CLUES TO GALAXY EVOLUTION FROM THE MAJOR MERGER RATE AT HIGH REDSHIFT

by

Russell E. Ryan Jr.

A Dissertation Presented in Partial Fulfillment
of the Requirements for the Degree
Doctor of Philosophy

ARIZONA STATE UNIVERSITY

August 2008

CLUES TO GALAXY EVOLUTION FROM THE MAJOR MERGER RATE AT HIGH REDSHIFT

by

Russell E. Ryan Jr.

has been approved

July 2008

Graduate Supervisory Committee:

Rogier A. Windhorst, Chair
James E. Rhoads
Paul A. Scowen
Evan Scannapieco
Andrei Belitsky

ACCEPTED BY THE GRADUATE COLLEGE

ABSTRACT

In this Dissertation, I present my work on a variety of topics on galaxy evolution from the deep fields observed by the Hubble Space Telescope. I derive spectrophotometric redshifts for the 1308 galaxies from the GRism ACS Program for Extragalactic Science in the Hubble Ultra Deep Field (HUDF). For the 81 galaxies with spectroscopic redshifts between 0.5 and 1.5, the standard deviation in the fractional error in $(1 + z)$ is 0.046. Using this redshift catalog, I conduct two extragalactic studies:

(1) The B-band galaxy luminosity function at redshift one. This spectrophotometric redshift catalog is 95% complete at 27.2 AB mag, which is nearly two magnitudes deeper than previous studies. Therefore, I am able to accurately determine that the faint-end slope of the galaxy luminosity function (LF) is –1.32. By comparing to numerous published measurements at various redshifts, I find evidence for a steepening of the faint-end slope with redshift.

(2) The galaxy major merger fraction and merger number density between redshifts 0.5 and 2.5. After correcting for mass incompleteness, I find that the major merger fraction of massive galaxies is not proportional to a power-law in $(1 + z)$ at high redshift, but rather appears to peak at an approximate redshift of 1.3. From this merger fraction, I infer that roughly 42% of massive galaxies have undergone a major merger since redshift one. To extend these measurements to higher redshifts, I determine the merger history of Lyman break galaxies selected as BVi'-band dropouts from the Great Observatories Origins Deep Survey and the HUDF. I correct these

high redshift merger statistics for contamination of low redshift early-type galaxies and low mass Galactic dwarfs. By adopting the published merger counts at low redshift, I find that the major merger number density for galaxies more luminous than –20.5 mag can be suitably fit by a two-component power-law, and peaks at an approximate redshift of 1.04. This evolution is qualitatively similar to that of X-ray selected AGN and provides circumstantial evidence that luminous AGN may be triggered by major mergers.

I would like to dedicate this dissertation to my loving and supportive wife, Amy.

ACKNOWLEDGMENTS

I must thank my research advisor, Dr. Rogier Windhorst, for his endless advice, financial support, wisdom, and encouragement over the years. He always put my needs, as well as the other graduate students', first. He has been an excellent mentor and an invaluable resource in preparing proposals, papers, and grants. I would also like to thank Dr. Seth Cohen, who has been a great source of daily help. I want to thank Dr. Rolf Jansen for his excellent advice on nearly every astrophysical topic. Finally, I would like to thank my committee for all their efforts to make this dissertation possible: Prof. James Rhoads, Dr. Paul Scowen, Prof. Evan Scannapieco, and Prof. Andrei Belitsky.

As a graduate student, I was a part of many exciting collobrations with individuals across the country and beyond. These people have provided me many inciteful comments and suggestions, invigorating conversations, and new ideas. Their contributions as coauthors have greatly improved significant portions of my disertation, and for that, I am very grateful. I would like to alphabetically acknowledge these individuals: Drs. Tamas Budavári, Seth Cohen, Norman Grogin, Nimish Hathi, Chuck Keeton, Sadegh Khochfar, Sangeeta Malhotra, Leonidas Moustakas, Nino Panagia, Nor Pirzkal, James Rhoads, Sperello di Serego Alighieri, Joe Silk, Amber Straughn, Todd Veach, Chun Xu, and Haojing Yan. I would also like to acknowledge several professors who have had a major impact on my education, Drs. Brian McNamara, John Page, Dave Burstein, John Venables, and Joe Shields. I would like to thank my fellow graduate students and friends for the "good times" throughout the years:

Jason Cook, Seth Cohen, Steven Finkelstein, Brian Frank, Nimish Hathi, Allison Loll, Jacob Russell, Keely Snider, Amber Straughn, Kaz Tamura, and Todd Veach.

I have been very fortunate over the years to have been supported by a series of generous funding institutions. I am particularly grateful for the several years of support as a teaching assistant from the Physics Department. I was provided a NASA Space Grant Fellowship for a few semesters, which greatly accelerated my research. The Graduate and Professional Student Association supported my trip to the meeting of the AAS in Honolulu, HI. I have been awarded two Archival grants (AR 10974 and AR 11772) and benefited from several others (AR 11287, GO 15030.07A, GO 09793), through the Space Telescope Science Institute, which is operated by AURA under NASA contract NAS 5-26555.

I am very grateful for the love and support from my parents and family, who have always stood by me.

Finally, I could have never completed this degree or dissertation without the endless love and support of my wife, Amy.

TABLE OF CONTENTS

LIST OF TABLES

LIST OF FIGURES

Figure Page

CHAPTER 1

Introduction

1.1. Review

The deep fields observed with the Hubble Space Telescope (HST) have revolutionized our understanding of galaxy formation and evolution by probing flux ranges and angular scales not achievable by even the best ground-based observatories. Owing to these unique properties, the amount of ancillary data — whether imaging at various wavelengths or spectroscopy from the largest ground-based telescopes — is continuously growing, making these deep fields among the richest datasets to date. Consequently these very powerful fields have attracted countless authors, who have studied nearly every observable property of these faint galaxies.

The original Hubble Deep Field (HDF; PID 6337; Williams et al. 1996) was the first survey undertaken with HST to push the photometric limits to AB ~ 28 mag. This significantly increased depth led to a number of unexpected results, many of which have become cornerstones in our current understanding of galaxy evolution. Since it is impractical to review the entire suite of work that has surfaced from the HDF observations, I will only briefly highlight those which are most relevant to this dissertation:

In the local Universe, the majority of massive galaxies can easily be classified into the broad categories established by Hubble (1936). However with the HDF observations, this morphological dichotomy came under significant examination. While early work with HST extended morphological classifications down to $V \sim 20$ mag (eg. Driver et al. 1995b; Glazebrook et al. 1995), the HDF observations routinely permitted visual classifications to $I \sim 24$ mag. This added depth over the general HST images

fueled the desire for quantitative morphological classification schemes, most notably the concentration and asymmetry parameters (eg. Abraham et al. 1996; van den Bergh et al. 1996), artificial neural networks (Odewahn et al. 1996), and bulge-disk decompositions (Marleau & Simard 1998), and Sérsic indices (Sérsic 1968). While these quantitative approaches have many key virtues — the measurements can be automated, free of qualitative biases, and are generally repeatable — they are not without limitations. For example, there are general concerns regarding the sensitivity of these morphological estimators to the signal-to-noise per pixel, the angular size of the galaxies, resolution of the images, and various redshift-dependent effects (such as bandpass-shifting and cosmological surface brightness diming; Ferguson, Dickinson, & Williams 2000). Whether determined from these quantified metrics or through visual classifications, it has become clear from the HDF observations that the distribution of morphological types at faint magnitudes and moderately higher redshifts ($z \lesssim 1$) changes dramatically from what is observed in the local Universe. For galaxies with $21 \lesssim I \lesssim 25$ mag, Abraham et al. (1996) show that $\sim 40\%$ of all galaxies are irregular/merging/peculiar systems. While bandpass-shifting may account for some of this "morphological evolution," the majority of galaxies do not exhibit strong morphological changes from the restframe ultraviolet to optical (eg. Teplitz et al. 1998; Windhorst et al. 2002), the so-called "morphological K-correction."

In addition to their marked structural changes, high redshift galaxies are generally smaller than their local counterparts. To further investigate this trend, Roche et al. (1998) propose a simple size-luminosity evolution model (SLE), wherein star-

formation in disk galaxies proceeds outward from the nucleus. However many of these measurements will breakdown at faint magnitudes ($I \gtrsim 25$ mag), since most galaxies will only extend over a few independent resolution elements (Ferguson, Dickinson, & Williams 2000). Naturally this worsens the already existing issues with the aforementioned measures of galaxy morphology.

Since the HDF observations facilitated the study of galaxies to limits far fainter than can be spectroscopically pursued by ground-based facilities, a need for a new tool to determine distances to faint galaxies arose. While notion of photometric redshifts existed long before the HDF (eg. Baum 1962; Koo 1985), they became a standard and widely embraced technique with the success of the HDF. Steidel et al. (1996) pioneered the use of color selections to identify high redshift galaxies based on a spectral break from the Lyman limit or Lyman-α forest. Since this "dropout" technique can only provide a coarse redshift estimate for galaxies at a specific redshift interval, it is necessary to use the additional broadband photometry to increase both the reliability and the range of the derived photometric redshifts. Therefore many authors have fit spectral templates (eg. Coleman, Wu, & Weedman 1980; Bruzual & Charlot 1993) to the bevy of photometric data to infer galaxy redshifts (eg. Gwyn & Hartwick 1996; Mobasher et al. 1996; Lanzetta, Yahil, & Fernández-Soto 1996; Sawicki, Lin, & Yee 1997). Such photometric redshifts are particularly accurate when the optical photometry is supplemented with comparably deep infrared data (eg. Fernández-Soto, Lanzetta, & Yahil 1999; Yahata et al. 2000). The precision of photometric redshifts are generally quoted as a fractional error in $(1 + z)$ with respect to the traditionally

measured spectroscopic redshifts, $\Delta z/(1+z_{\rm spec})$. From deep spectroscopy with the Keck Observatory, Cohen et al. (2000) estimate that a photometric redshift survey can achieve $\sigma[\Delta z/(1+z_{\rm spec})] \simeq 0.05$ for $\gtrsim 90\%$ of the galaxies at $z < 1.3$. Based on the success of these studies, the photometric redshifts derived from the HDF have become the benchmark against which all photometric redshift surveys are compared (Ferguson, Dickinson, & Williams 2000).

The cosmic star-formation rate density (SFRD), as often traced by the integrated ultraviolet (UV) luminosity (eg. Kennicutt 1998), has been the focus of many studies in the HDF. Early work by Lilly et al. (1996) established a sharp increase in the SFRD with redshift for $z \lesssim 1$. To extend this work, Madau et al. (1996) applied the dropout criteria to select high redshift galaxies, and found that the cosmic SFRD declines by nearly a factor of 10 over $1 \lesssim z \lesssim 4$. These early estimates only represent lower limits, since all corrections will tend to increase these values (Ferguson, Dickinson, & Williams 2000). The source and magnitude of these corrections has been the subject of further investigation, and they can be broadly characterized as either refinements in the galaxy selection and redshift estimation or the dust attenuation correction. Regarding the galaxy selection, increasing the area in the color–color space tends to increase the number of Lyman break candidates and the contamination of low redshift interlopers, such as elliptical galaxies at $z \sim 1$ or low-mass Galactic dwarfs. Since this exacerbates the need for subsequent spectroscopic observations, it can be more practical to model the stellar populations with spectral templates (eg. Sawicki & Yee 1998; Fontana et al. 1999) in a fashion which is similar to the

photometric redshift technique. In general the luminosity densities derived by this technique are higher than what is found from the dropout selections, rendering the apparent decline in the SFRD at $z \gtrsim 1$ up for debate. While the stellar population modeling naturally accounts for any internal reddening, many authors have developed extinction corrections based on local starbursts. For example, Meurer et al. (1997) calibrated the UV slope with the far-infrared flux (60 μm $\lesssim \lambda_{\rm obs} \lesssim$ 100 μm) to derive a bolometric extinction correction. With these corrections, their SFRDs are roughly consistent with those derived from the stellar population modeling, and imply that there may be little decline in the SFRD at $z \gtrsim 1$ (Meurer, Heckman, & Calzetti 1999).

As the measurements of the cosmic SFRD have improved, its role in galaxy evolution has also been developed. Madau, Pozzetti, & Dickinson (1998) show that the observed SFRD at $z \lesssim 4$ is consistent with the colors and mass densities of local galaxies, the metallicites of damped Lyα absorbers, and the integrated far-infrared background. Since high redshift galaxies generally have high star-formation rates and small physical sizes (as discussed above), their surface brightnesses can be significantly higher than those of local galaxies. Indeed, this effect was unknown to Bahcall, Guhathakurta, & Schneider (1990) and was likely the source of their pessimistic prediction.

Despite the overwhelming success of the HDF, many of these discussed conclusions are subject to further scrutiny, owing to the appreciable cosmic variance introduced by its narrow field-of-view (~ 5.7 arcmin^2). Therefore additional deep surveys with HST must be conducted. The Great Observatories Origins Deep Survey

(GOODS; PID 9583; Giavalisco et al. 2004a) consists of a northern and souther field, each covering ~ 160 arcmin^2. This roughly 50-fold increase in surveyed area, at a comparable flux limit, led to the study of several additional topics.

Like the HDF, the GOODS fields have benefited from a wealth of supporting observations, and the deep HST imaging has developed a symbiotic relationship with the near- to mid-infrared data (3.6 μm $\leq \lambda_{\rm obs} \leq$ 24 μm) from the Spitzer Space Telescope (SST). For galaxies at $0.6 \lesssim z \lesssim 2.6$, the Infrared Array Camera (IRAC) samples the restframe K-band, which can be a reliable measure of the stellar mass (Brinchmann & Ellis 2000; Cole et al. 2001). However to take full advantage of the suite of imaging, many authors fit stellar population synthesis models to the multiwavelength data from HST and SST to select galaxies based on their stellar mass. These stellar mass studies have established the evidence for a population of passively-evolving, massive ($M_* \gtrsim 10^{11}$ M$_\odot$) galaxies at $1.6 \lesssim z \lesssim 2.5$ (eg. Cimatti et al. 2004; Daddi et al. 2004; Papovich et al. 2006). While there have been suggestions of equally massive systems at $z \gtrsim 5$ (eg. Eyles et al. 2005; Mobasher et al. 2005; Stark et al. 2007; Wiklind et al. 2008), most mass estimates for the highest redshift galaxies ($z \simeq 6$) are considerably lower ($M_* \sim 10^{9-10}$ M$_\odot$; Yan et al. 2006; Lai et al. 2007). These stellar mass studies have supported the already growing idea of the downsizing in massive galaxies (eg. Cowie et al. 1996; Bundy, Ellis, & Conselice 2005; Treu et al. 2005). In the downsizing model, star-formation in massive galaxies was completed very early in the history of the Universe (Cowie et al. 1996), which may manifest

itself as a stellar population that appears to have passively evolved over the majority of the Hubble time.

The area affords the GOODS survey a unique opportunity to study intrinsically rare objects, which may elude narrower surveys. It is widely accepted that the deposition of gas onto to a central, supermassive black hole (SMBH) results in an active galactic nuclei (AGN). Even from the earliest observations of AGN and quasi-stellar objects (quasars or QSOs), it was clear that such objects are rather rare. Furthermore this phenomena is capable of emitting over many orders in frequency, which inherently requires multiwavelength observations to record a complete census of objects for study. By combining the X-ray luminosity function and an appropriate set of AGN SEDs, Treister et al. (2004) apply a simple unified AGN model, where there are roughly three times as many obscured AGN to unobscured, to reproduce the z'-band flux and photometric redshift distributions of hard X-ray selected AGN. Based on the deep X-ray observations from the Chandra X-ray Observatory (CXO; which preceded the HST and SST imaging) in GOODS-N, Barger & Cowie (2005) find a deficit in the space density of high-luminosity AGN at $z \gtrsim 1$. They argue for a pure-luminosity evolution model (PLE; Barger et al. 2005), which is in contrast to the more common luminosity-dependent density evolution (LDDE; eg. Ueda et al. 2003; Hasinger, Miyaji, & Schmidt 2005). Cristiani et al. (2004) find a similar dearth of high redshift ($3.5 \lesssim z \lesssim 5.2$) moderate luminosity QSOs, when compared to PLE of the $z \simeq 2.7$ luminosity function and a constant universal efficiency of the formation of SMBHs. In any case, it is clear that the space density of X-ray selected AGN

increases to $z \sim 1$ and likely declines for $z \gtrsim 1$, which is broadly consistent with the density evolution of radio selected AGN (eg. Waddington et al. 2001).

To fully exploit the multiwavelength survey, many authors select objects at one frequency and study their properties at another. For the GOODS fields, this generally means examining the optical images of X-ray or radio selected AGN (Rosati et al. 2002; Afonso et al. 2006). Many of the optical counterparts to X-ray AGN are bulge-dominated, and do not show an increased number of close companions or enhanced image asymmetry (eg. Grogin et al. 2003), which argues for AGN not generated by a major merger (Grogin et al. 2005), or the visual clues of the major merger are no longer present. By identifying the HST counterparts to the CXO sources, Koekemoer et al. (2004) discovered a new population of AGN with extreme X-ray-to-optical flux ratios (EXOs). The broadband photometry from the majority of EXOs are best-fit by early-type galaxy templates with a median photometric redshift of $z \simeq 1.9$, while a few examples may be at $z \gtrsim 6$ (Mainieri et al. 2005). Since the AGN energy source is the sporadic feeding of the central SMBH, its flux is not constant with time, but rather varies chaotically. Klesman & Sarajedini (2007) find that 51% and 26% of AGN selected from their soft X-ray or mid-infrared fluxes are optically variable, respectively. Furthermore, Cohen et al. (2006) find that $\sim 1\%$ of all galaxies in the Hubble Ultra Deep Field have variable nuclei.

By utilizing its superior angular resolution, the study of galaxy sizes and morphologies has been consistently studied since the commissioning of HST. One of the many unexpected results evident from the HDF was that galaxies become smaller at

high redshift. This observation has been supported with the wider GOODS fields, where sizes have been observed to scale as $H(z)^{-1}$ or $(1+z)^{-1.1}$ (Ferguson et al. 2004; Dahlen et al. 2007), and $H(z)$ is the Hubble parameter. Furthermore, high redshift Lyα emitting galaxies (LAEs) are significantly more compact than the typical LBG at the same redshift (eg. Dow-Hygelund et al. 2007), which may reflect the generally lower masses of the LAEs (eg. Pirzkal et al. 2007).

The increased fraction of galaxies with significantly disturbed morphologies at high redshift suggests that galaxy merging may play an increasingly important role in galaxy evolution. Many galaxies at high redshifts ($0.5 \lesssim z \lesssim 3$) show qualitative signatures of a recent major merger, such as tidal tails or multiple cores (de Mello et al. 2006; Elmegreen & Elmegreen 2006; Ravindranath et al. 2006; Elmegreen et al. 2007). This is somewhat reinforced by various quantitative morphological or structural indices (Conselice 2003a; Lotz et al. 2006). While the irregular appearance of these high redshift galaxies suggest that they were assembled by major mergers, the seemingly "normal" morphology the bulge-dominated systems hints at a *monolithic* formation (eg. Eggen, Lynden-Bell, & Sandage 1962; Larson & Tinsley 1978). However, the increase in bulge-dominated systems which tend to become bluer with redshift indicates that some early-type galaxies may have also formed from multiple mergers at $z \gtrsim 1$ (Dahlen et al. 2007). Futhermore N-body and smoothed particle hydrodynamic simulations suggest that elliptical galaxies can be formed by a major merger when the gas fraction of progenitors is relatively low (eg. Toomre & Toomre 1972; Barnes 1992;

Springel, Di Matteo, & Hernquist 2005b). The evolution and assembly of massive early-type galaxies remains a contentious point which is still actively debated.

Focusing on the most recent *pencil-beam* survey, the Hubble Ultra Deep Field (HUDF; PID: 10086; Beckwith et al. 2006) is the deepest optical image ever taken of the Universe. With 400 orbits in a single Advanced Camera for Surveys (ACS) pointing, the HUDF reaches an unprecedented AB ~ 30 mag in the $BVi'z'$-bands, which is nearly two magnitudes deeper than the previous HST deep fields. Since the HUDF is still a relatively new dataset, it has not been studied in the same detail as the HDF or GOODS.

Its unrivaled depth has made the HUDF the ideal dataset for studying the most distant objects detectable in the Universe. Using the deep Near Infrared Camera and Multi-Object Spectrometer (NICMOS) imaging in the HUDF, many authors have claimed either successful detections or upper limits on the number of z'-band dropouts at $7 \lesssim z \lesssim 8$ (Bouwens et al. 2004b; Yan & Windhorst 2004b; Bouwens et al. 2006) and J-band dropouts at $z \sim 10$ (Bouwens et al. 2005). However, most of the work on such galaxies has focused on the i'-band dropouts at $z \simeq 6$, particularly measuring and interpreting their luminosity function (Stanway et al. 2004a; Yan & Windhorst 2004b; Bouwens et al. 2006, 2007). While no two authors find identical sets of dropout objects and generally reach at slightly different conclusions, several things are clear. The galaxy luminosity function evolves considerably over $1 \lesssim z \lesssim 6$, although whether this evolution is in the overall density (Φ^*), its characteristic luminosity (L^*), or its faint-end slope (α) is somewhat disputed (eg. Bouwens et al. 2004a;

Bunker et al. 2004; Stanway et al. 2004a; Yan & Windhorst 2004b; Bouwens et al. 2007). The stellar population synthesis fits to the available broadband photometry at 1200 Å $\lesssim \lambda_{\rm rest} \lesssim$ 2400 Å, suggest that the i'-band dropouts are very young, have low metallicities, and are actively forming stars (eg. Stanway et al. 2004a; Thompson et al. 2006; Bouwens et al. 2007). Furthermore, there are tentative claims that these galaxies may form stars from a top-heavy IMF with an appreciable internal reddening (eg. Stiavelli, Fall, & Panagia 2004; Stanway, McMahon, & Bunker 2005). Since many of the brighter $z \simeq 6$ candidates have been spectroscopically confirmed with large ground-based facilities (such as the Keck Observatory or the Very Large Telescope; Le Fèvre et al. 2005; Grazian et al. 2006) or HST (eg. Malhotra et al. 2005), it is possible to subselect galaxies for Lyα emission. These LAEs generally have high equivalent widths (EW $\sim$ 200 Å) and star-formation rates (eg. Rhoads et al. 2005; Stanway et al. 2007), despite being considerably less massive than their LBG counterparts (Lai et al. 2007).

The typical LBG at $z \gtrsim 3$ is very compact and nearly unresolved (eg. Hathi et al. 2008a; Hathi, Malhotra, & Rhoads 2008b), however there are several galaxies for which some morphological information is available. Rhoads et al. (2005) suggest that the linear morphology of a particular LAE at $z \approx 5.4$ is caused by a recent merger, and that its extended Lyα emission may be from an active nucleus. They speculate that this galaxy is in the assembly process, and is actively accreting gas onto its SMBH. The multiple knots of the Rhoads et al. (2005) object are a true hallmark of a recent merger, however this object is not unique. Many LBGs have a number of

close companions (eg. Yan & Windhorst 2004b; Coe et al. 2006) and may reside in overdense regions (eg. Stanway et al. 2004b; Malhotra et al. 2005; Wang, Malhotra, & Rhoads 2005). Hathi et al. (2008a) investigate the surface brightness profiles of the composite image of a number of compact LBGs selected as BVi'-band dropouts. They find that the composite galaxy is sufficiently resolved and shows a break in its surface brightness profile, which they interpret as indicative of its average dynamical age. While these results provide some qualitative evidence of the galaxy merger rate at $z \simeq 6$, a thorough and quantitative analysis is needed before any firm conclusions can be drawn.

I have reviewed three very successful imaging campaigns conducted with HST, however this by no means constitutes a complete set. While other deep surveys represent an equal or larger investment of HST time, such as the GEMS survey (Rix et al. 2004), the AEGIS survey (Davis et al. 2007), or the COSMOS survey (Scoville et al. 2007), and have also been extremely successful, only the HDF, GOODS, and HUDF combine the necessary depth and many photometric bandpasses to explore many of these topics presented here. Therefore these deep fields — the HUDF and GOODS — are the central datasets for this Dissertation. I show the rough positions of these HST deep fields and the planned observations with the Wide Field Camera 3 (WFC3), to be launched in October 2008, in Figure 1.

1.2. Outline

This Dissertation focuses on galaxy evolution as observed in the HUDF and GOODS fields and is organized as follows. In Chapter 2, I outline my work with the

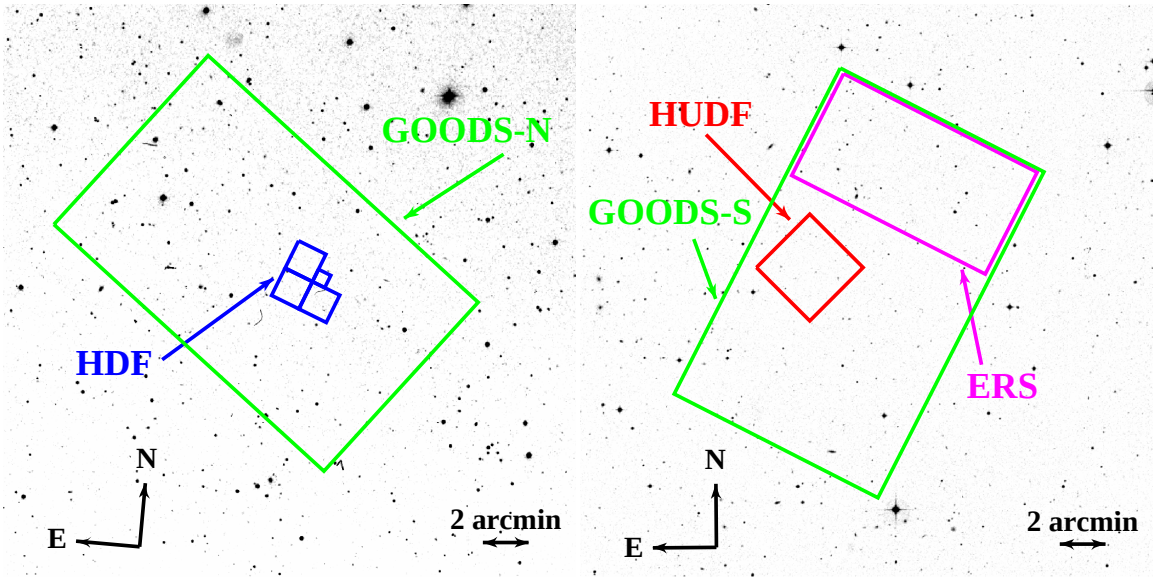

FIG. 1. These greyscale images are taken from the Digital Sky Survey (DSS) in the B-band. The green apertures show the rough positions of the GOODS-North (left panel; $12^h36^m55^s$, $+62°14^m15^s$) and the GOODS-South (right panel; $3^h32^m30^s$, $-27°48^m20^s$) fields (Giavalisco et al. 2004a). The blue and red apertures represent the positions of the HDF (Williams et al. 1996) and HUDF fields (Beckwith et al. 2006), respectively. In the GOODS-S, I have indicated the approximate position of the Early Release Science (ERS) data to be taken with the Wide Field Camera 3 (WFC3). This survey will add F225W, F275W, and F336W in the ultraviolet, F098M, F125W, and F160W in the infrared to $\sim$30% of GOODS-S, and G102L and G141L infrared grisms in a limited portion of the ERS field. Assuming a successful servicing mission to HST (the launch is currently planned for October 2008), this strip of $\sim$50 arcmin^2 in GOODS-S will have 10-band photometry to AB$\sim$27 mag and low-resolution grism observations from 6000 Å to 1.7 μm to AB$\sim$26 mag over a single WFC3 field, making this a very unique and powerful dataset (see § 7.3).

slitless spectroscopic survey undertaken with HST (GRAPES; PID: 9793; PI: S. Malhotra Pirzkal et al. 2004). In particular, I describe the construction and calibration of the spectro-photometric redshift catalog. In Chapter 3, I use this redshift catalog to compute the galaxy luminosity function in the restframe B-band for galaxies at $z = 1.0 \pm 0.2$. I discuss these results in the context of the redshift-dependence of the faint-end slope and its relevance to galaxy evolution. In Chapter 4, I study the redshift evolution of the galaxy pair fraction at $0.5 \leq z \leq 2.5$ for massive galaxies drawn from the GRAPES redshift catalog. In Chapter 5, I extend these pair fraction measurements to $3.8 \lesssim z \lesssim 6$ from Lyman break galaxies, which are selected as BVi'-band dropouts. With these two Chapters (4 and 5), I have determined the major merger history of massive galaxies for the last ~ 12.7 Gyr of the history of the Universe. In Chapter 6, I present my estimate of the scale height of the L- & T-dwarf population in the Milky Way. From these Galactic structure models, I determine the fraction of i'-band dropouts that could have been mistakingly identified as low-mass, Galactic dwarfs. In Chapter 7, I summarize many of these conclusions and discuss possible future to extend much of this work.

Much of the work presented in this Dissertation has been published in the Astrophysical Journal: Chapters 2 and 3 have appeared as Ryan, R. E., Jr., et al. 2007, ApJ, 668, 839 (© and published by the American Astronomical Society in the October 2007 issue of the Astrophysical Journal). Chapter 4 has appeared as Ryan, R. E., Jr., et al. 2008, ApJ, 678, 751 (© and published by the American Astronomical Society in the May 2008 issue of the Astrophysical Journal). Chapter 6

has appeared as Ryan, R. E., Jr., et al. 2005, ApJ, 631, L159 (© and published by the American Astronomical Society in the October 2005 issue of the Astrophysical Journal). Figure 8 is taken from Khochfar, S., Silk, J., Windhorst, R. A., & Ryan, R. E., Jr. 2007, ApJ, 668, L115 (© and published by the American Astronomical Society in the October 2007 issue of the Astrophysical Journal), and appears here courtesy of S. Khochfar.

CHAPTER 2

The GRAPES Redshift Survey

2.1. Introduction

Measuring a large sample of accurate redshifts for distant galaxies is one of the most daunting tasks in observational cosmology and extragalactic science. Given the typical brightness (AB$\sim$26 mag) of distant ($z \gtrsim 1$) galaxies, optical spectroscopy requires extensive observations on the largest telescopes. While multi-slit spectrographs and grating prism (grism) modes allow for many simultaneous spectroscopic observations, they can be severely limited in wavelength coverage or spectral resolution. Therefore, the use of photometric redshifts estimated from observed fluxes is a necessity for the statistical study of distant galaxies (for example Grazian et al. 2006; Coe et al. 2006; Mobasher et al. 2007).

Since the release of the original Hubble Deep Field (HDF; Williams et al. 1996), photometric redshifts have been the focus of numerous extragalactic studies and are at the core of many others. At present, there are primarily two different, yet very similar, techniques for computing these redshifts: χ^2 minimization and Bayesian statistics. The minimization scheme compares a set of model fluxes measured from empirical or synthetic spectral energy distributions (SEDs) to the observed fluxes. Early studies using χ^2 minimization were met with some skepticism regarding possible degeneracies between redshift and internal reddening in galaxy colors (Lanzetta, Yahil, & Fernández-Soto 1996). With the addition of near-infrared (JHK) imaging in the HDF, Fernández-Soto, Lanzetta, & Yahil (1999) showed that many of the degeneracies can be broken to yield fairly accurate redshifts ($\sigma[\Delta z/(1+z_{\rm spec})] \approx 0.1$). In contrast, the Bayesian marginalization uses prior redshift probabilities, obtained by

other means, to compute more accurate photometric redshifts (Benítez 2000). While the current implementation of this technique (`BPZ`) produces more reliable redshifts from limited observational constraints, it does not compute many useful quantities (eg. k-corrected magnitudes, probability densities, V-band extinction, and age; Caputi et al. 2004).

2.2. Observations

The GRism ACS Program for Extragalactic Science (GRAPES; Pirzkal et al. 2004) data consists of 40 orbits with the Hubble Space Telescope (HST) of the Hubble Ultra Deep Field (HUDF; Beckwith et al. 2006) taken during HST-Cycle 12. These slitless spectroscopic observations were conducted with the ACS in the G800L mode, range from ∼5500–10500 Å with a spectral resolution of $R \simeq 100$, and cover $\simeq 11$ arcmin^2. The GRAPES data were taken over four epochs, each with a different position angle in order to minimize the contamination from nearby objects. These data were supplemented with the existing ACS grism observations of Riess et al. (2004), giving a total dataset of five position angles and an integration time of 1.1×10^5 s. A thorough discussion of the GRAPES observations, its data reduction, and the spectral extraction and calibration methods can be found in Pirzkal et al. (2004).

2.2.1. *Additional Bandpasses*

Given the limited spectral range of the GRAPES observations, it is necessary to include the broadband data available in this well-observed field to increase accuracy of the spectro-photometric redshift measurements. To extend our spectra to

~ 3000 Å and 2.3 μm, we include the CTIO-MOSAIC II U-band observations, the HST-NICMOS J- and H-band (Thompson et al. 2005), and the VLT-ISAAC K_s-band data. Therefore, the final dataset has $\sim$40 independent spectral points from the combination of broadband and grism observations.

Since the HUDF i'-band image is the deepest optical exposure ever taken, it is used to define the apertures for the near-ultraviolet (NUV) and near-infrared (NIR) data. To eliminate aperture corrections between the broadband data, we convolve all images to the same full-width at half-maximum as the worst observation (the U-band data), which is $1\farcs3$. While convolving the HST images is highly undesirable, the NUV constraint is essential to accurately determine the redshifts at $1 \lesssim z \lesssim 2.3$ (Ferguson 1999). Stanway, Bunker, & McMahon (2003) suggest that surveys with U- and B-band data will be particularly powerful in distinguishing between the 4000 Å and Lyman breaks, thereby drastically reducing the catastrophic failure rate for the photometric redshifts. Since quasars have roughly featureless continua, at least from the perspective of broadband observations, their photometric redshifts remain somewhat degenerate in the absence of a strong Lyman break. Since the PSF is ~ 20 times larger for the ground-based observations, many objects in the HST images become confused after the image convolution. Objects were deemed confused if after the convolution more than one object from the original GRAPES catalog (Pirzkal et al. 2004) was within the new aperture. Therefore, the U-band flux was only measured for galaxies that have unconfused detections. The remaining

galaxies were only measured from the unconvolved images, and do not have a U-band measurement.

The final photometric dataset includes 1308 galaxies with grism spectroscopy. Since the HST-NICMOS data covers $\sim$50% of the HUDF observed with ACS, 687/1308 galaxies have J- and H-band imaging and only 543/1308 galaxies have *viable* U-band data. In total, 273/1308 galaxies have the entire suite of UB+grism+JHK_s data. In general, these are the brighter galaxies, for which the convolution is less significant. All broadband magnitudes are measured as `MAG_AUTO` by `SExtractor` in dual-image mode with the default values for `PHOT_AUTOPARAMS`. To determine the apertures, we use `DETECT_THRESH` and `ANALYSIS_THRESH` of 1.5 (see Bertin & Arnouts 1996, for a discussion of these parameters).

2.2.2. *Source Catalogs*

For the matched aperture photometry, we use the convolved HST-ACS i'-band as the *detection image* in `SExtractor`. Since the GRAPES spectra were extracted from a spectral trace of fixed width (Pirzkal et al. 2004), they must be scaled to reproduce the fluxes measured by `SExtractor` in the HUDF. Therefore, we define a multiplicative aperture correction as

$$-2.5 \log \beta = (i'_{\rm HUDF} - i'_{\rm GRAPES}) \,, \tag{2.1}$$

where $i'_{\rm HUDF}$ and $i'_{\rm GRAPES}$ are the i'-band magnitudes measured from the ACS imaging and the GRAPES spectra, respectively. Since the i'-band image was used to define the apertures used in the other images, there is no need for additional corrections between the broadband images.

The distribution of these aperture corrections is shown in Figure 2. The width of this distribution is related to the properties of the spectral extraction, contamination of nearby objects, and the broadband apertures. Since the GRAPES spectra are most reliable from $\sim 6000 - 9500$ Å, they do not fully cover the V- or z'-bands, therefore scaling to multiple bands or using a wavelength-dependent aperture correction is not possible with these data. Lastly, the scaled GRAPES spectra are rebinned onto a common wavelength grid, and are assigned a 100 Å wide, top-hat filter transmission curve. This procedure typically decreases the number of GRAPES spectral points by a factor $\sim$2 and boosts their signal-to-noise ratio, which markedly helps for the faintest objects ($z' \sim 27$ mag).

2.3. Spectro-Photometric Redshifts

Measuring redshifts from a calibrated spectrum requires readily identifiable absorption or emission lines or characteristic breaks. Since the GRAPES data have a resolution of $R \simeq 100$, any narrow spectral features are typically not detectable. Xu et al. (2007) measured emission line redshifts from $\sim$100 GRAPES galaxies. Therefore, we complement that study by estimating spectro-photometric redshifts for the remaining dataset from the low-resolution GRAPES spectra.

From the scaled spectra and broadband fluxes, we compute spectro-photometric redshifts with the code `HyperZ` of Bolzonella, Miralles, & Pelló (2000). The alternative code `BPZ` of Benítez (2000), was not used for three reasons: (1) It currently does not constrain the galaxy ages to be less than the age of the Universe; (2) It does not compute many useful secondary quantities; and (3) With our spectral constraints

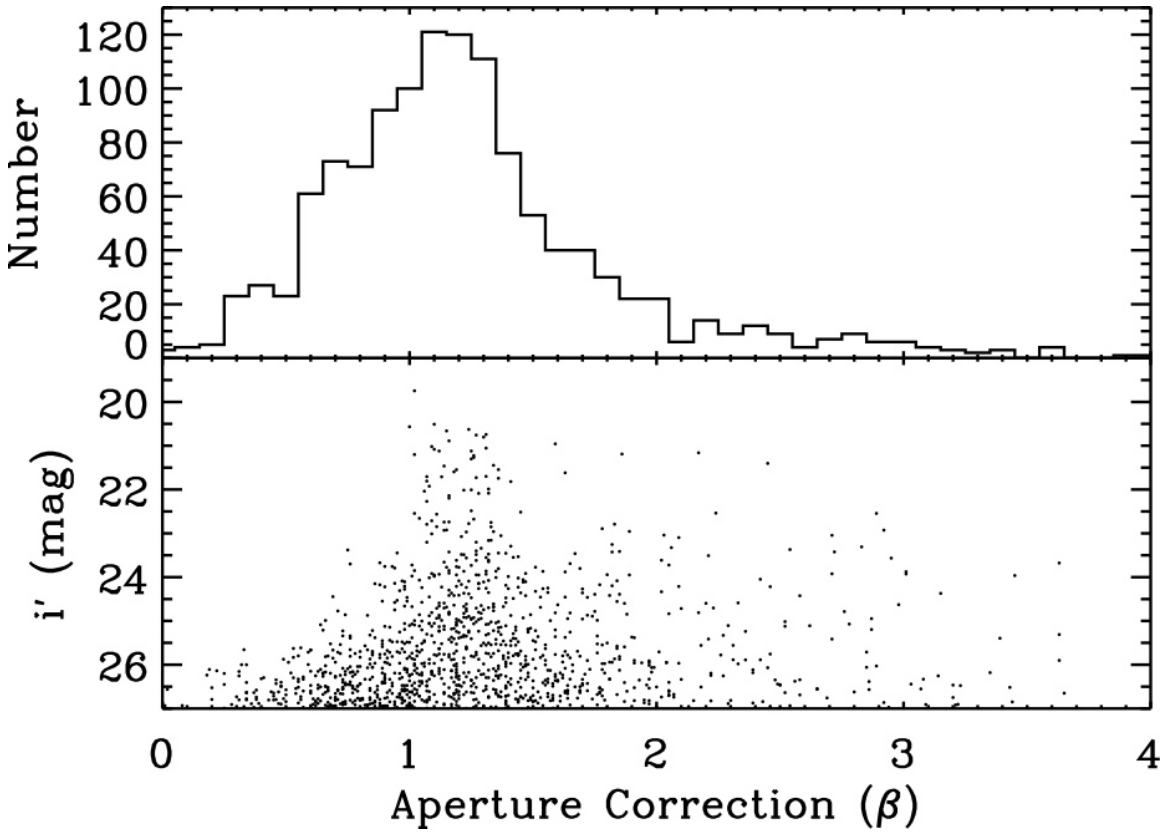

FIG. 2. The aperture correction is defined such that the GRAPES spectra reproduce the i'-band fluxes measured from the HUDF. Since the NUV and NIR fluxes are measured with apertures defined by the i'-band data, there are no additional corrections to the broadband data. *Upper panel*— The distribution of aperture corrections. The GRAPES spectra are only scaled to reproduce the i'-band fluxes, since their usable portion does not completely cover the neighboring bandpasses (V and/or z'). *Lower panel*— The dependence of the i'-band magnitude on the aperture correction. The majority of the objects with $\beta \leq 1$ are near the detection limit of $z' \simeq 27.2$ mag, suggesting that uncertainties in the background subtraction may be the cause of these aperture corrections (Pirzkal et al. 2004). This figure is reproduced from Ryan et al. (2007).

and coverage, `BPZ` is not expected to substantially outperform `HyperZ`. Mobasher et al. (2004) compares the quality of redshifts from `HyperZ` and `BPZ` for a sample of $\simeq$400 galaxies in the Chandra Deep Field-South using broadband fluxes. They show that the rms scatter in the photometric redshifts is 0.140 and 0.072 for strict maximum likelihood and Bayesian techniques, respectively. In Figure 3, we show three observed SEDs with best-fit templates, for which there is reasonable agreement between our redshift and the published value. These examples illustrate the power of the GRAPES spectra to locate the 4000 Å break (the top two) and the Lyα-break (the lower one) at various redshifts.

Using the set of SED templates summarized in Table 1, `HyperZ` minimizes the reduced χ^2 between the observed and modeled fluxes as a function of redshift, age, and extinction. By omitting the $Vi'z'$-bands in the spectro-photometric redshift calculation, the combination of scaled GRAPES spectra and remaining broadband fluxes typically yields ~ 40 fully independent spectral bins per galaxy. In Figure 4, we show the distribution of best-fit spectral types for the 1308 galaxies. Since the Bruzual & Charlot (BC03; 2003) templates are generated at a series of finite time steps of $\Delta \log t \lesssim 0.05$, we require each galaxy be younger than the age of the Universe at its redshift. The *Burst* template is a single, instantaneous burst followed by passive stellar evolution. Since this template is the most common, we show the distribution of its stellar ages in the inset. We see that majority of the *Burst* models are very young, which is not surprising, since most galaxies are expected to be blue and actively forming stars at $z \sim 1$ (eg. Xu et al. 2007).

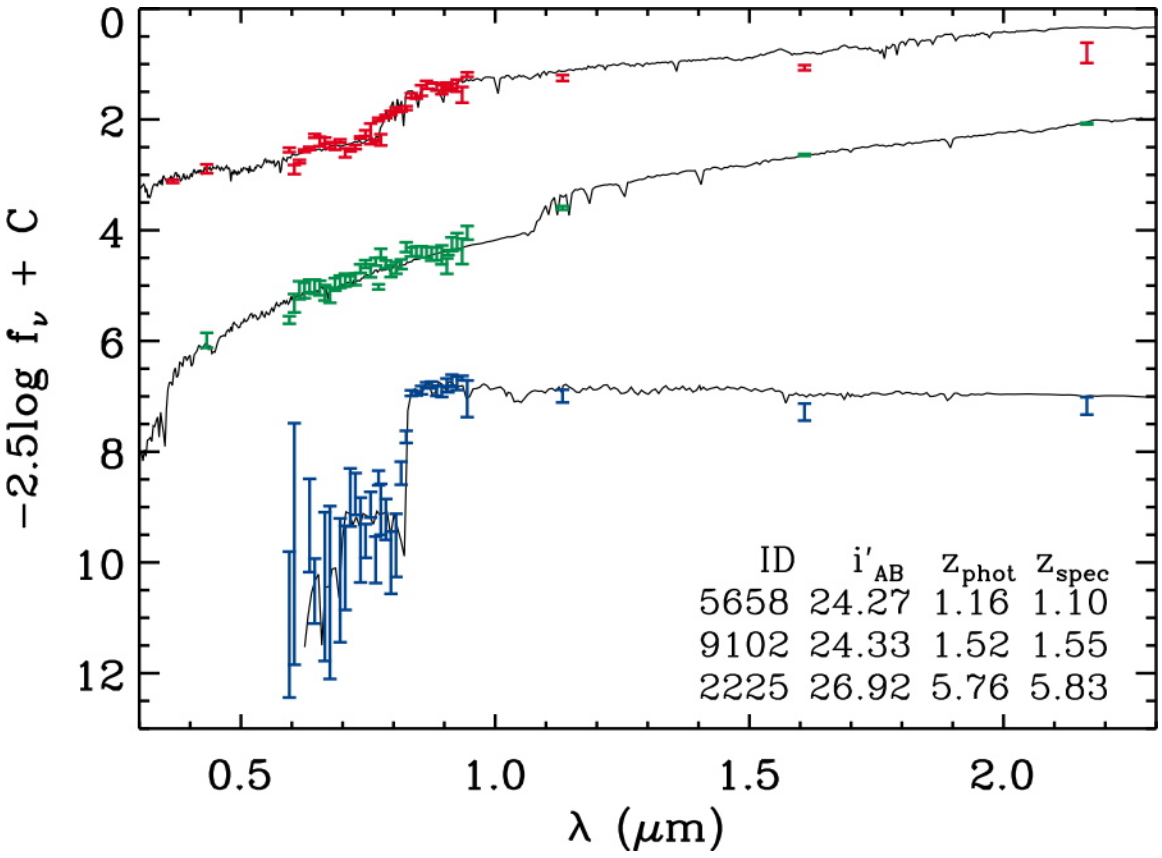

FIG. 3. These examples highlight two advantages of the GRAPES data: high signal-to-noise at faint flux levels ($i' \sim 25$ mag) and excellence in determining spectral breaks. In the lower-right, we tabulate the HUDF ID, i'-band magnitude, the spectro-photometric redshift derived in this work, and the published spectroscopic redshift. The spectra are arranged in decreasing redshift, so that from top to bottom the HUDF IDs are 5658, 9102, and 2225. With the addition of the Wide-Field Camera 3 (WFC3) on HST, we can expect IR grism data at $1.1 - 1.7$ μm. The combination of ACS and WFC3 spectra will provide an extremely broad spectral coverage at low-medium resolution. This figure is reproduced from Ryan et al. (2007).

TABLE 1
HyperZ Templates

Template†	SpT†	τ‡ (Gyr)
1	Burst	0
2	E	1
3	S0	2
4	Sa	3
5	Sb	5
6	Sc	15
7	Sd	30
8	Im	∞

†All of the templates came from the BC03 stellar population synthesis models assuming a star-formation history which exponentially declines with cosmic time.

‡τ is the e-folding time in the exponentially decreasing star-formation rate.

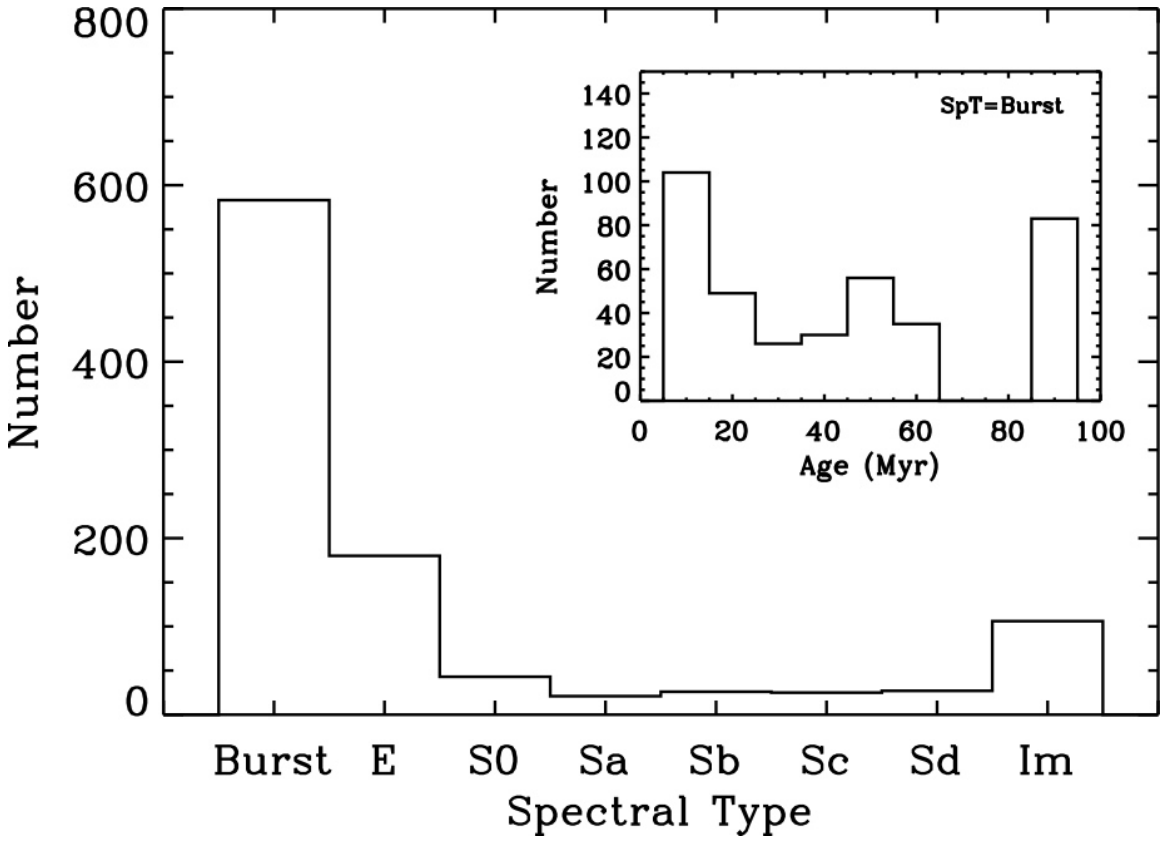

FIG. 4. The *Burst* template is the dominant SED. From the inset, these galaxies are typically very young. This is somewhat expected, since the majority of galaxies at $z \sim 1$ are young and actively forming stars. Since the BC03 templates are tabulated as a function of stellar population age, we require that this age be less than the age of the Universe at any given redshift. This figure is reproduced from Ryan et al. (2007).

2.4. Redshift Quality

We compare our spectro-photometric redshifts to the published spectroscopic measurements (Grazian et al. 2006; Ravikumar et al. 2006; Vanzella et al. 2006). Of the 1308 GRAPES galaxies, only 114 have measured spectroscopic redshifts. For these galaxies, we show the fractional error in $(1+z)$ as a function of the published spectroscopic redshift in Figure 5. The upper and lower panels show this error for different

sets of fluxes used in the redshift computation, as indicated in the upper right corners. Photometric redshifts are the most reliable when a readily identifiable spectral break occurs between two adjacent bandpasses. The 4000 Å and Lyα-breaks will occur in the GRAPES spectra for $0.5 \leq z \leq 1.5$ and $4 \leq z \leq 8$, respectively. Therefore, when either of these breaks occur in the GRAPES spectra, we expect more accurate redshifts. The standard deviation of the fractional error is 0.061 for redshifts computed using only the broadband observations. However, when we use the low-resolution grism in place of the $Vi'z'$ bandpasses the overall redshift uncertainty reduced to 0.046 for the 81 galaxies with $0.5 \leq z \leq 1.5$. Since these low resolution spectra eliminate the need for deep V and z' imaging, this approach requires $\sim$10% the observing time while producing equally or more accurate redshifts by providing more spectral information. In Table 2, we show a representative portion of the final catalog, while the entire ASCII-readable version is available online at http://wwwgrapes.dyndns.org/.

TABLE 2
REPRESENTATIVE† SPECTROPHOTOMETRIC CATALOG

HUDF ID*	x (pix)	y (pix)	RA (h:m:s)	Dec (° ′ ″)	i' (mag)	β	$z_{\rm phot}$	SpT	Age (Gyr)	M_B (mag)
1	4932.88	802.89	3:32:39.7	–27:49:42.5	22.931±0.012	1.14	0.38	5	7.500	–17.75
5	5089.39	753.56	3:32:39.4	–27:49:44.0	26.983±0.110	0.60	0.69	1	0.090	–14.36
7	5052.73	788.94	3:32:39.5	–27:49:42.9	25.367±0.030	1.21	0.61	1	0.004	–16.96
8	5013.85	1274.58	3:32:39.5	–27:49:28.4	21.464±0.003	1.14	0.64	1	1.434	–20.18
13	5108.60	918.70	3:32:39.3	–27:49:39.1	24.985±0.042	1.76	0.52	1	0.360	–16.62

∗Identification from Beckwith et al. (2006).

†The full ascii version is available online at http://wwwgrapes.dyndns.org/

2.5. Summary

We have presented a catalog of 1308 spectro-photometric redshifts for objects that were observed as part of the GRAPES survey of the HUDF. When the low-resolution GRAPES spectra are supplemented with $UJHK_s$ fluxes from other facilities, the standard deviation of the fractional error in $(1+z)$ for the 81 galaxies in the redshift range of $0.5 \leq z \leq 1.5$ is 0.046. While this is only a marginal improvement over traditional photometric redshifts, it requires in total only $\sim$10% the exposure time of those traditional observations. Since the photometric redshift technique is essentially a "break-finding" algorithm, the redshift accuracy is limited by the spectral resolution of the grism data. Therefore, we can estimate spectro-photometric redshifts at a comparable depth and accuracy with only $\simeq 50$ orbits (40 orbits for the grism observations, and 10 orbits for the i'-band image for object selection). This is a critical improvement for wide-angle surveys which may be completely reliant on traditional photometric redshifts. Moreover, the grism observations provide a necessary complement to deep ground-based spectroscopic surveys. Owing to the line-spread function and lower resolution of the grism spectra, determining redshifts from emission lines, in a fashion similar to ground-based surveys, is typically not possible (eg. Xu et al. 2007). However, from the high signal-to-noise continua, the spectral breaks can provide excellent redshift measurements at flux levels not possible from the ground.

The redshift improvement with HST/ACS grism spectroscopy over traditional photometric redshifts on a *per observation basis* has significant promise for future

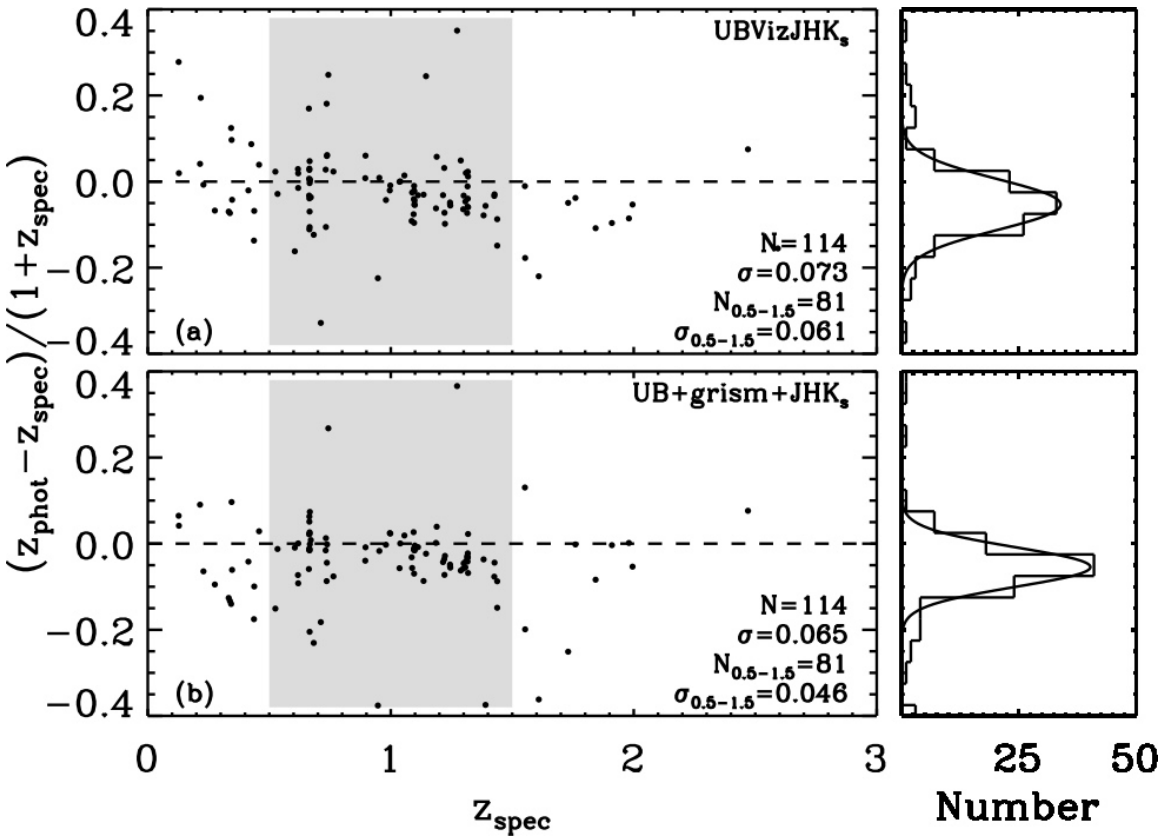

FIG. 5. The bandpasses used for computing the redshifts is indicated in the upper-right of each panel. We tabulate the standard deviation of the fractional error in $(1+z)$ for the shaded redshift range $0.5 \leq z \leq 1.5$, where the 4000 Å break occurs in the ACS grism spectra, and the number of galaxies in the lower-right. The distribution of the residuals is shown to the right of each of the primary panels. Seven catastrophic outliers have been eliminated, since they contained strong emission lines (Xu et al. 2007), which are not accounted for in the stellar population synthesis models. While the broadband data alone can yield good redshift estimates, with the low-resolution grism spectra we further refine the redshifts to $\sigma_{0.5-1.5} = 0.046$. Since these data constitute the extreme case of the best possible data (ultra-deep ACS and NICMOS imaging), the redshift refinement is only marginal. However, we expect a more substantial improvement in the more general case of shallower imaging without available broad spectral coverage. This figure is reproduced from Ryan et al. (2007).

NASA missions, namely the Wide Field Camera 3 upgrade to HST and the planned James Webb Space Telescope (JWST).

CHAPTER 3

The B-band Galaxy Luminosity Function at $z \simeq 1$

3.1. Introduction

The luminosity function (LF) of galaxies represents the distribution of galaxy luminosities in a given redshift interval. Since the LF can be used to constrain galaxy formation models, it has been well studied at both high and low redshifts. While the LF can be computed at any wavelength, it is often studied in the restframe B-band. At $z \simeq 1$ accurate determinations of the B-band LF requires large, deep surveys (eg. Chen et al. 2003; Abraham et al. 2004; Cross et al. 2004; Zucca et al. 2006). In this Chapter, we complement these studies by going nearly two magnitudes fainter in M_B, and accurately determine the shape of the galaxy LF, particularly the faint-end slope.

At the redshifts of interest ($z \simeq 1$), the typical ground-based spectroscopic and photometric surveys are only complete to $M_B \sim -20$ mag and -18 mag, repsectively. Therefore it is necessary to assume a value for the faint-end slope in order to determine the characteristic luminosity (eg. Willmer et al. 2006). In the local Universe, where typical surveys can probe to $M_B \gtrsim -18$ mag, the faint-end slope may depend on the density environment (eg. Trentham 1998) and galaxy colors, spectral type, or morphology (eg. Wolf et al. 2003; Croton et al. 2005; Liu et al. 2008). For the low-luminosity or correspondingly low-mass galaxies, supernovae-driven winds will expel gas which regulates the evolution of the faint-end slope (eg. Dekel & Silk 1986; Khochfar et al. 2007). Futhermore at very high redshifts ($z \gtrsim 6$), the faint-end slope will be critical in determining the source of cosmic reionization (eg. Madau, Haardt, & Rees 1999; Yan & Windhorst 2004a).

3.2. Determination of the Luminosity Functions

We calculate the LF using the $V_{\rm max}$ method (Schmidt 1968; Willmer 1997) in 1.0 mag wide bins from absolute magnitudes measured from `HyperZ` by convolving the best-fit spectrum with the restframe B-bandpass. We construct three redshift intervals: $z = 1.0 \pm 0.2$ which has the best statistics, $z = 0.9 \pm 0.1$, and $z = 1.1 \pm 0.1$ for direct comparison to previous studies. The differential LF is then computed by $\Phi(M)dM = N(M)dM/\Delta V(z_{\rm max})$, where $N(M)dM$ is the number of galaxies with absolute magnitudes between M and $M + dM$, and

$$\Delta V(z_{\rm max}) = \frac{\Omega}{4\pi} \int_{z_{\rm min}}^{z_{\rm max}} C(z, M) \frac{dV}{dz} dz, \tag{3.1}$$

where Ω is the solid angle of the GRAPES survey, $z_{\rm max}$ is the maximum redshift at which a galaxy with an absolute magnitude of M_B would have been detected in the survey, and $C(z, M_B)$ is the survey completeness function. The uncertainties on $\Phi(M)dM$ are computed assuming Poisson noise in the galaxy counts (eg. Wolf et al. 2003).

To estimate the completeness in each absolute magnitude bin, we use a Monte Carlo simulation (Wolf et al. 2003; Budavári et al. 2005). First, we generate random redshifts from a Gaussian distribution of width 0.046, as expected from Figure 5. Next, we count the number of deviates with apparent magnitudes brighter than the survey limit, and take the ratio of the number recovered to the number simulated as the completeness value. This correction is typically less than a factor of 10 for the absolute magnitudes presented.

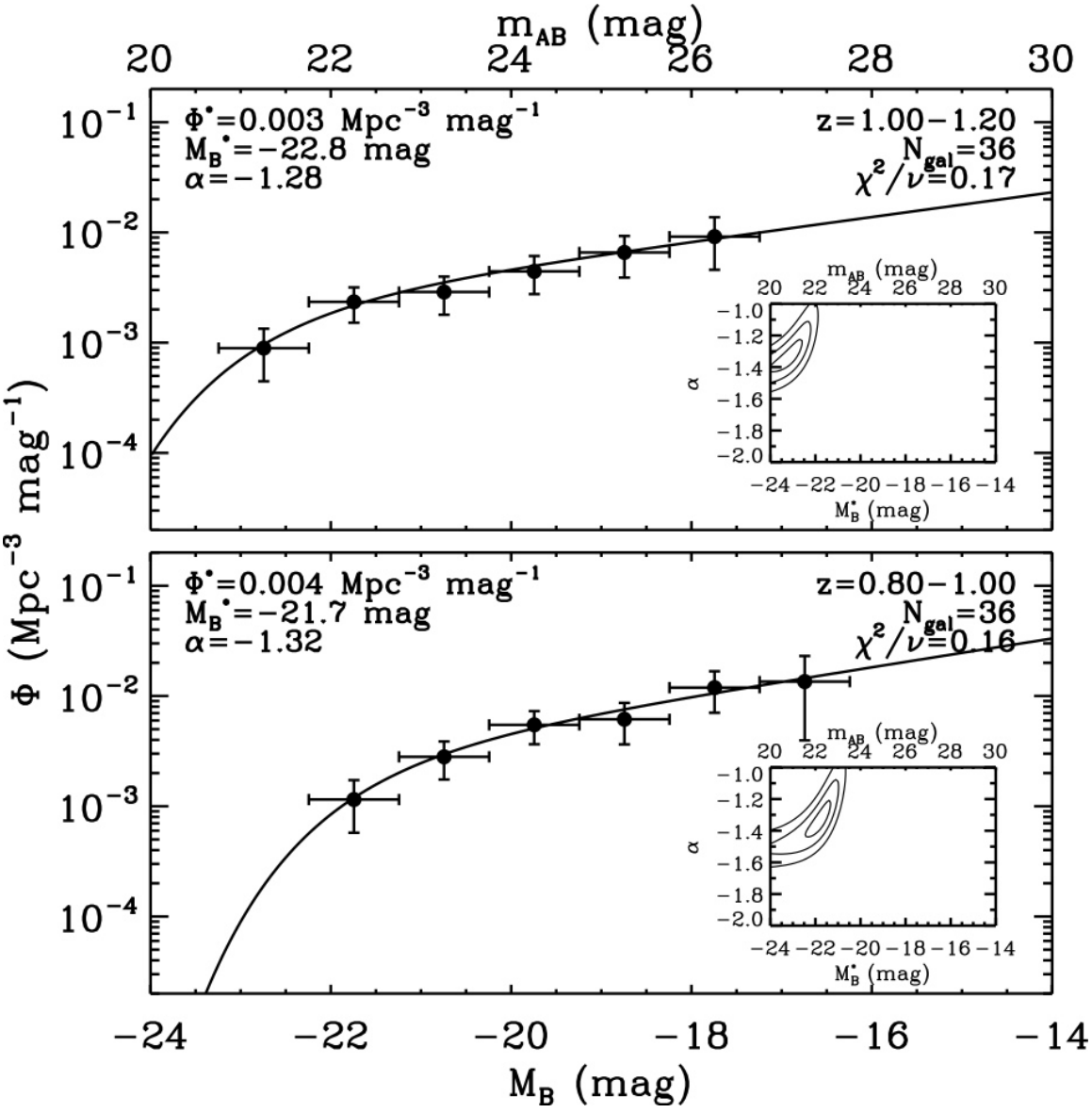

FIG. 6. The two B-band luminosity functions for $z = 0.8$–1.0 (bottom) and $z = 1.0$–1.2 (top) with the corresponding $\Delta\chi^2_\nu$ contours in the $(\alpha - M^*)$ plane. The offset and scatter in Figure 5 will only alter the absolute magnitudes by $\Delta M \simeq 0.1$ mag at these redshifts. Due to the faint flux limit of the GRAPES survey ($z' = 27.2$ mag), we can directly constrain the Schechter parameters in this critical redshift interval for galaxy evolution. While these data can determine $M^* = -22.4 \pm 0.3$ and $\alpha = -1.32 \pm 0.07$ (for $z = 1.0 \pm 0.2$), the normalization (Φ^*) is less certain, since the object selection and contamination in grism spectroscopy poses significant challenges. Therefore, the union of complete ground-based surveys with these deep space-based grism observations provides the most thorough results. This figure is reproduced from Ryan et al. (2007).

TABLE 3
BEST FIT SCHECHTER PARAMETERS

z	$N_{\rm gal}$	Φ^* (10^{-4} Mpc^{-3} mag^{-1})	M_B^* (mag)	α
0.90±0.10	36	35.9±0.2	–21.7±0.9	–1.32±0.19
1.10±0.10	36	25.8±0.1	–22.8±0.5	–1.28±0.10
1.00±0.20	72	26.1±0.1	–22.4±0.3	–1.32±0.07

In Figure 6, we show the LFs for $z = 0.90 \pm 0.10$ (bottom) and $z = 1.10 \pm 0.10$ (top). We model these LFs with a standard Schechter function (Schechter 1976), which is parameterized by the normalization (Φ^*), characteristic absolute magnitude (M^*), and the faint-end slope (α). Additionally in Figure 6, we show the contours for $\Delta\chi^2_\nu$=1, 4, and 9 in the ($\alpha - M^*$) plane as insets. While the total number of galaxies in these redshift bands may be low (~ 10 galaxies per absolute magnitude bin), the GRAPES dataset provides excellent constraints of the Schechter parameters, as in Table 3. Previous studies at these redshifts often use ground-based spectroscopic surveys, which are inherently limited to $M_B \sim -19$ mag (eg. Chen et al. 2003; Abraham et al. 2004; Cross et al. 2004; Zucca et al. 2006). Consequently, it has been customary in such studies to *assume* a faint-end slope of $\alpha \simeq -1.3$ (eg. Willmer et al. 2006). However, the GRAPES observations provide a means to *measure* the faint-end slope of $\alpha = -1.32 \pm 0.07$ at $z = 1.0 \pm 0.2$. It is reassuring that the assumption of $\alpha \simeq -1.3$ at these redshifts was indeed correct.

3.3. Redshift Evolution of the Faint-end LF Slope

The hierarchical formation scenario asserts that many dwarf galaxies at high redshift will merge over cosmic time. This effect should result in an increased number of dwarf galaxies at higher redshift and may be observed as a steepening of the faint-end slope. In Figure 7, we show the redshift dependence of the faint-end slope compiled from numerous studies. These studies include, but are not limited to, the largest ground-based redshift surveys (eg. Norberg et al. 2002; Blanton et al. 2003), the deepest HST surveys (eg. Beckwith et al. 2006), and nearby GALEX surveys (eg. Budavári et al. 2005; Wyder et al. 2005). While each survey has unique selection effects and observational biases, many problems can be mitigated by requiring two criteria of the dataset: a sufficient amount of data *fainter* than M^*, and a minimal reliance on k-corrections. Ilbert et al. (2004) emphasize that only surveys for which $(1 + z_{\rm obs}) \sim \lambda^S/\lambda^{\rm REF}$, where $z_{\rm obs}$ is the redshift of the LF, and λ^S and $\lambda^{\rm REF}$ are the wavelengths at which the galaxies are selected and the LF is computed, respectively, can reliably infer the faint-end slope. When the Ilbert et al. (2004) condition is met, the k-correction is minimized. For uniformity, we only show values of α which meet these requirements. In Figure 7, the red and blue open circles indicate the faint-end slopes measured in the restframe B-band and far UV (FUV$\simeq$1700 Å), respectively. Our GRAPES observation is indicated as the filled red circle at $z = 1.0 \pm 0.2$.

From Figure 7, the faint-end slope clearly depends on redshift in the manner suggested in the hierarchical scenario, where many low-mass galaxies at high redshift merge throughout cosmic time into the massive galaxies of today. We parameterize

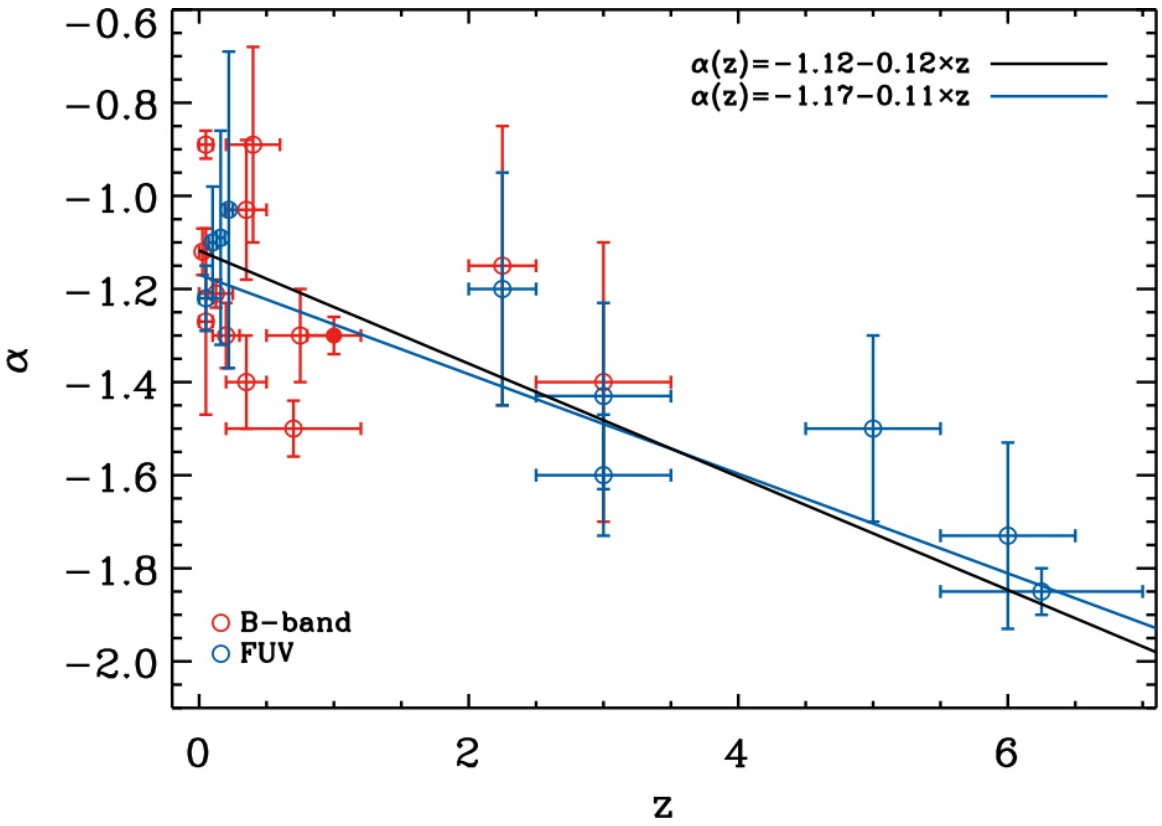

FIG. 7. We show 23 published slopes from 18 sources, including this work. While there are many more values which could have been shown, we require each survey to have measured the LF ∼2 mag fainter than M^*, and optimally selected their galaxies to minimize the k-correction (Ilbert et al. 2004) to ensure uniform and reliable estimates of the faint-end LF slope. The open red points indicate measurements made in the restframe B-band (Lin et al. 1997; Sawicki, Lin, & Yee 1997; Marzke et al. 1998; Fried et al. 2001; Norberg et al. 2002; Blanton et al. 2003; Driver & de Propris 2003; Wolf et al. 2003; Marchesini et al. 2007). The open blue points represent the restframe FUV (Steidel et al. 1999; Iwata et al. 2003; Yan & Windhorst 2004b; Budavári et al. 2005; Wyder et al. 2005; Bouwens et al. 2006; Sawicki & Thompson 2006). The filled red point at $z=1.0\pm0.2$ is the result of this work. This suggests that dwarf galaxies were more numerous at higher redshift as predicted in the hierarchical formation paradigm. This figure is reproduced from Ryan et al. (2007).

the redshift dependence of the faint-end slope as $\alpha(z) = a + bz$, and give the best fit models for the entire dataset and the FUV as black and blue lines, respectively (see Figure 7). While the two fits are mutually consistent, the significant scatter warrants further study. There are many effects which could contribute to this scatter: differences in the restframe bandpass, type-dependent evolution, galaxy clustering and large-scale structure, and non-uniform sample selections.

3.4. Implications for Galaxy Evolution

This steepening of the faint-end slope (α) with increasing redshift has a number of consequences for our understanding of galaxy formation and evolution. To explore some of the possible effects, Khochfar et al. (2007) develop a semi-analytic model of galaxy formation with a standard merger tree for the dark matter haloes (Somerville & Kolatt 1999). Since their focus was to study the faint-end of the luminosity function, physical processes which solely affect the bright-end were omitted, such as AGN feedback (eg. Bower et al. 2006) or environmental dependences (Khochfar, Silk, Windhorst, & Ryan 2007). To incorporate the stellar populations, they adopt standard prescriptions for the star formation as the global Schmidt-Kennicutt law (Kennicutt 1998), the reheating from the associated supernovae (Dekel & Silk 1986), and the stellar population models of Bruzual & Charlot (2003).

With this simulation, they confirm early results that the flattening of the faint-end slope with respect to the dark matter mass function can be well explained by the supernovae reheating of the cold gas (eg. Khochfar & Burkert 2001). Futhermore, they find that faint-end slope steepens at high redshift due to evolution of underlying

dark matter mass function (Khochfar et al. 2007). In Figure 8, I show Figure 2 taken from Khochfar et al. (2007) which plots the same data and linear fit (now two dashed lines) as in Figure 7. The shaded region shows range of linear fits obtained by varying the star formation and supernovae efficiencies (a_* and $\epsilon_{\rm SN}$, respectively). They argue that at $z \geq z_* \simeq 2$, the faint-end slope is dominated by galaxies which end up in present day galaxy clusters. This transition redshift is somewhat dependent on σ_8, the normalization of the power spectrum at 8 h^{-1} Mpc.

3.5. Summary

Since the HST-ACS grism observations (Chapter 2) allow for significantly deeper spectral observations, we are able to probe the faint-end of the B-band luminosity function at redshifts that are not easily probed from the ground. Owing to this enhanced depth, we are able to accurately constrain the faint-end slope by reaching as faint as $M_B \simeq -18$ mag at $z = 1.0 \pm 0.2$, nearly two magnitudes fainter than previous studies at comparable redshifts. At this redshift, we determine that the faint-end LF slope is $\alpha = -1.32 \pm 0.07$.

In the hierarchical formation scenario, galaxies are expected to evolve by successive mergers throughout cosmic time. Therefore, we naïvely expect to find fewer dwarf galaxies at lower redshifts, which can be directly measured in terms of the redshift evolution of the Schechter parameters, particularly its faint-end slope. The data presented here provide a measurement of the faint-end slope in the critical redshift range of $0.5 \leq z \leq 1.5$, where the cosmic star formation rate density is substantially changing (eg. Hopkins & Beacom 2006). When our measurement of the faint-end slope

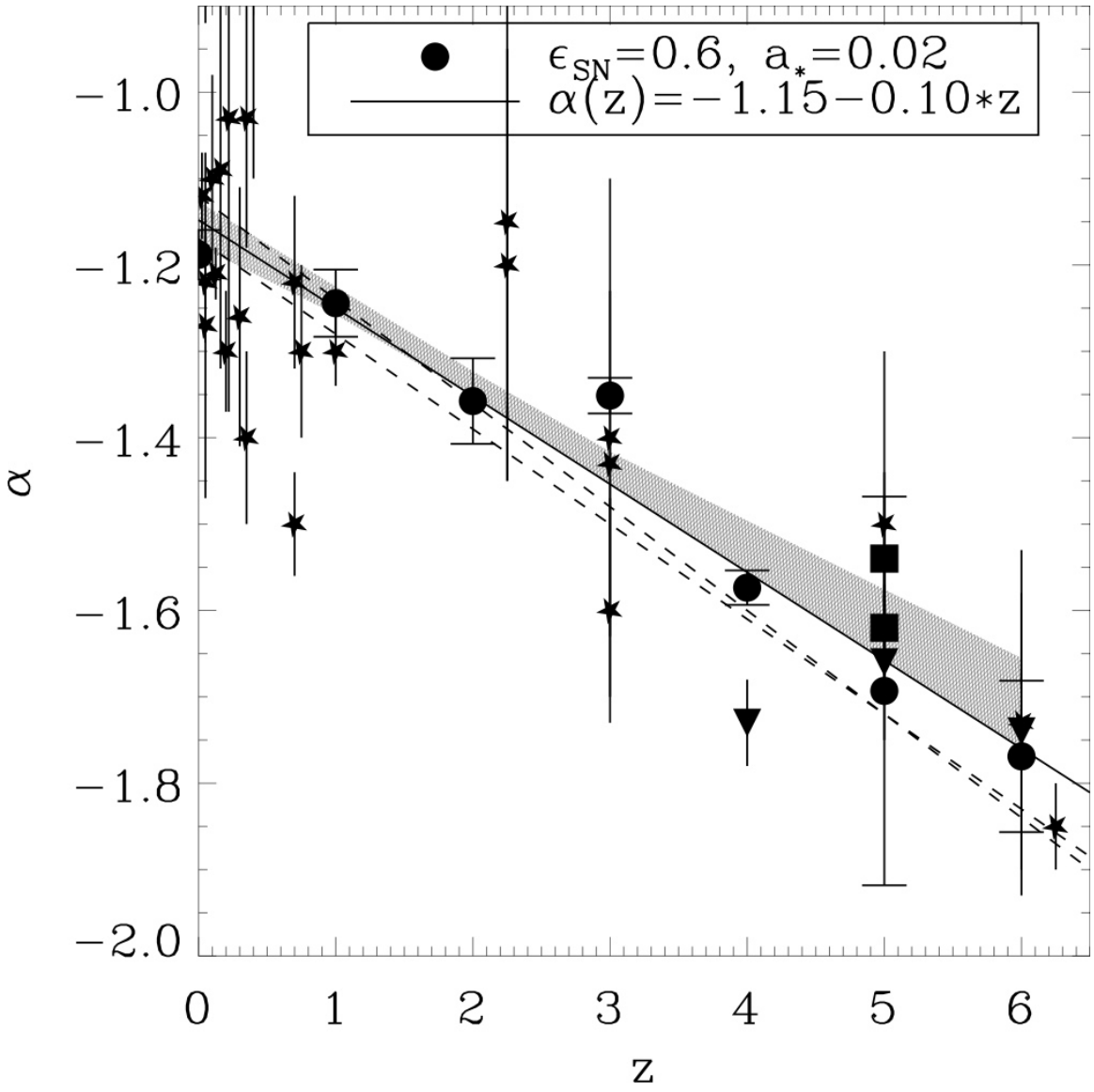

FIG. 8. The filled circles show the simulation results for $\epsilon_{\rm SN} = 0.6$ and $a_* = 0.02$ and the best-fit model to the simulated data as a solid line (taken from Khochfar, Silk, Windhorst, & Ryan 2007). The stars show the data compiled in Figure 7 with additional data from Oesch et al. (2007, squares) and Bouwens et al. (2007, downward triangles). The shaded region shows the range of linear fits for varied star formation efficiencies (a_*) and supernovae feedback ($\epsilon_{\rm SN}$). This figure is reproduced from Khochfar et al. (2007).

is compared to numerous published studies, we find strong evidence for a redshift-dependent faint-end slope. While previous authors have suggested a similar trend (eg. Arnouts et al. 2005; Zucca et al. 2006), this compilation of published results provides both increased statistics and a broader redshift range.

The redshift dependence of the other two Schechter parameters (Φ^* and M^*) has been discussed by various authors. Lin et al. (1999) study the redshift evolution of the B-band galaxy luminosity function, and propose the parameterizations of $M^*(z) = M_0^* - Qz$ and $\rho(z) = \rho_0 10^{0.4Pz}$, where $\rho \equiv \int \Phi(M) dM$. If the faint-end slope is constant with redshift (ie. $\alpha(z) = \alpha_0$), then ρ and Φ^* are essentially equivalent. These parameters (P, Q) provide a simple way of quantifying galaxy evolution, and can be determined as a function of galaxy type. For $q_0 = 0.1$, Lin et al. (1999) find $(P, Q) = (-1.00 \pm 0.40, 1.72 \pm 0.41)$ for the combination of early- and intermediate-type galaxies. However, Fried et al. (2001) parameterize Φ^* linearly on redshift: $\Phi^*(z) = a + b \times (1 + z)$, where the coefficients (a, b) have only a minimal dependence on galaxy type. Nonetheless, an obvious trend based on the observed evolution of the Schechter parameters is emerging: the galaxy luminosity function is shallower, and has a brighter characteristic absolute magnitude at low redshift.

CHAPTER 4

The Galaxy Major Merger Rate of Massive Galaxies at $z \simeq 1$

4.1. Introduction

The hierarchical formation scenario suggests that galaxy merging is the driving mechanism in galaxy formation (eg. White & Frenk 1991; Kauffmann, White, & Guiderdoni 1993). Since galaxy merging has been linked to numerous astrophysical processes, including star-formation and the fueling of a supermassive black hole (SMBH), which triggers an active galactic nucleus (AGN), the merger history of galaxies is critical for a complete understanding of galaxy evolution.

The redshift evolution of the galaxy merger fraction has been well studied for $z \lesssim 1$, and is roughly proportional to $(1+z)^m$, where typically $1 \leq m \leq 4$ (Zepf & Koo 1989; Burkey et al. 1994; Carlberg, Pritchet, & Infante 1994; Yee & Ellingson 1995; Neuschaefer et al. 1997; Patton et al. 1997; Le Fèvre et al. 2000; Patton et al. 2002; Lin et al. 2004; Xu, Sun, & He 2004; Bell et al. 2006; Kartaltepe et al. 2007). Toomre (1977) predicted the galaxy pair fraction to be proportional to the matter space density at low redshift. Carlberg (1991) refined this idea to show that the power-law index should be somewhat sensitive to the Cosmological Constant. Based on N-body simulations, Berrier et al. (2006) argue that while the galaxy merger rate per halo is increasing with redshift, the number of halos massive enough to host a galaxy pair is decreasing. This balance will result in a flattening of the high redshift pair counts, which is consistent with some high redshift observations (eg. Lin et al. 2004). Fakhouri & Ma (2008) suggest that this power-law form is a particular representation of a universal merger rate which scales as a power-law with the progenitor mass ratio, and depends only weakly on the halo mass. Additionally, Conselice (2006) has

suggested that the merger fraction may peak at some critical redshift. However, until now there have been very few observational studies for $z \gtrsim 1$ to constrain the redshift of this possible peak, and hence the detailed physics of the galaxy merging at high redshift is still uncertain.

The standard hierarchical formation model has been modified to incorporate the feedback effects of a central SMBH (eg. Silk & Rees 1998). Hydrodynamical simulations have suggested that as galaxies merge, they evolve into a starburst system, and a substantial amount of gas is eventually funneled onto their SMBHs. This triggers a visible AGN typically 1–2 Gyr after the onset of the merger (Springel, Di Matteo, & Hernquist 2005a). While previous authors have discussed an evolutionary link between mergers and starburst galaxies (eg. Larson & Tinsley 1978; Sanders & Mirabel 1996; Bell et al. 2005), this "duty cycle" of merging, followed by a starburst, followed by an AGN, has only recently been suggested (Hopkins et al. 2006). This formation scheme implies that we should observe similarities in the redshift evolution of merging galaxies, their star-formation history (eg. Madau et al. 1996), the mass assembly in galaxies (eg. Dickinson et al. 2003), their AGN activity (eg. Ueda et al. 2003; Hasinger, Miyaji, & Schmidt 2005; Schneider et al. 2005), and the relevant galaxy morphologies (eg. Driver et al. 1995b; Abraham et al. 1996). Since these other phenomena have been well studied at $z \gtrsim 1$, we desire corresponding measurements of galaxy merging at comparable redshifts, which is the focus of this Chapter.

While there may be some convergence on the theoretical front, there is little consensus regarding the observational connections between merging and active galax-

ies. In general, AGN host galaxies do not exhibit strong merger-type morphologies (eg. Bahcall et al. 1997; Cohen et al. 2006; Guyon, Sanders, & Stockton 2006) or show enhanced image asymmetry (Grogin et al. 2005). Conversely, Canalizo et al. (2007) find evidence for recent merger activity in the quasar host galaxy MC2 1635+119, which was previously classified as an undisturbed elliptical galaxy. Some of this disagreement may be resolved in the context of the above duty cycle, wherein the morphological indications of the recent merger have subsided by the time the AGN is observationally identified. This debate will surely continue owing, in part, to the difficulties interpreting morphological studies of faint galaxies (eg. de Propris et al. 2007).

This Chapter is organized as follows: In § 4.2 we describe the dataset and the mass estimates, in § 4.3 we outline our merger selection, in § 4.4 we measure the merger fraction and number density, in § 4.5 we compare this study to published work, and in § 4.6 we conclude with a general discussion of the result in the context of galaxy evolution. We adopt the three-year results from the *Wilkinson Microwave Anisotropy Probe* (Spergel et al. 2007), where $\Omega_0 = 0.24$, $\Omega_\Lambda = 0.76$, and $H_0 = 100h$ km s^{-1} Mpc^{-1} with $h = 0.73$. All magnitudes quoted herein are in the AB system (Oke & Gunn 1983).

4.2. Data

The deep fields observed by the *Hubble Space Telescope* (HST) provide an unprecedented view of the distant universe ($z \gtrsim 1$), and are therefore the ideal datasets for studying the high redshift evolution of the galaxy merger rate. The GRism ACS

Program for Extragalactic Science (GRAPES; Pirzkal et al. 2004) has provided low-resolution ($R \simeq 100$) spectroscopy of 1400 objects with $z' \leq 27.2$ mag in the Hubble Ultra Deep Field (HUDF; Beckwith et al. 2006). From these data, Ryan et al. (2007, Chapter 2) computed spectro-photometric redshifts for 1308 galaxies at $z \lesssim 5$. When the Balmer or 4000 Å break occurs in these optical ACS spectra (for $0.5 \leq z \leq 1.5$), the standard deviation in $(z_{\rm phot} - z_{\rm spec})/(1 + z_{\rm spec})$ is 0.037, and it is only 0.050 for $z \geq 1.5$, which make these among the most accurate photometric redshifts computed to date, using the standard maximum-likelihood technique (Bolzonella, Miralles, & Pelló 2000).

Since the primary aim of this work is to measure the high redshift evolution of the galaxy merger rate, we require a set of criteria to select our merger candidates. While this has traditionally been performed using the restframe luminosity, we will select our systems based on their mass. We desire their total gravitational mass, since it is expected to drive galaxy merging (eg. Khochfar & Burkert 2001). However, since this mass is exceedingly difficult to determine for a large sample of faint galaxies, we will adopt the stellar mass as our selection quantity.

To determine the required stellar masses of our sample, we fit the combination of GRAPES spectra and broadband observations in the B-, J-, and H-bands with a grid of stellar population synthesis models (Bruzual & Charlot 2003, BC03 hereafter). The masses are determined by minimizing the reduced χ^2 between the spectrophotometry and these models, following the method of Papovich, Dickinson, & Ferguson (2001). By parameterizing the star-formation history of these galaxies

as $\Psi(t) = \Psi_0 e^{-t/\tau}$, our model grid consists of three parameters: the extinction in the restframe V-band A_V, the e-folding time in the star-formation history τ, and stellar population age t. If we assume a Salpeter initial mass function (Salpeter 1955) and solar metallicity, then this parameter space is populated by $\sim 4 \times 10^4$ independent models. By varying the values of the grid points, we estimate the uncertainty on the stellar masses to be $\lesssim 15\%$. In Figure 9, we show the stellar mass as a function of redshift for these galaxies. The different tracks show the mass of a maximally old stellar population for the various values of τ listed in the lower-right corner. The shaded region shows the mass selection for the primary galaxies, which is $\sim 95\%$ complete for $z' < 27.2$ mag. The darker area indicates the selection region for the lower mass companion galaxies to be discussed below.

4.3. Identification of Merging Galaxies

Since we have reasonable redshift information for the entire sample of galaxies, it is natural that we adopt the dynamically close pair method (eg. Carlberg, Pritchet, & Infante 1994). However, since our redshift uncertainty is roughly a factor of 10 larger than that of a traditional spectroscopic survey, our approach will be somewhat akin to the more common pair count analysis (eg. Zepf & Koo 1989). This technique has several key virtues not present in other approaches: it has simple and well understood statistics to compute (Abraham 1999), and does not rely on calibration datasets (de Propris et al. 2007). Patton et al. (2000, P2000 hereafter) demonstrate that the galaxy merger rate ($\mathcal{R}_{\rm mg}$) can be computed from the galaxy merger or pair

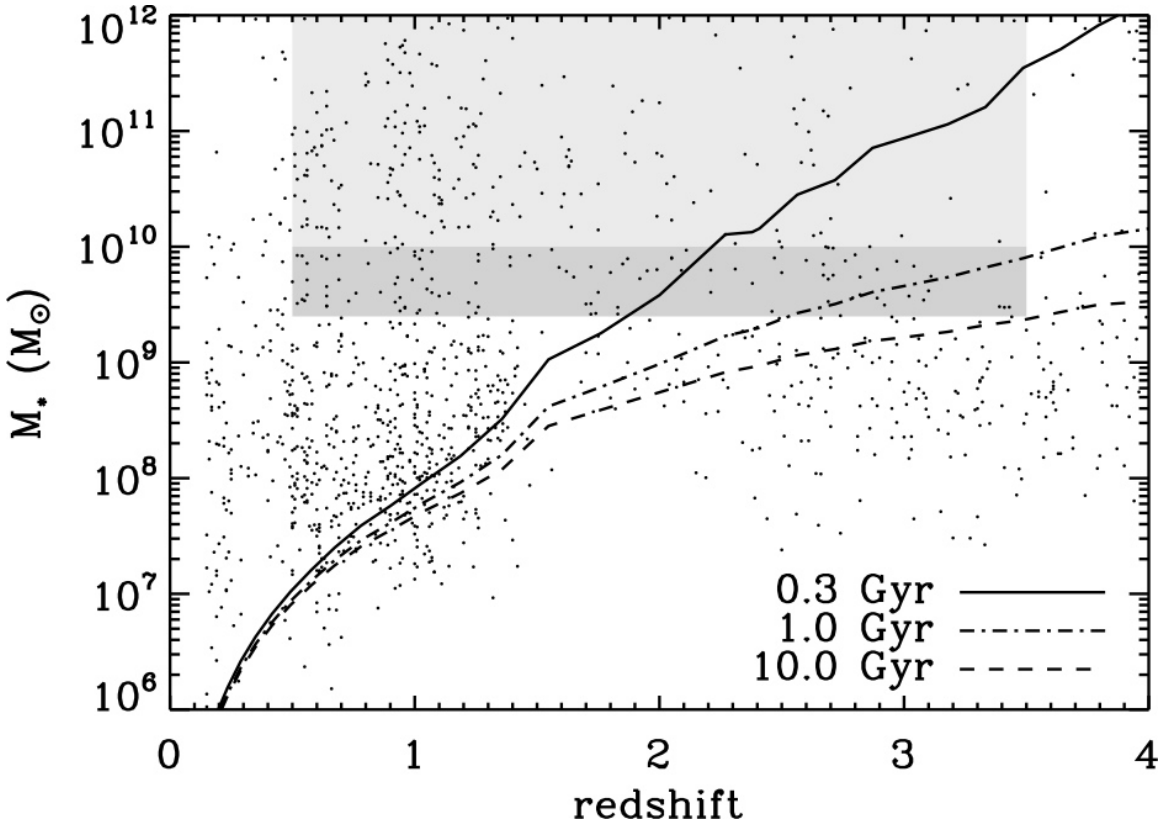

FIG. 9. We show the computed stellar mass as a function of the spectro-photometric redshift. The lightly shaded region indicates the volume-limited, mass selection region for the primary galaxies, while the darker region shows the possible selection of companion galaxies. In total, $\sim 95\%$ of the galaxies with $z' \leq 27.2$ mag identified in the HUDF by Beckwith et al. (2006) are represented here (see Figure 10) with 230 of these meeting the selection criteria discussed in § 4.3. The various lines show the mass of a maximally old, passively-evolving stellar population with an e-folding time in the star-formation rate given in the lower-right corner. This figure is reproduced from Ryan et al. (2008a).

fraction (f) and the galaxy number density (n) as $\mathcal{R}_{\rm mg} = fn\tau_{\rm mg}^{-1}$, where $\tau_{\rm mg}$ is the typical merger timescale.

4.3.1. *Pair Criteria*

Using the redshift catalog of Ryan et al. (2007, Chapter 2), we require the following four criteria to be satisfied to identify a galaxy pair as a merger system: (1) at least one neighboring galaxy $\leq$20 h^{-1} kpc away to ensure that close galaxy pairs will merge (eg. de Propris et al. 2005; Bell et al. 2006) on a timescale $\tau_{\rm mg} \lesssim 0.5$ Gyr (eg. Khochfar & Burkert 2001; Patton et al. 2002); (2) we require the mass ratio of primary galaxy to any nearby companion to be $\leq 4:1$, which is consistent with a flux ratio between the galaxies of $\lesssim 1.5$ mag assuming that they have the same mass-to-light ratio; (3) we require the stellar mass of the primary galaxy to be $M_* \geq 10^{10}$ $\mathrm{M}_\odot$; and (4) we require the redshifts of the primary and the companion to agree within the 95% confidence interval of the spectro-photometric redshifts of Ryan et al. (2007).

4.3.2. *Accounting for the Flux and Mass Limit*

Since the GRAPES survey is complete to very faint flux levels (see Figure 10), we may expect it to be volume-limited at high redshift and that no completeness corrections to the pair statistics are needed. Therefore to investigate this issue, we show the absolute B-band magnitude as a function of the spectro-photometric redshift in Figure 11, where the solid line shows our flux limit of $z' \simeq 27.2$ mag for a flat spectrum in f_ν following Driver (1999). While this figure shows the expected volume-limited behavior (eg. de Propris et al. 2005), there is a more subtle question to address as this is a mass-selected sample: *Is there a population of galaxies which are fainter*

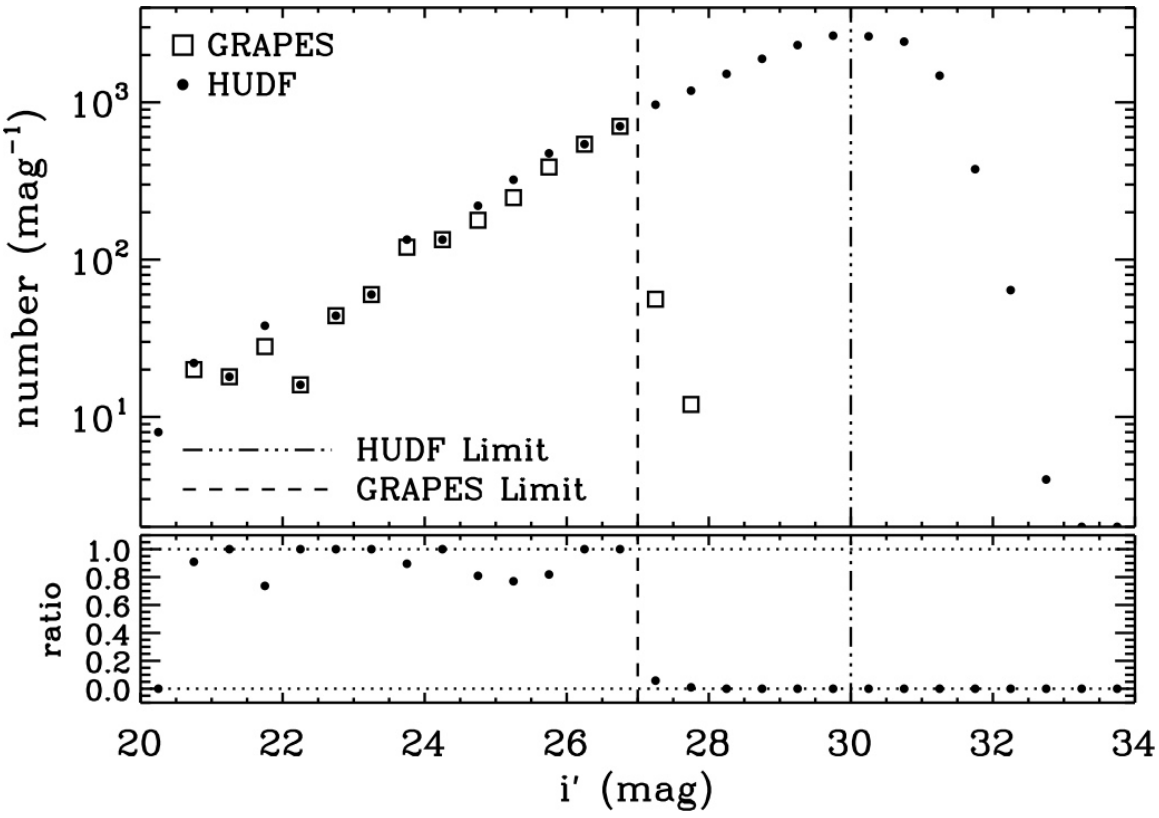

FIG. 10. The GRAPES objects were selected from the HUDF to have $z' \leq 27.2$ mag, and this diagram illustrates that the survey is $\geq 95\%$ complete at these flux levels. In the lower panel, we show the ratio of the number counts of the GRAPES survey to all objects in the HUDF. This figure is reproduced from Ryan et al. (2008a)

than our flux limit and more massive than our mass limit? If such a population exists, then our mass selection would be incomplete for these galaxies (Dickinson et al. 2003). At the redshifts of interest, such objects must have a relatively high stellar mass-to-light ratio ($\Upsilon_{*,B} \gtrsim 2$ $M_\odot$ $L_\odot^{-1}$), and would likely very red in the HST images.

To find similar dark, red galaxies at $1.5 \lesssim z \lesssim 2.4$, Daddi et al. (2004) have developed a selection criteria based on the observed $(B - z')$ and $(z' - K)$ colors (the BzK method). When this is applied to the HUDF, Daddi et al. (2005) identify

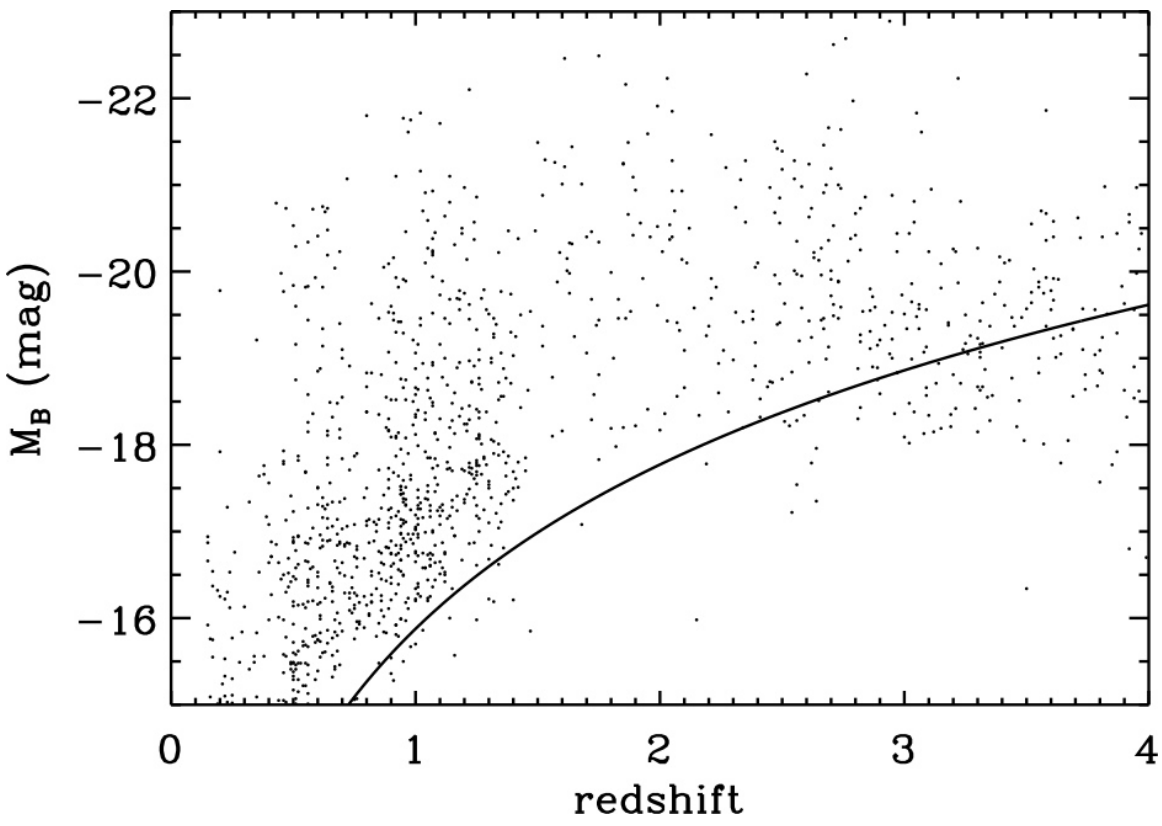

FIG. 11. This figure is shown only for comparison and is not used in the merger candidate selection. The solid line shows the contour of constant apparent magnitude of $z' \simeq 27.2$ mag following Driver (1999). The majority of our galaxies have ages $\lesssim$500 Myr, which implies their median stellar mass-to-light ratio is $\Upsilon_{*,B} \simeq 0.5\ \mathrm{M}_{\odot}\ \mathrm{L}_{\odot}^{-1}$. Therefore, the mass limit of $M_* \geq 10^{10}\ \mathrm{M}_{\odot}$ roughly corresponds to $M_B \leq -20.5$ mag, which is comparable to the luminosity limit imposed by various authors (eg. Patton et al. 1997; Le Fèvre et al. 2000) at lower redshifts. This figure is reproduced from Ryan et al. (2008a).

only seven old, passively-evolving galaxies with $K<23$ mag. They argue that these systems must have been formed in a relatively quick burst, since they emit little restframe ultraviolet flux. While these objects would satisify the above mass-to-light ratio criterion, they are brighter than our flux limit, and are hence included in our redshift survey. Therefore, to estimate the number of galaxies that satisfy this mass-to-light criterion that are fainter than our flux limit, we must perform a similar analysis on deeper data. However Daddi et al. (2005) analyzed the deepest K-band imaging of the HUDF available, and we must turn to a deeper dataset. We will adopt the NICMOS imaging in the H-band of the HUDF (Thompson et al. 2005), which is $\sim$4 mag deeper than the K-band data used by Daddi et al. (2005). To ensure a comparable color selection, we will assume that these galaxies have a typical infrared color of $(H-K)\sim$0.8 mag (Förster Schreiber et al. 2004). In Figure 12, we show the corresponding BzH color selection for the objects in NICMOS imaging with fluxes taken from Coe et al. (2006). The shaded polygon shows the BzH selection region defined by $(z'-H)-(B-z')<-0.2-(H-K)$ and $(z'-H)>2.5-(H-K)$. The open squares represent all objects satisfying these BzH criteria, while the open circles show the five objects of Daddi et al. (2005) which are in this portion of the HUDF. The various lines represent the BC03 stellar population models with exponentially declining star-formation histories whose e-folding times (τ) are listed in the lower-right. The BzH selection identifies only nine galaxies, or 1% of all objects with $z\lesssim 28.5$ mag, which are expected to have burst-type star-formation histories ($\tau\lesssim$ 0.3 Gyr Daddi et al. 2005). Since we recover 4/5 objects from Daddi et al. (2005), we

conclude that this is a viable method to identify maximally old, passively-evolving galaxies which would satisfy the mass-to-light requirement. Furthermore galaxies with $\tau \lesssim 0.3$ Gyr are rather rare, we will correct the pair statistics using stellar populations with $\tau \geq 0.3$ Gyr.

To correct the observed pair counts, we will adopt the method of P2000, and for brevity only highlight our modifications for the mass-selection and give the essential details. In the P2000 method, one computes the maximal k-correction from a set of galaxy SED templates to derive the low-luminosity limit, when selecting objects based on absolute magnitudes (see Figures 1 and 2 from Patton et al. 2002). However, since we select candidates based on their stellar mass, we must determine the corresponding maximal mass limit. While Patton et al. (2002) adopt the empirical templates of Coleman, Wu, & Weedman (1980), we choose the stellar population synthesis models of BC03. As in § 4.2, we parameterize the star-formation rate as $\Psi(t;\tau) \propto e^{-t/\tau}$, and restrict $\tau \geq 0.3$ Gyr, since objects with $\tau \leq 0.3$ Gyr are extremely rare (as discussed above). Since the aim is to generate a population of maximal stellar mass, we set $t = T(z)$, where $T(z)$ is the age of the Universe at redshift z.

We define the stellar mass limit to be the more massive between the fiducial limit ($M_{*,0}$) and the maximal mass model ($M_*(z;\tau)$):

$$M_*^{\rm lim}(z) = \max\left[M_{*,0}, M_*(z;\tau)\right]. \tag{4.1}$$

With this mass selection, we compute the selection function to correct the counts of the flux-limited survey as:

$$S_N(z) = \frac{\int_{M_{*,0}}^{M_*^{\rm lim}(z)} \Phi(M_*, z) dM_*}{\int_{M_{*,0}}^{\infty} \Phi(M_*, z) dM_*}, \tag{4.2}$$

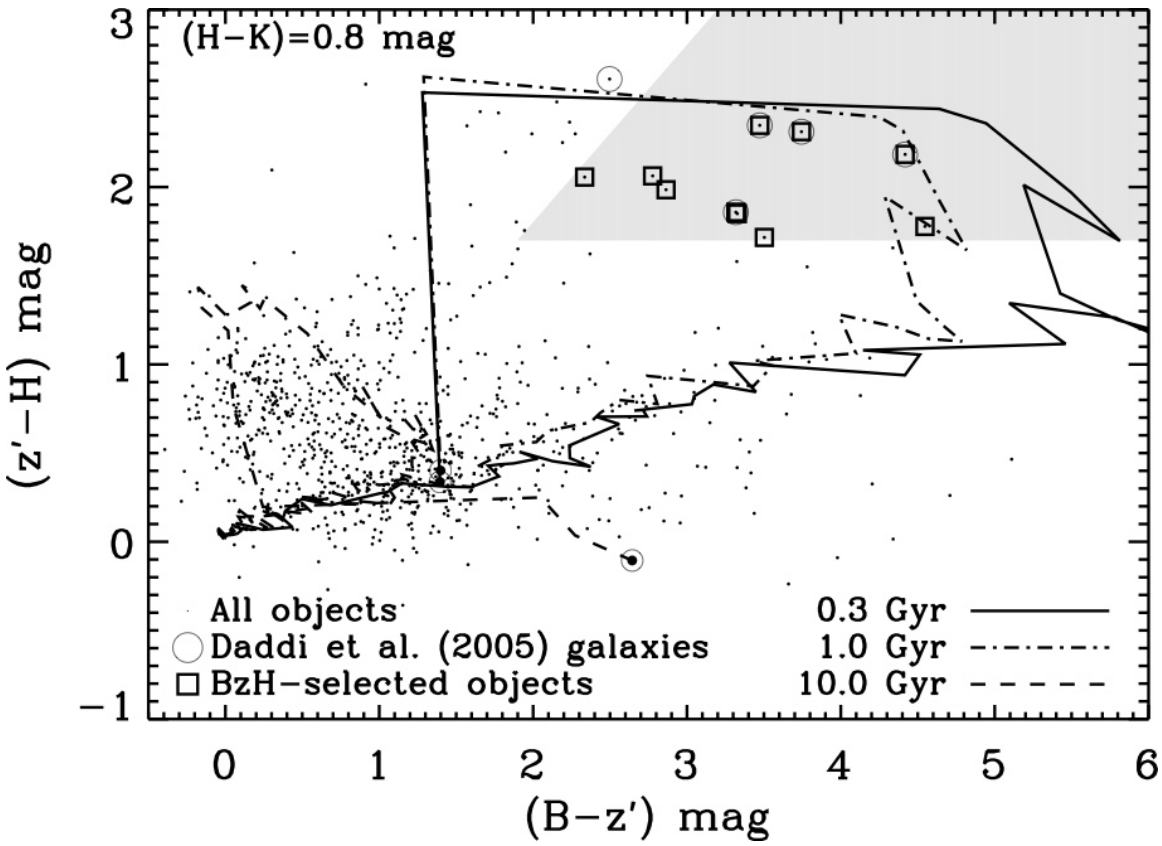

FIG. 12. By assuming $(H-K)\simeq 0.8$ mag (Förster Schreiber et al. 2004), we perform a similar analysis to Daddi et al. (2005) on the much deeper NICMOS imaging in the HUDF, to estimate the range of star-formation histories applicable to these redshifts. The shaded region represents the BzH selection discussed in § 4.3.2. As in Figure 9, the different lines represent maximally old, passively-evolving stellar populations, denoted by the e-folding time in their star-formation rate in the lower-right. The "bullseye" marks the birth of the populations at $z_{\rm form}\rightarrow\infty$. As discussed in § 4.3.2, maximally old galaxies with $\tau\leq 0.3$ Gyr are exceedingly rare and would appear in the shaded, BzH polygon. Therefore, when correcting our pair counts following the P2000 method, we adopt BC03 models appropriate for our sample ($\tau\geq 0.3$ Gyr). This figure is reproduced from Ryan et al. (2008a).

where $\Phi(M_*, z)$ is the galaxy mass function (not to be confused with the luminosity function). Elsner, Feulner, & Hopp (2008) show that the galaxy mass function can be well modeled as the Schechter function (Schechter 1976) with $M_*^* \sim 10^{11.5}$ $M_\odot$ and $\alpha \sim -1.36$ for $z \lesssim 5$. Finally, the optimal weights to apply to the pair statistics will be $w_N(z) \propto S_N(z)^{-1}$, where the various remaining terms (such as boundary effects and spectroscopic completeness) are computed following Patton et al. (2002). Using these optimal weights, the number of close companions for the ith primary galaxy is computed as $N_{c,i} = \sum_j w_{N_2}(z_j)$, where j runs over the companions which satisfy the above merger criteria. Finally, the mean number of close companions per primary galaxy is found as

$$N_c = \frac{\sum_i w_{N_1}(z_i) N_{c,i}}{\sum_i w_{N_1}(z_i)}, \tag{4.3}$$

following the notation of Patton et al. (2002).

4.3.3. *Error Budget*

While it may be appropriate to assume Poisson uncertainties on the pair counts, we require a more detailed analysis to incorporate the effects of the redshift uncertainties. Despite having spectrophotometric redshifts for each component of the merging pair, the relatively large uncertainties on the proper distance ($\delta d_p \lesssim 500$ Mpc) can lead to false positives. To estimate the magnitude of this effect, we randomize the redshifts and masses in such a manner to preserve the selection discussed above, and recompute the resulting pair counts. In 10^3 realizations of the redshift catalog, we estimate that $\lesssim 1.5$ pairs per redshift bin may arise from superpositions identified by erroneous redshifts estimates. This approach allows us to bootstrap the uncertainties

on the pair counts to include the effects of Poisson shot noise, chance superpositions, and the spectrophotometric redshift uncertainties.

Since the HUDF covers $\simeq 3\farcm3 \times 3\farcm3$, the uncertainties resulting from cosmic variance must also be addressed. By assuming that the spatial correlation function of the galaxies is $\xi(r) \propto (r/r_0)^{-\gamma}$, the relative cosmic variance in the number counts is given as $\sigma_v^2 = 1.45(V/r_0^3)^{-\gamma/3}$ for cell volume V, correlation length r_0, and $\gamma = 1.8$ (Somerville et al. 2004). For comparable sampled volumes, Beckwith et al. (2006) estimate the cosmic variance to be $\sigma_v \simeq 0.17$ for the HUDF cell geometry.

4.4. Redshift Evolution

In Figure 14, we show the resulting galaxy merger fraction as a function of $(1 + z)$ as filled circles with uncertainties that reflect the contributions from chance superpositions, cosmic variance, redshift uncertainty, and Poisson shot noise. Since these galaxies are typically very young (age $\lesssim$500 Myr as inferred from the SED fitting described in § 4.2), their median stellar mass-to-light ratio in the restframe B-band is $\Upsilon_{*,B} \simeq 0.5$ $M_\odot$ $L_\odot^{-1}$ (see Figure 13), and therefore the mass limit of $M_{*,0} \geq 10^{10}$ $M_\odot$ roughly corresponds to $M_B \lesssim -20.5$ mag. Since this luminosity limit is similar to that imposed by Patton et al. (1997) and Le Fèvre et al. (2000), we show those measurements for comparison as open triangles and diamonds, respectively. We show the standard power-law parameterization of $f(z) = 0.02 \times (1 + z)^3$ as a dashed line. While this model can fit the low redshift ($z \lesssim 1$) observations, it fails to reproduce our higher redshift ($z \gtrsim 1$) data. Therefore, we also show the empirical formed proposed

by Conselice (2006) of

$$f(z) = a(1+z)^b e^{-c(1+z)}, \tag{4.4}$$

as a solid line. Using a standard least-squares technique, we find $a = 0.44 \pm 0.04$, $b = 7.0 \pm 0.6$, and $c = 3.1 \pm 0.4$ for $\chi^2_\nu = 0.28$. This model has a maximum at $z_{\rm frac} = (b/c) - 1 = 1.3 \pm 0.4$, when accounting for the correlated uncertainties on b and c. In the inset, we show the 68%, 95%, and 99% confidence intervals in the b-c plane for the fit to these data. The peak in the fraction is likely a consequence of the strict mass limit and mass ratio imposed on our sample, and not a result of flux incompleteness (see Figure 9). Our observations can rule out the standard power-law model at $z \gtrsim 1$, which has a reduced $\chi^2_\nu = 7.8$.

While the major merger fraction of massive galaxies may provide excellent information on galaxy evolution, the merger number density is more relevant when comparing to other extragalactic observations. From the merger fraction (f), we compute the merger number density as

$$n_{\rm mg} = \frac{f(z)N(z)}{\int_{z-\Delta z}^{z+\Delta z} dV}, \tag{4.5}$$

where $N(z)$ is the completeness corrected redshift distribution from the Ryan et al. (2007) catalog. Then the merger rate is $\mathcal{R}_{\rm mg} = n_{\rm mg}\tau_{\rm mg}^{-1}$ (P2000). In Figure 15, we show the merger number density for the same data discussed in Figure 14. As a solid line, we show empirical model of Equation (4.4), converted to a number density using the redshift distribution of equation (23) in Benítez (2000). Our merger number density peaks at a $z_{\rm dens} \simeq 1.2$, which is a slightly lower redshift than the peak in the

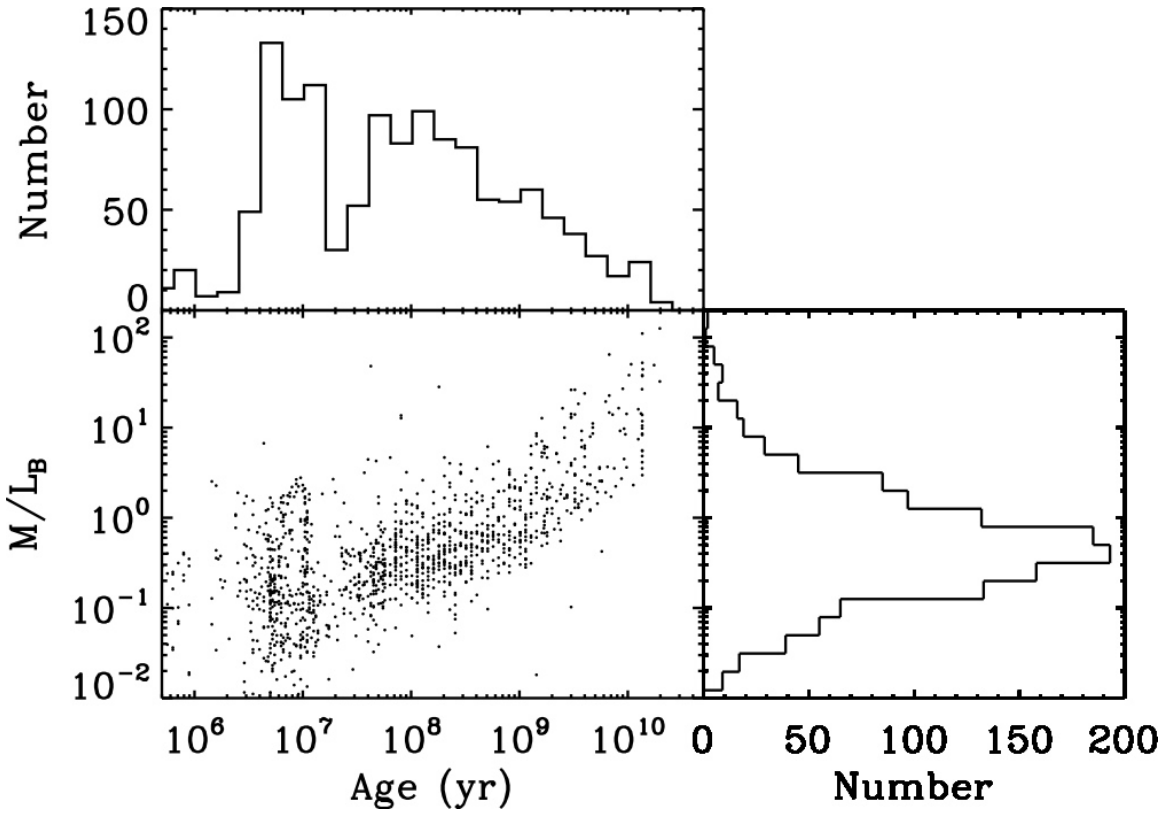

FIG. 13. In the main panel (lower-left), I show the B-band mass-to-light ratios determined from the stellar population synthesis models. Along the vertical and horizontal axes, I show the distribution of mass-to-light ratios and stellar population ages, respectively. The median mass-to-light ratio for these GRAPES galaxies is $\Upsilon_{*,B} \simeq 0.5$ $M_\odot$ $L_\odot^{-1}$, which implies that for a stellar mass of $M_* = 10^{10}$ $M_\odot$ roughly corresponds to an absolute magnitude of $M_B \simeq -20.5$ mag (assuming $M_{B,\odot} = +5.2$ mag). This suggests that the imposed mass limit of $M_* \geq 10^{10}$ $M_\odot$ is consistent with the luminosity limits imposed at $z \lesssim 1$ by various other authors.

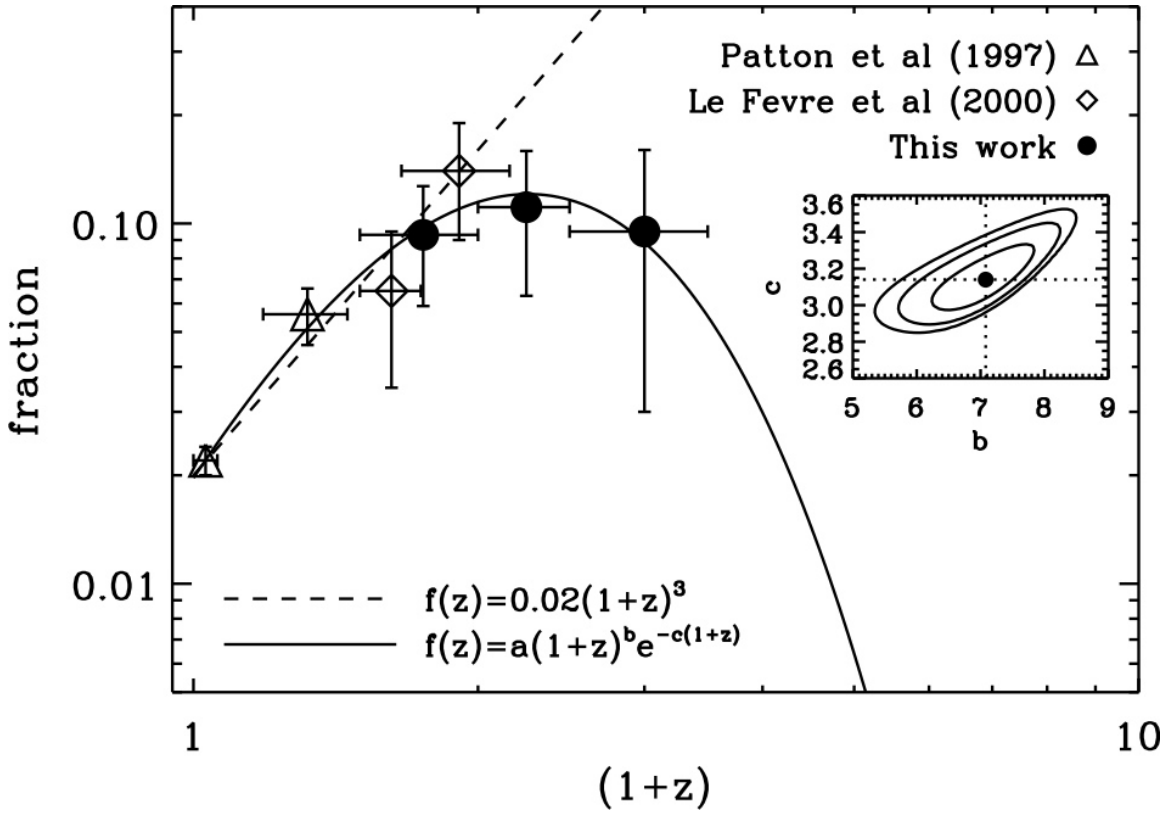

FIG. 14. The results from this work are indicated by filled circles, while the observations of Patton et al. (1997) and Le Fèvre et al. (2000) are shown by open triangles and diamonds, respectively. The dashed line shows the common power-law form of $f(z) = 0.02 \times (1+z)^3$, which fails to fit our high redshift observations. However, the model $f(z) = a(1+z)^b e^{-c(1+z)}$, shown as the solid line, can reproduce all the observations reasonably well ($\chi^2_\nu = 0.28$). This peak in the merger fraction at $z_{\rm frac} \simeq 1.3 \pm 0.4$ may arise from the strict mass limit ($M_* \geq 10^{10}$ M$_\odot$) and mass ratio ($\leq 4{:}1$) imposed on our sample. It is not due to flux incompleteness, given the unparalleled depth of this survey (see Figure 9) and the corrections applied in § 4.3.2. This figure is reproduced from Ryan et al. (2008a).

merger fraction. Finally, we tabulate our measured galaxy major merger fraction and number density in Table 4.

TABLE 4
GALAXY MERGER RESULTS

z	$f(z)$	$n_{\rm mg}{}^{\dagger}$ (10^{-4} Mpc^{-3})
0.75±0.25	0.09±0.03	6.31±2.34
1.25±0.25	0.11±0.04	3.56±1.52
2.00±0.50	0.09±0.06	2.04±1.39

†Computed from the merger fraction by Equation (4.5).

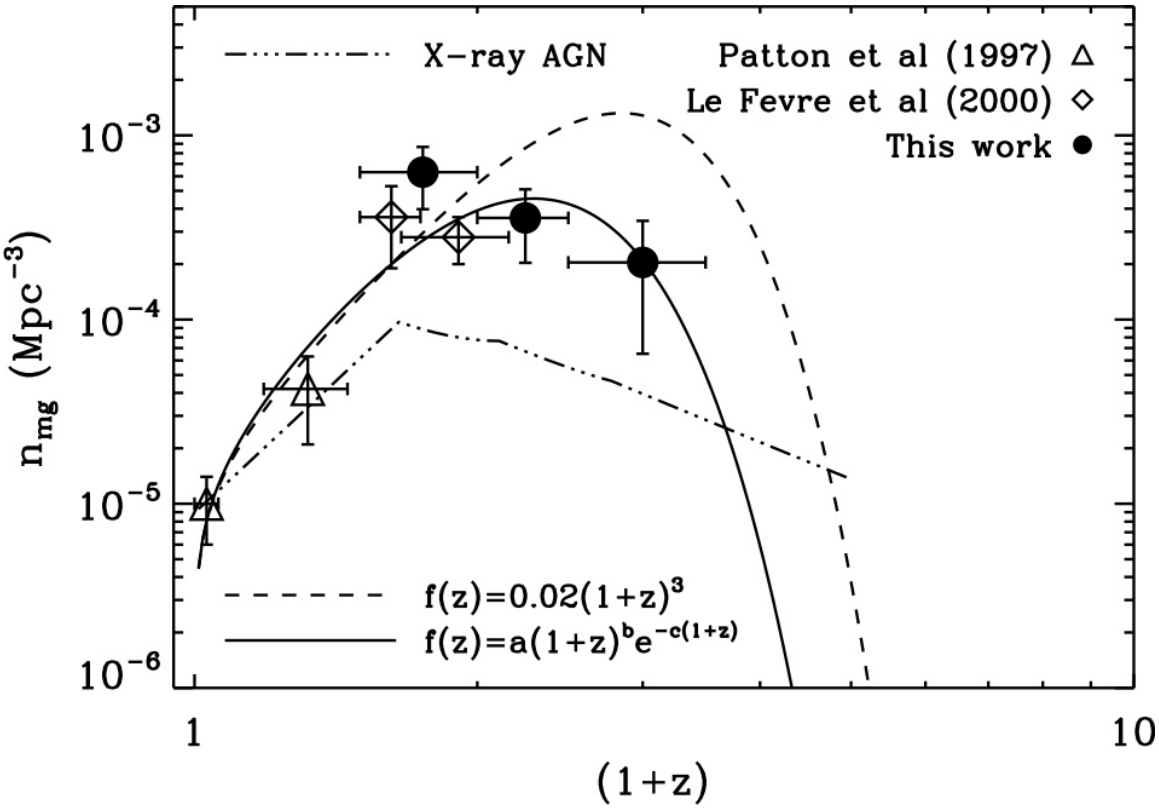

FIG. 15. As in Figure 14, the results from this Chapter are indicated by filled circles, and the observations of Patton et al. (1997) and Le Fèvre et al. (2000) are shown as open triangles and diamonds, respectively. The dotted line shows the total density of AGN with $L_X > 10^{42}$ erg s^{-1} selected in the soft (0.5–2 keV) X-ray band (Hasinger, Miyaji, & Schmidt 2005). The number density of merging galaxies peak at $z_{\rm dens} \simeq 1.2$ while the AGN number density peaks at $z_{\rm AGN} \simeq 0.65$. This difference in redshift corresponds to a cosmic time difference of $\simeq 2.5$ Gyr. A comparable time delay between the merging and the AGN phase has been suggested by simulations (Springel, Di Matteo, & Hernquist 2005a). Moreover, the ratio of the densities at their peaks would suggest that as much as $\sim 20\%$ of the major merging of massive galaxies will evolve into X-ray AGN with $L_X > 10^{42}$ erg s^{-1} (eg. Daddi et al. 2007). This figure is reproduced from Ryan et al. (2008a).

4.5. Comparison to Previous Work

For low to moderate redshifts ($z \lesssim 1$), there have been numerous measurements of the galaxy pair fraction. While many studies disagree on the precise values of the pair fraction, they generally agree that the fraction rises from $\sim 2\%$ at $z \simeq 0$ to $\sim 15\%$ at $z \simeq 1$ following a power-law in $(1+z)$. Where our observations overlap with previous work, we find a merger fraction of $15 \pm 5\%$ at $z \simeq 1$, which is in good agreement with the previously published values (eg. Le Fèvre et al. 2000; Lin et al. 2004; Kartaltepe et al. 2007).

At higher redshift ($z \gtrsim 1$), there are no other studies of merging using the pair fraction, due to the difficulty in acquiring sufficiently deep redshift datasets. However, if the redshift of the primary galaxy can be obtained, then a morphological approach can be a viable method for determining the merger status. Conselice et al. (2003b) has shown a roughly power-law form to $z \simeq 3$ using the CAS (concentration, asymmetry, clumpiness) morphological system (Bershady, Jangren, & Conselice 2000; Conselice 2003a). When these measurements are coupled with restframe colors, the refined merger fraction is substantially higher than our observations (Conselice 2006). However, de Propris et al. (2007) discuss some of the limitations of this system and caution that merger studies using image asymmetry require careful interpretation.

Based on the matched Two Micron All Sky Survey (2MASS)/Two-Degree Field Galaxy Redshift Survey (2dFGRS; Cole et al. 2001), Xu, Sun, & He (2004) identify 38 merging systems with similar close pair criteria at $0.01 \lesssim z \lesssim 0.07$. By adopting a standard stellar mass-to-light ratio in the restframe K_s-band ($\Upsilon_{*,K_s} = 1.32$ $M_\odot$ $L_\odot^{-1}$),

these galaxies are selected to have $M_* \geq 10^{10.25}$ $M_\odot$. While they restricted their work to a smaller range of mass ratios for their systems ($\delta K_s \leq 1$ mag), they find a pair fraction of $1.70 \pm 0.32\%$, consistent with other low values at these low redshifts (eg. Patton et al. 1997).

4.6. Discussion

Using the deepest imaging and spectroscopic data available, we show that the fraction and number density of major mergers between massive galaxies peak at relatively low redshifts ($z \sim 1$). These peaks are likely not an artifact of the data nor the measurement process, given the careful attention to the mass limits, spectro-photometric redshift accuracy, accounting of measurement uncertainties, unprecedented deep flux limit, and the good agreement with published data in the redshift range of overlap.

Since the high redshift portion of our observed major merger rate dramatically differs from the extrapolated results by numerous authors, it is interesting to explore some of the consequences which arise from this difference. In particular, one implication of our merger rate concerns the fraction of galaxies which have undergone a major merger, or the remnant fraction $f_{\rm rem}$. By assuming a merger fraction of $f(z) = 0.011 \times (1+z)^{2.3}$ and a merger timescale $\tau_{\rm mg} = 0.5$ Gyr, Patton et al. (2002) find that $f_{\rm rem} \simeq 15\%$ of galaxies with $-21 \leq M_B \leq -18$ mag have experienced a major merger since $z \simeq 1$. This is in contrast with the semi-analytic models of De Lucia et al. (2006), who argue that $\sim 50\%$ of stars which comprise elliptical galaxies assemble into a single dark halo between $0 \leq z \leq 1$ by major merging. When we apply this

analysis[1] to our slightly larger and steeper merger rate, we find that $f_{\rm rem} \simeq 42\%$ of galaxies with $M_* \geq 10^{10}$ M$_\odot$ have been involved in a major merger since $z=1$, which is consistent with the De Lucia et al. (2006) fractions. Moreover, since our merger rate peaks at some critical redshift, the fraction of massive galaxies that have undergone a major merger tends to a limiting value at $z \rightarrow \infty$ of $f_{\rm rem}^{\rm lim} \simeq 62\%$, whereas a strict power-law form increases to 100%. This suggests that $(1 - f_{\rm rem}^{\rm lim}) \simeq 38\%$ of massive galaxies may have never undergone a major merger in their lifetime, but does not preclude a series of minor mergers or steady infall.

The magnitude of physical processes, which are driven by galaxy merging, should be proportional to the merging galaxy number density. Many phenomena have been linked to galaxy merging, most notably, star formation, AGN activity, and galaxy morphologies. The cosmic star formation rate density, as traced by radio, ultraviolet, far infrared, and/or various emission line luminosities has been measured by numerous authors at $z \lesssim 7$ (Lilly et al. 1996; Madau et al. 1996; Connolly et al. 1997; Steidel et al. 1999; Haarsma et al. 2000; Brinchmann et al. 2004; Wyder et al. 2005; Bouwens et al. 2006; Hopkins & Beacom 2006). While there is reasonable consensus that the star-formation rate density increases from $z \simeq 0$ to $z \simeq 1$, the high redshift portion can differ greatly among the many authors. Nonetheless, the peak in our merger number density is consistent with the peak in the cosmic star-formation rate density at $z \simeq 1-1.5$. Moreover, the peak star-formation rate density is $\sim 10^{-1}$ M$_\odot$ yr^{-1} Mpc^{-3} (eg. Hopkins & Beacom 2006), which would require the typical merger system to have a star-formation rate of ~ 100 M$_\odot$ yr^{-1}. This rate

[1]Our remnant fraction is found from equation (18) of Patton et al. (2002).

is considerably higher than what is expected for major mergers (Bell et al. 2005), which suggests that major mergers are not the only source of star-formation at these redshifts. However, minor merging is expected to be more frequent, and may be responsible for triggering the remaining portion of the cosmic star-formation density.

Many authors have addressed an evolutionary link between merging galaxies and AGN (Carlberg 1990a; Silk & Rees 1998; Kauffmann & Haehnelt 2000; Croton et al. 2006; Hopkins et al. 2006), and generally agree that major merging can drive AGN activity. Therefore, it is natural to compare our merger number density to the observed AGN density. The density of type-1 AGN selected in soft (0.5–2.0 keV) X-ray band with luminosities of $L_X = 10^{42} - 10^{46}$ erg s^{-1} from Hasinger, Miyaji, & Schmidt (2005) is shown in Figure 15 as a dotted line. This sample traces the roughly instantaneous AGN activity unobscured through any dust, and is similar to the results in the hard X-rays (Ueda et al. 2003). This AGN density peaks at $z_{\rm AGN} \simeq 0.65$, or a lookback time of $\simeq$5.9 Gyr, whereas our observed merger number density peaks at $z_{\rm dens} \simeq 1.2$, or $\simeq$8.5 Gyr in lookback time. If a major merger of two galaxies triggers an AGN, then we may expect on average ~ 2.6 Gyr between the time when the galaxies are observed as a pair on the sky, and when the remnant would be observed as an AGN in the soft X-rays. Springel, Di Matteo, & Hernquist (2005a) have suggested that major merging can trigger the fueling of the central black hole *after* the merger onset, and will be observed as a visible AGN $\sim$1$-$2 Gyr later. According to these simulations, we expect the merger number density to peak $\sim$2.5 Gyr earlier

in cosmic time than the AGN density, which is similar to our observations to within the uncertainties.

These measurements have exploited the excellent redshift accuracy, spatial resolution, and depth of ACS grism observations. The Wide Field Camera 3 for HST will provide combined ultraviolet prism, infrared grism, and numerous ultraviolet, optical, and near-infrared broadband observations. With such a rich dataset, redshifts of comparable accuracy from $2 \lesssim z \lesssim 6$ should become standard. This will be ideal for refining this work, and determining the role of various effects, such as galaxy environments and/or cosmic variance at $z \lesssim 6$.

CHAPTER 5

The Galaxy Major Merger Rate from BVi'-band Dropouts

5.1. Introduction

In the hierarchical formation paradigm, galaxies are expected to evolve by repeated mergers and interactions (eg. Kauffmann, White, & Guiderdoni 1993) with episodes of merger-driven star formation (eg. Larson & Tinsley 1978). When these ideas are extended to include the feedback of an active galactic nucleus (AGN; eg. Silk & Rees 1998), they begin to provide a self-consistent framework for understanding galaxy evolution. Recent computer simulations have suggested that as galaxies merge, they will trigger a modest starburst in the constituent systems, which often continues for $\sim 1 - 2$ Gyr until the central black hole triggers an AGN (Springel, Di Matteo, & Hernquist 2005a). By suppressing the present star formation, the feedback from the AGN may be responsible for formation of the red sequence of elliptical galaxies (Springel, Di Matteo, & Hernquist 2005b) and may lead to galaxy downsizing (Scannapieco, Silk, & Bouwens 2005). This formation scenario indicates that galaxies grow via a "duty cycle" of merging, starbursts, and AGN (Hopkins et al. 2006). While these ideas are quickly maturing, there remain many open observational questions. In particular, the precise form of the galaxy merger rate will be a unique constraint, since it serves as the central and driving mechanism in this formation model.

The duty cycle of merging, starburst, and AGN suggests that we may observe correlations between the galaxy merger rate, galaxy mass assembly (eg. Dickinson et al. 2003), the cosmic star formation rate density (eg. Madau et al. 1996; Hopkins & Beacom 2006), and the epoch-dependent AGN space density (eg. Ueda et al. 2003; Hasinger, Miyaji, & Schmidt 2005). However, there may be an additional class of

secondary phenomena, which may also be related galaxy merging. The observed galaxy luminosity function evolves over cosmic time, particularly the faint-end slope, where there are significantly more dwarf galaxies at high redshift (eg. Bouwens et al. 2007; Ryan et al. 2007). This evolution can be quantitatively and qualitatively understood from a merger-based semi-analytic model, where the evolution of the dark halo mass function dictates the evolution of the galaxy luminosity function (Khochfar et al. 2007). Observed at cosmological distances, gamma-ray bursts (GRBs) are likely the supernovae of very massive stars ($M \gtrsim 40$ M$_\odot$; Stanek et al. 2003; Mazzali et al. 2006), which must have formed in a recent starburst. Whether this starburst was initiated by a galaxy merger or in some other way reflects the increased cosmic star formation rate, the rise in the GRB rate at low redshift (eg. Kistler et al. 2008) or a possible peak in the GRB fraction at $z \simeq 1.4$ (eg. Young & Fryer 2007) may be caused by the redshift evolution of the galaxy merger number density.

Finally, the aggregation of stellar mass as implemented by galaxy merging may also be responsible for the decrease in galaxy sizes with redshift. Several authors have found that the half-light radii of galaxies are roughly proportional to $H(z)^{-\gamma}$ (eg. Ferguson et al. 2004; Trujillo et al. 2006; Hathi, Malhotra, & Rhoads 2008b), where $\gamma = 2/3$ for a fixed galaxy mass and $\gamma = 1$ for a fixed circular velocity (eg. Mo, Mao, & White 1999). The majority of observations generally favor the fixed circular velocity model with $\gamma \simeq 1$, which supports the hierarchical clustering model of disk galaxy formation (eg. Fall & Efstathiou 1980). While many of these phenomena have been well studied by various techniques for $z \lesssim 6$ (particularly the mass assembly,

cosmic star formation rate, and AGN density), there has been little observational work on merging galaxies at comparable redshifts. In Ryan et al. (2008a, Chapter 4), we presented some of the highest redshift measurements of the galaxy major merger fraction and number density for $0.5 \leq z \leq 2.5$. The density of major mergers between massive galaxies increases from $z \simeq 0$ to $z \simeq 1.3$, and appears to decline at higher redshifts. While this behavior is qualitatively similar to the cosmic star formation rate and the AGN number density, higher redshift ($z \gtrsim 3$) observations of major mergers are needed to further explore and confirm this possible trend.

At low redshift ($z \lesssim 1$), the galaxy merger rate is derived from the merger fraction, which is often parameterized as proportional to $(1+z)^m$, where $1 \lesssim m \lesssim 4$ (Zepf & Koo 1989; Burkey et al. 1994; Carlberg, Pritchet, & Infante 1994; Yee & Ellingson 1995; Neuschaefer et al. 1997; Patton et al. 1997; Le Fèvre et al. 2000; Patton et al. 2002; Lin et al. 2004; Xu, Sun, & He 2004; Bell et al. 2006; Kartaltepe et al. 2007; Hsieh et al. 2008). However, there are indications that the strict power-law form may fail at higher redshift (Conselice, Rajgor, & Myers 2008; Ryan et al. 2008a), and that the major merger fraction is more suitably fit by the empirical form proposed by Conselice (2006): $f(z) = a(1+z)^b e^{-c(1+z)}$, with $a = 0.44 \pm 0.04$, $b = 7.0 \pm 0.6$, and $c = 3.1 \pm 0.4$ (Ryan et al. 2008a). Our intermediate redshift observations ($0.5 \leq z \leq 2.5$) suggest a possible peak in the major merger rate at $z_{\rm max}^{\rm frac} = (b/c) - 1 = 1.3 \pm 0.4$.

Current theories and numerical simulations have made galaxy mergers the central theme of galaxy formation and evolution. Moreover there are several indications that the galaxy merger rate may be sensitive to the cosmological parameters. Carl-

berg (1990b) suggest that the galaxy merger rate may be sensitive to the matter density (Ω_0), and later argue that the power-law index (m) of the redshift-dependent merger rate strongly depends on the matter and dark energy densities (Ω_Λ; Carlberg 1991). Governato et al. (1999) find that $m = 2.5 \pm 0.4$ and $m = 3.1 \pm 0.2$ for open ($\Omega_0 = 0.3,\ h = 0.75,$ and $\sigma_8 = 1$) and tilted ($\Omega_0 = 1,\ h = 0.5,$ and $\sigma_8 = 0.6$) cosmology, respectively. With a semi-analytic model of galaxy formation, Khochfar & Burkert (2001) investigate the effect of the equation of state parameter for the dark energy (w) on the galaxy merger rate. By comparing to the available observations, they find that the galaxy merger fraction does not strongly depend on the adopted cosmology, namely quintessence ($w = -2/3$) versus Λ ($w = -1$) cold dark matter (CDM) models. The precise role of galaxy mergers in constraining the cosmological model may become clearer as more observations, both at higher redshifts and varied mass/luminosity limits, become available. In this Chapter, we will extend our previous results at $0.5 \leq z \leq 2.5$ to higher redshifts ($z \gtrsim 3$), using observations of Lyman break galaxies (LBGs; eg. Steidel et al. 1996) selected as BVi'-band dropouts.

This Chapter is organized as follows: § 5.2 describes the datasets, § 5.3 outlines our merging galaxy sample with corrections for the redshift reliability, § 5.4 discusses the redshift evolution of the galaxy merger rate, and § 5.5 is a general discussion of these results in the context of galaxy formation. We quote all magnitudes in the AB system (Oke & Gunn 1983). For the cosmological model, we adopt $\Omega_0 = 0.24$, $\Omega_\Lambda = 0.76$, and $H_0 = 100\ h$ km s^{-1} Mpc^{-1} where $h = 0.73$ (Spergel et al. 2007).

5.2. Data

To identify and study galaxy pairs at high redshift ($z \gtrsim 3$), we require deep high-resolution imaging in a variety of bandpasses. Therefore, only the deep fields observed by the Hubble Space Telescope (HST) will suffice, in particular those observed with the Advanced Camera for Surveys (ACS) in the $BVi'z'$-bands. Such observations have proven quite successful at identifying high redshift galaxies using the dropout selection (Giavalisco et al. 2004b; Yan & Windhorst 2004b; Bouwens et al. 2006; Beckwith et al. 2006; Hathi, Malhotra, & Rhoads 2008b). Therefore, we will adopt a similar color–color selection for three multiwavelength, deep fields observed by HST. The Great Observatories Origins Deep Survey (GOODS) consists of two 3×5 ACS pointings, one in the north and one in the south, covering a total of 316 arcmin^2 (Giavalisco et al. 2004a). We use the GOODS v2.0 imaging and catalogs, which are generally ~ 0.3 mag deeper than the v1.0 dataset. The Hubble Ultra-Deep Field (HUDF) is a single ACS pointing ($3\farcm3 \times 3\farcm3$) of 400 orbits (Beckwith et al. 2006), located in the GOODS-S field and is an additional ~ 2.5 mag deeper than either GOODS field. In Figure 1, I show the approximate field geometry and layout for the GOODS and HUDF surveys.

To identify our high redshift LBGs from the deep ACS imaging, we use the software package `SExtractor` (Bertin & Arnouts 1996), and adopt the GOODS extraction parameters (Giavalisco et al. 2004a). We require that each object has at least 16 connected pixels that are 0.6σ brighter than the local sky. For object deblending, we use 32 sub-thresholds with a minimum contrast of 0.03. These parameters facil-

itate identifying point source objects, which is ideal for these compact LBGs. From these catalogs, we determine the approximate 50% completeness limit in flux for each field and bandpass, based on a power-law fit to the observed number counts. To select the high redshift LBGs, we adopt the color-color selection described by Bouwens et al. (2007), with additional constraints on the signal-to-noise (S/N) in the bands immediately blueward and redward of the Lyman discontinuity: $(S/N)_{\rm blue} \leq 2$ and $(S/N)_{\rm red} \geq 5$, respectively (eg. Giavalisco et al. 2004b). In Figure 16, Figure 17, and Figure 18, I show the color-color selections for the BVi'-band dropouts, respectively. I summarize our dropout samples by giving the limiting magnitudes and the object counts in Table 5.

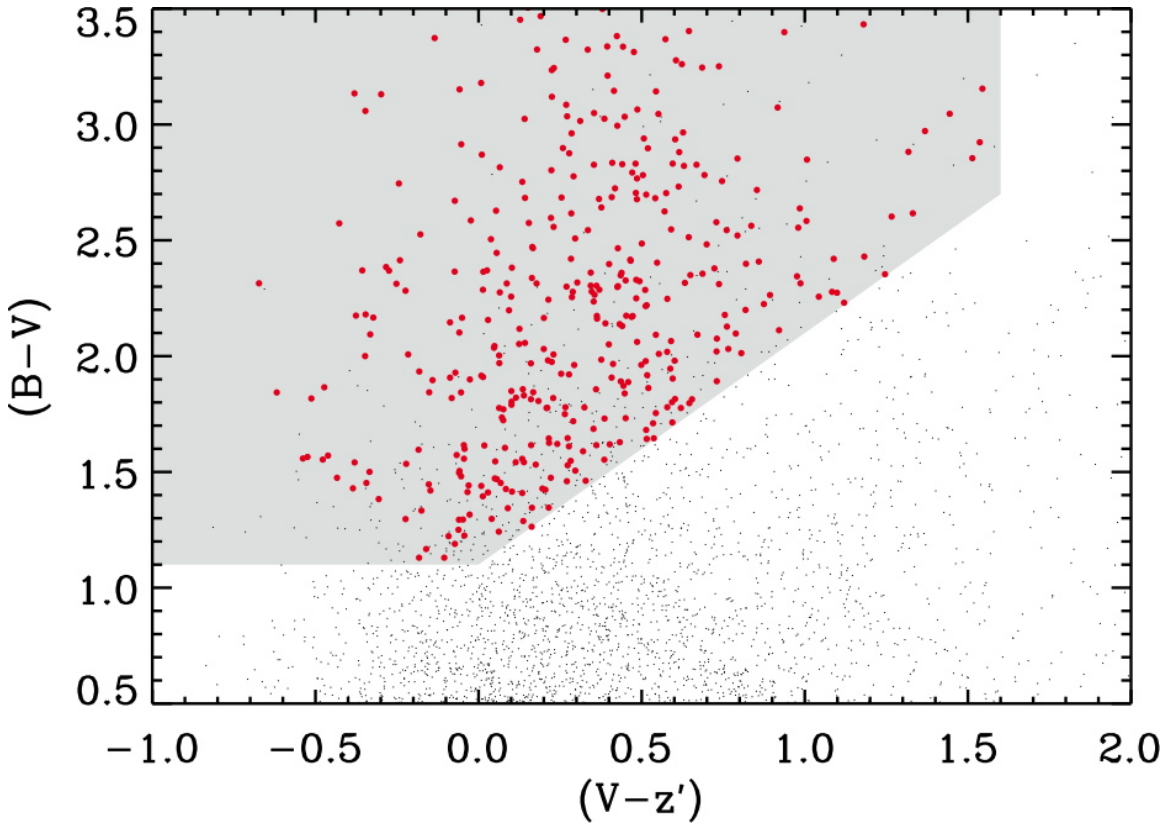

FIG. 16. Each dot represents a single galaxy identified in the HUDF, while the red points indicate galaxies which satisfy the LBG color criteria of $(B-V)>1.1$ and $(B-V)>1.1+(V-z')$ and $(V-z')<1.6$ mag. By imposing signal-to-noise limits on the bands blueward $(S/N)_{\rm blue}<2$ and redward $(S/N)_{\rm red}>5$ of the Lyman limit ($\lambda_{\rm rest}=912$ Å), these dropout selection rules can reliably identify galaxies at $z\simeq 3.8\pm 0.3$.

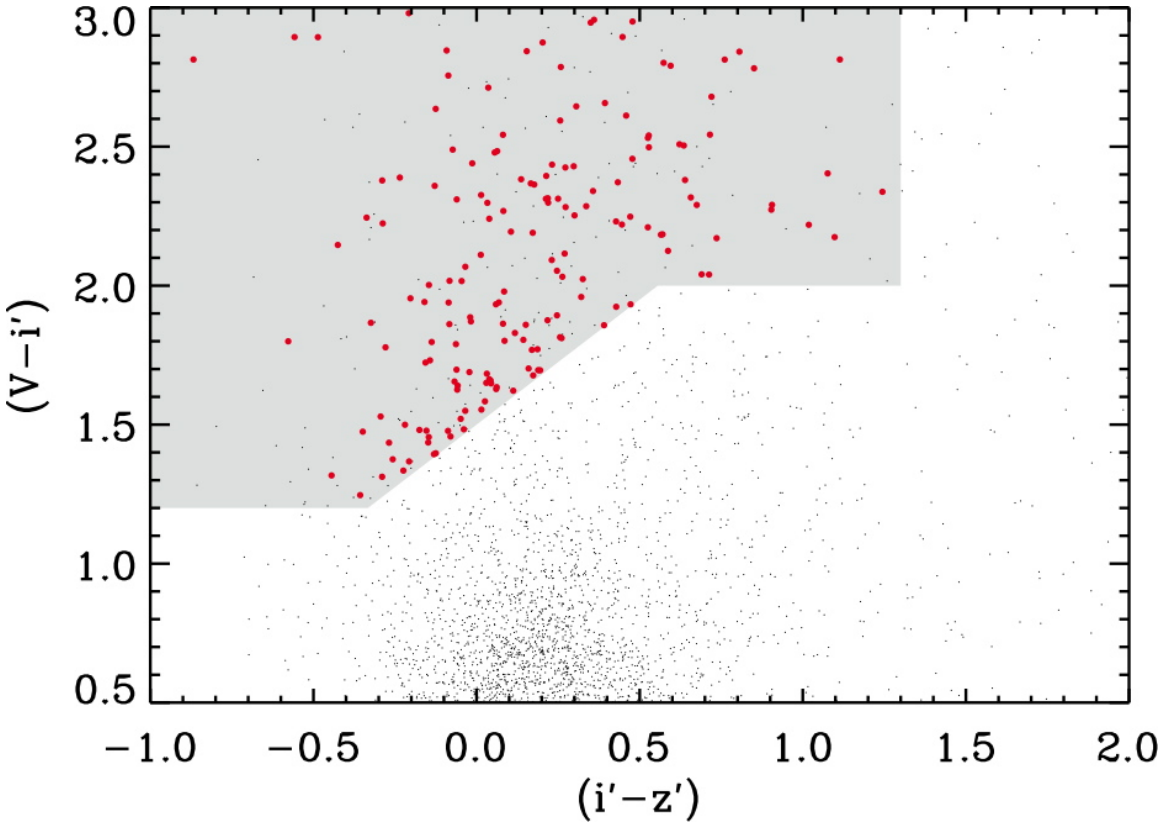

FIG. 17. As in Figure 16, the black symbols represent each galaxy in the HUDF, while the red symbols show the galaxies satisfying the V-band dropout selection of $((V-i')>1.5+0.9(i'-z')$ or $(V-i')>2)$ and $(V-i')\geq 1.2$ and $(i'-z')\leq 1.3$ mag. By imposing similar signal-to-noise limits as for the B-band dropouts, these color–color criteria select galaxies at $z\simeq 5.0\pm 0.4$ from the Lyman forest ($\lambda_{\rm rest}<1216$ Å). Unlike the B-band dropouts, this selection is subject to contamination of low redshift elliptical galaxies whose 4000 Å break masquerades as the Lyman break. Vanzella et al. (2006) estimate that the reliability of the V-band dropout selection is $\gtrsim$90% (see § 5.3.2 for additional discussion).

TABLE 5
DROPOUT SAMPLES

Dropout	Limit† (mag)	$N_{\rm LBGs}$
	GOODS-N‡	
B	$V \leq 27.9$	1602
V	$i' \leq 27.7$	579
i'	$z' \leq 27.6$	256
	GOODS-S‡	
B	$V \leq 27.7$	1407
V	$i' \leq 27.5$	412
i'	$z' \leq 27.4$	230
	HUDF	
B	$V \leq 29.8$	700
V	$i' \leq 29.7$	229
i'	$z' \leq 29.8$	73

†The 50% completeness limit derived from a power-law fit to the observed galaxy counts.

‡We used the GOODS v2.0 imaging and catalogs (http://archive.stsci.edu/pub/hlsp/goods/).

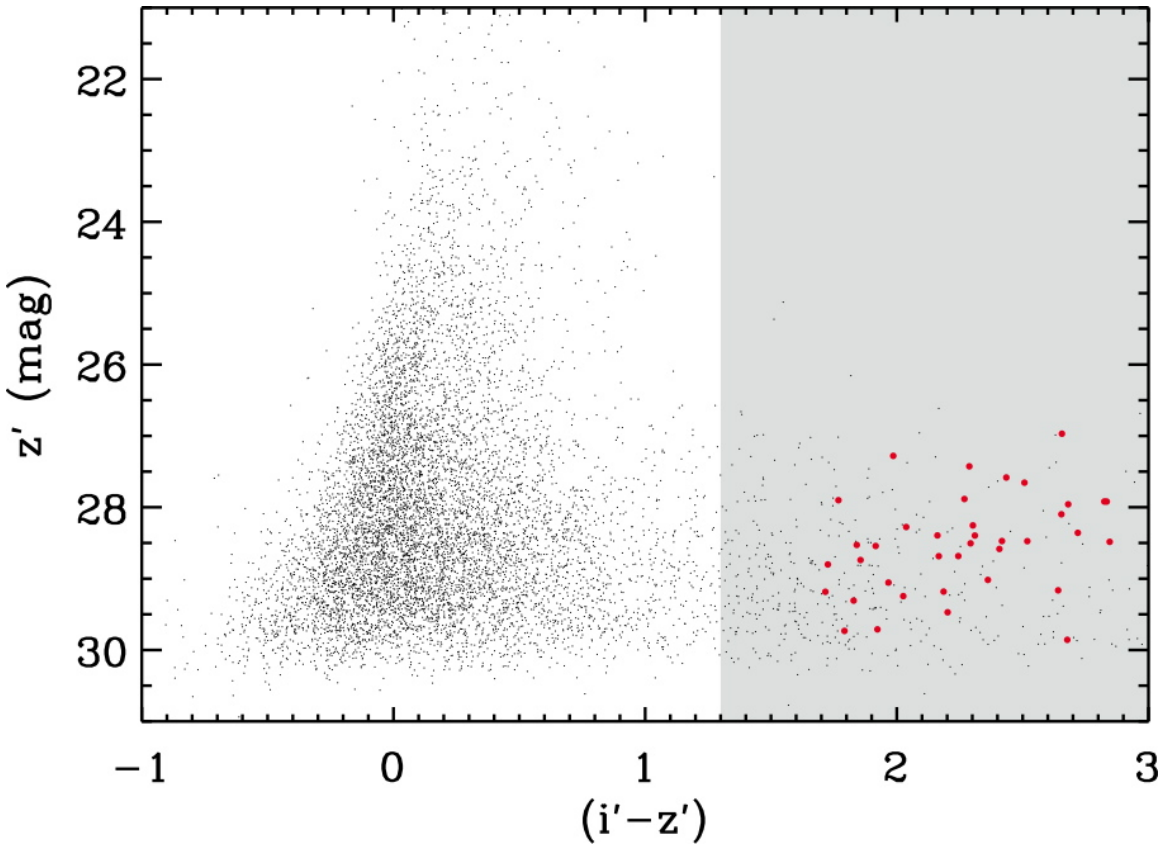

FIG. 18. Like the previous two figures (Figure 16 and Figure 17), I show each galaxy from the HUDF as a solid black circle and those galaxies selected from as i'-band drops from $(i' - z') \geq 1.3$ mag. Since the overwhelming majority of the galaxies in this study do not have deep, high resolution J-band imaging, I cannot impose an additional color criterion of $(z' - J) \lesssim 1.3$ mag, which is similar to the V-band dropout selection. Without this additional $(z' - J)$ color constraint, this i'-band dropout selection will systematically identify low mass, Galactic stars. In § 5.3.2, I statistically correct the merger counts for a L- & T-dwarf contribution, based on the estimate of the scale height of this population (Ryan et al. 2005, and Chapter 6).

5.3. Analysis

5.3.1. *Merger Selection*

There have been a number of techniques developed to identify and measure various properties of galaxies in all states of merging. A popular approach has been to measure a series of morphological indicators, which are assumed to have been triggered by the recent merger (eg. Conselice et al. 2003b; Straughn et al. 2006; Lotz et al. 2008). While these schemes differ in their execution, they are all critically dependent on the angular resolution of the survey, and the source deblending algorithms (eg. de Propris et al. 2007). While HST imaging provides the best possible resolution on faint galaxies (Windhorst et al. 2008), a morphological approach at $z \gtrsim 3$ will be met with two major challenges:

(1) At these redshifts, the majority of galaxies are observed to have half-light radii of $r_{hl} \lesssim 0\farcs3$ (Ferguson et al. 2004; Bouwens et al. 2006; Hathi, Malhotra, & Rhoads 2008b) or $r_{hl} \lesssim 10$ pixels. Overzier et al. (2008) find that the UV-luminous galaxies (UVLGs) identified with GALEX (Heckman et al. 2005) resemble high-redshift LBGs at $z \gtrsim 4$. They conclude that these galaxies often show qualitative merger signatures (such as double nuclei, tidal tails, companions). However, many of these features would be unresolved and/or too faint to be identified in the HST imaging of galaxies at $z \gtrsim 3$ (eg. Cohen et al. 2003).

(2) Since the morphological approach requires a calibration dataset, the rest-frame wavelength in which the galaxies are observed becomes critical. The optical/near-infrared imaging ($Vi'z'$-bands) with HST-ACS samples the far-ultraviolet ($\lambda_{\rm rest} \sim$

1300 Å) continuum and/or possible Lyα line emission in the restframe of the dropout galaxies. However, most morphological indicators are calibrated with surveys conducted in the restframe optical (eg. Frei et al. 1996). Therefore, the blind use of these indicators, without additional calibration for the UV restframe wavelength sampled, may lead to erroneous conclusions owing to possible wavelength-dependent galaxy morphologies (eg. Teplitz et al. 1998; Windhorst et al. 2002; Papovich et al. 2003; Cassata et al. 2005; Taylor-Mager et al. 2007).

Given these possible limitations of a morphological approach, we adopt the "dynamically-close pair" method (eg. Carlberg, Pritchet, & Infante 1994), which is a slight modification of the traditional pair count (eg. Zepf & Koo 1989) by including redshift measurements for *both* the primary and companion galaxy. While the Lyman break technique can select galaxies at a given redshift, the uncertainty on this redshift can be $\sigma_z \sim 0.3$, which gives an unacceptably large uncertainty on the proper distance. Therefore, our technique should be considered as a compromise between the dynamically-close pairs, where the velocity difference between the primary and companion galaxies can be measured and considered, and the projected pair count, which does not include redshift measurements in any way. We will address and account for the redshift uncertainties after defining our merger samples in § 5.3.3.

To construct our merger catalogs, we begin with the standard definition for close galaxy pairs: (1) The separation of the pairs should be sufficiently small to ensure that the pairs will merge in the typical merger timescale of $\tau_{\rm mg} \lesssim 1$ Gyr. For this projected distance, we adopt $\Delta r \leq 20\,h^{-1}$ kpc; (2) The luminosity ratio of the primary-

to-companion galaxies should be $\Delta M_B \leq 1.5$ mag. If we assume the two galaxies have the same intrinsic mass-to-light ratio, then this luminosity ratio selects major mergers with a mass ratio of approximately $\leq 4:1$; (3) The merging pair should have the same redshift to within their 1σ uncertainties, which will be discussed in more detail below. As noted above, this redshift requirement is the primary difference between the two aforementioned pair count methods; (4) The final criterion that is generally adopted concerns the luminosity of the primary galaxy. The varying flux limits of these fields and the luminosity dependence on redshift complicates a straightforward luminosity threshold. Therefore, we adopt the techniques developed by Patton et al. (2000) to consistently identify dynamically-close galaxy pairs, while simultaneously correcting a flux-limited survey to the comparable volume-limited survey. In this method, one constructs two optimal parameters, which measure the merger rate and the mass accretion rate. We will briefly outline the Patton et al. (2000) algorithm:

From the inherently flux-limited surveys, we desire all galaxy pairs that have a primary galaxy in a given absolute magnitude range: $M_{br} \leq M_B \leq M_{fa}$. To select such systems, Patton et al. (2000) determine a redshift-dependent absolute magnitude limit:

$$M_{\rm lim}(z) = \min\left[M_{fa} + \Delta M_B, m_{\rm lim} - 5\log d_L(z) - 25 - k^{\rm max}_{m\rightarrow B}(z) - E(z)\right], \qquad (5.1)$$

where $m_{\rm lim}$ represents the magnitude limit from the band immediately redward of the Lyman break (see Table 5), $d_L(z)$ is the luminosity distance in megaparsecs, $k^{\rm max}_{m\rightarrow B}(z)$ is the maximum k-correction from the observed band immediately redward of the Lyman discontinuity to the restframe B-band, and $E(z)$ is the luminosity evolutionary

correction. Patton et al. (2002) determine the maximum k-correction from the R_C-to the B-band at $0.12 \leq z \leq 0.55$ for the empirical galaxy templates of Coleman, Wu, & Weedman (1980). These templates may not be generally applicable to the high redshift LBGs, instead we adopt the population synthesis models of Bruzual & Charlot (2003), which have been successful in fitting the broadband observations of LBGs at $z \sim 3$ (eg. Papovich, Dickinson, & Ferguson 2001). While there are some variations in the stellar populations, these LBGs generally have relatively low dust content ($A_V \lesssim 1.2$ mag) and young stellar populations ($t \sim 200$ Myr) with exponential star formation histories ($\Psi(t) \propto e^{-t/\tau}$, where $\tau \lesssim 2$ Gyr). Therefore, we use the k-corrections derived from these average stellar populations, which are $k^{\rm ave}_{m \rightarrow B}(z) \sim -2$ mag. The luminosity evolution correction can be parameterized as $E(z) = Qz$, where $Q \simeq 1$ for $z \lesssim 1$ (eg. Lin et al. 1999; Patton et al. 2002). However the characteristic galaxy luminosity *decreases* for $z \gtrsim 1$ (eg. Bouwens et al. 2007), which would argue perhaps for $Q \sim -0.5$. Given the lack of any quantification of Q at the redshifts which are of interest here ($z \gtrsim 3$), we will adopt no evolutionary correct (ie. $Q = 0$). We did investigate $Q = -0.5$, and find that our merger statistics slightly increase by a factor of $\lesssim 2$ at $z \simeq 3.8$ and a factor of $\lesssim 3$ at $z \simeq 5.9$. As will be shown below, this factor will not affect our conclusion nor could it account for the overall significant decline in the major merger fraction at $z \gtrsim 3$.

We can now identify the sample of primary galaxies which satisfy the above four criteria. However, the flux-limited surveys will systematically miss companions fainter than the completeness limits. Patton et al. (2000) demonstrate that, with an

assumed galaxy luminosity function (LF), one can correct the pair counts for these missing companions. For the BVi'-band dropouts, we adopt the LFs determined by Bouwens et al. (2007), and give their Schechter function parameters in Table 6 (Schechter 1976). The selection functions for the pair fraction and luminosity in the companion galaxies are defined as:

$$S_N(z) = \frac{\int_{M_{br}-E(z)}^{M_{\rm lim}(z)-E(z)} \Phi(M,z)dM}{\int_{M_{br}-E(z)}^{M_{fa}-E(z)} \Phi(M,z)dM}, \tag{5.2}$$

$$S_L(z) = \frac{\int_{M_{br}-E(z)}^{M_{\rm lim}(z)-E(z)} \Phi(M,z)L(M)dM}{\int_{M_{br}-E(z)}^{M_{fa}-E(z)} \Phi(M,z)L(M)dM}, \tag{5.3}$$

respectively. We numerically evaluate these integrals, and generate our effectively volume-limited sample for $M_{fa} = -20.5$ mag and $M_{br} = -25.0$ mag, which are chosen match lower redshift analyses.

TABLE 6
PROPERTIES OF DROPOUT GALAXIES†

Dropout	z	M^* (mag)	α
B	3.8 ± 0.3	-21.06 ± 0.10	-1.76 ± 0.05
V	5.0 ± 0.4	-20.69 ± 0.13	-1.69 ± 0.09
i'	5.9 ± 0.3	-20.29 ± 0.19	-1.77 ± 0.16

†All values are taken from Bouwens et al. (2007), and are tabulated here for completeness.

The primary and companion galaxies are individually weighted as a function of their brightnesses using these selection functions. The optimal weights for this procedure must take into account a variety of selection biases. First, we consider the boundary effects. Following Patton et al. (2002), a primary galaxy near a field edge of the survey must be given a lower weight, which we will take to be the ratio of the effective surveyed area to the circular area, as defined by the search radius (Δr) and close-pair condition. Therefore, a primary galaxy that is a distance Δb from an assumed survey border will be assigned the weight

$$w_b = \begin{cases} \frac{1}{\pi}\left[\left(\frac{\Delta b}{\Delta r}\right)\sqrt{1-\left(\frac{\Delta b}{\Delta r}\right)^2} - \cos^{-1}\left(\frac{\Delta b}{\Delta r}\right)\right] + 1;\ \Delta b \leq \Delta r \\ 1;\ \Delta b > \Delta r. \end{cases} \tag{5.4}$$

In general, this weight will contribute very little, since ratio of selection area to the total survey area is $\sim 7.5 \times 10^{-5}$ and $\sim 1.1 \times 10^{-3}$ at $z = 3.8$ for the GOODS fields and the HUDF, respectively. Finally, the optimal weights for the primary galaxies for the number fraction and the luminosity of the close pairs will be:

$$w_{N,1}(z_i) = S_N(z_i) w_b, \tag{5.5}$$

$$w_{L,1}(z_i) = S_L(z_i) w_b. \tag{5.6}$$

Similarly, the optimal weights for the companion galaxies will be:

$$w_{N,2}(z_i) = \frac{1}{S_N(z_i) w_b}, \tag{5.7}$$

$$w_{L,2}(z_i) = \frac{1}{S_L(z_i) w_b}. \tag{5.8}$$

We will discuss additional weights which account for the redshift reliability of the LBG sample in § 5.3.2. The pair statistics (N_c and L_c) are found from summations over

these optimal weights. For the ith primary galaxy, we compute $N_{c,i} = \sum_j w_{N,2}(z_j)$ and $L_{c,i} = \sum_j w_{L,2}(z_j) L_j$, where each summation runs over all companion galaxies which satisfy the above four merger criteria. Then the optimally weighted pair statistics are found from weighted averages of $N_{c,i}$ and $L_{c,i}$:

$$N_c = \frac{\sum_i w_{N,1}(z_i) N_{c,i}}{\sum_i w_{N,1}(z_i)}, \tag{5.9}$$

$$L_c = \frac{\sum_i w_{L,1}(z_i) L_{c,i}}{\sum_i w_{L,1}(z_i)}, \tag{5.10}$$

where these summations run over all the primary galaxies in the LBG catalogs. For a strictly volume-limited survey with no borders and in which all merger systems are binary pairs, N_c is identical to the galaxy pair fraction. Since all surveys will have edge-effects and a distribution in the number of close companions, N_c and L_c are only directly proportional to the galaxy merger rate and the mass accretion rate (Patton et al. 2000, 2002). For the merger rate, the constant of proportionality is 0.5 for binary mergers and decreases correspondingly for higher order n-tuples. The mass accretion rate also requires the mass-to-light ratio as an additional conversion factor (Patton et al. 2000).

5.3.2. *Sources of Contamination*

While the dropout selection can be very effective at identifying high redshift LBGs galaxies, it will can systematically select other astronomical objects (eg. foreground elliptical galaxies or late-type Galactic stars; Yan, Windhorst, & Cohen 2003). Therefore, it is critical to spectroscopically confirm each putative LBG, to ensure a reliable sample of high redshift galaxies. For the typical numbers and brightnesses of LBGs, this can be a daunting task, even for 10 m class telescopes with multislit

capabilities. Therefore, we can only attempt to correct our merger counts in a statistical fashion. From deep observations with the VLT in the GOODS-S field, Vanzella et al. (2006) determine that 100%, 90%, and 93% of the BVi'-band dropouts are indeed high redshift LBGs, respectively. In most cases, the interloping objects are lower redshift galaxies, where the Balmer/4000 Å break is misidentified as the Lyman break.

Like foreground elliptical galaxies, late-type Galactic stars can be mistakingly identified as high redshift LBGs. While infrared observations ($\lambda_{\rm obs} \gtrsim 1.0$ μm) can break this identification degeneracy, they are generally not available at our deep flux limits. Therefore without deep spectroscopy to verify the the object identification and redshift, we must again resort to a statistical correction. The most dominate source of Galactic stars comes from M-, L-, and T-dwarfs (eg. Caballero, Burgasser, & Klement 2008). Since the scale height for the population of Galactic L- and T-dwarfs is $z_l \simeq 350$ pc, we expect that 97% of the i'-band dropouts are LBGs for $z' \lesssim 29$ mag and not foreground Galactic stars (Ryan et al. 2005, and Chapter 6 here).

We adopt these published estimates for the reliability of the BVi'-band dropout samples as additional factors in defining the optimal weights for the primary (equation 5.5) and secondary galaxies (equation 5.7). These corrections are then 1.0, 0.9, and 0.9 ($=0.93 \times 0.97$ for the foreground ellipticals and late-type Galactic stars) for the BVi'-band dropouts, respectively.

5.3.3. *Error Budget*

As mentioned above, the redshift uncertainty for the LBGs can be $\sigma_z \sim 0.3$, which gives a typical uncertainty on the proper distance of $\sigma_{d_p} \sim 200$ Mpc at redshifts of interest. Therefore, we perform a simple Monte Carlo simulation, where the redshift of a given galaxy is drawn from a normal distribution with a mean and standard deviation given in Table 6 (column 2). With this procedure, we can empirically determine the uncertainties on the merger counts and their luminosities, which include the effects of Poisson noise and chance superpositions, while preserving the spatial imprint of any clustering or large-scale structures. In Figure 19 and Figure 20, we show the results of 10^3 Monte Carlo realizations for the BVi'-dropouts in the GOODS-N, GOODS-S, and HUDF fields for the merger fraction (N_c) and the fraction of luminosity in merging components (L_c). We show a Gaussian fit to each distribution as a solid red line. Owing to the lower number counts, the distributions derived from the HUDF are poorly sampled and yield merger statistics with larger uncertainties.

The effects of cosmic variance can be easily visualized by comparing panels arranged in a given column. Somerville et al. (2004) estimate that the relative cosmic variance on the observed number counts for LBGs in the GOODS fields will be $\sigma_V \sim 0.15$. Since our observed cosmic variance (ie., the shifting of the distributions in a given column of Figure 19) is consistent with their estimate for σ_V, we do not attempt to include any additional source of cosmic counting uncertainty.

We summarize our merger statistics for the three fields in Table 7. For each dropout type (or redshift), we compute the averages of the three fields and take

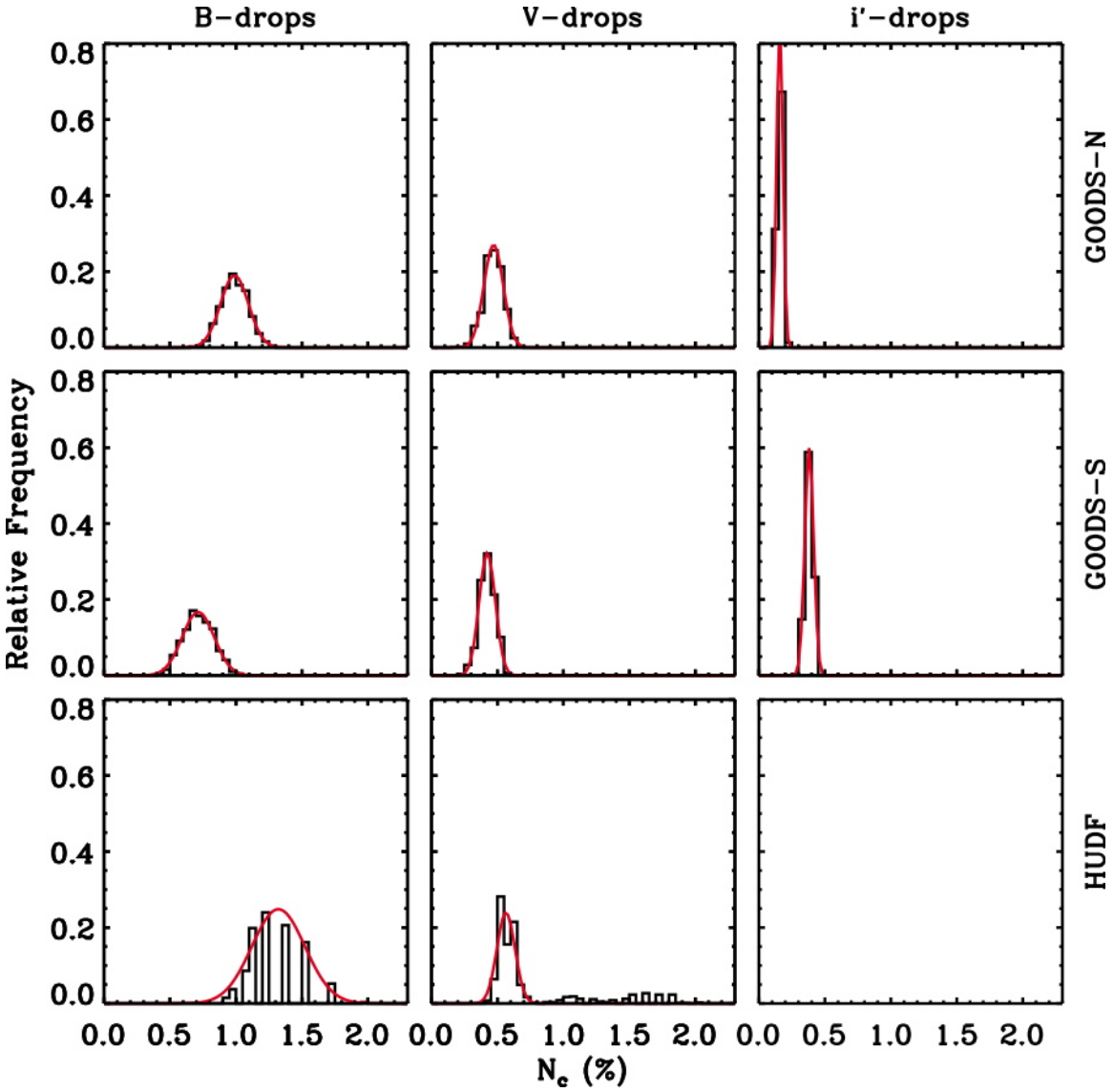

FIG. 19. Since the typical redshift uncertainty for the LBG selection is $\sigma_z \sim 0.3$, some galaxy pairs could be simply line-of-sight projections and corrupt the true merger signal. Therefore, we use a Monte Carlo simulation, where the redshifts of the galaxies are drawn from a normal distribution with mean and standard deviation given in Table 5. In the black histograms, we show the results of this Monte Carlo simulation the Gaussian fit in red. Owing to the small sample size, there are no i'-band dropouts in the HUDF which met all four close pair criteria discussed in § 5.3.1. This figure is reproduced from Ryan et al. (2008b).

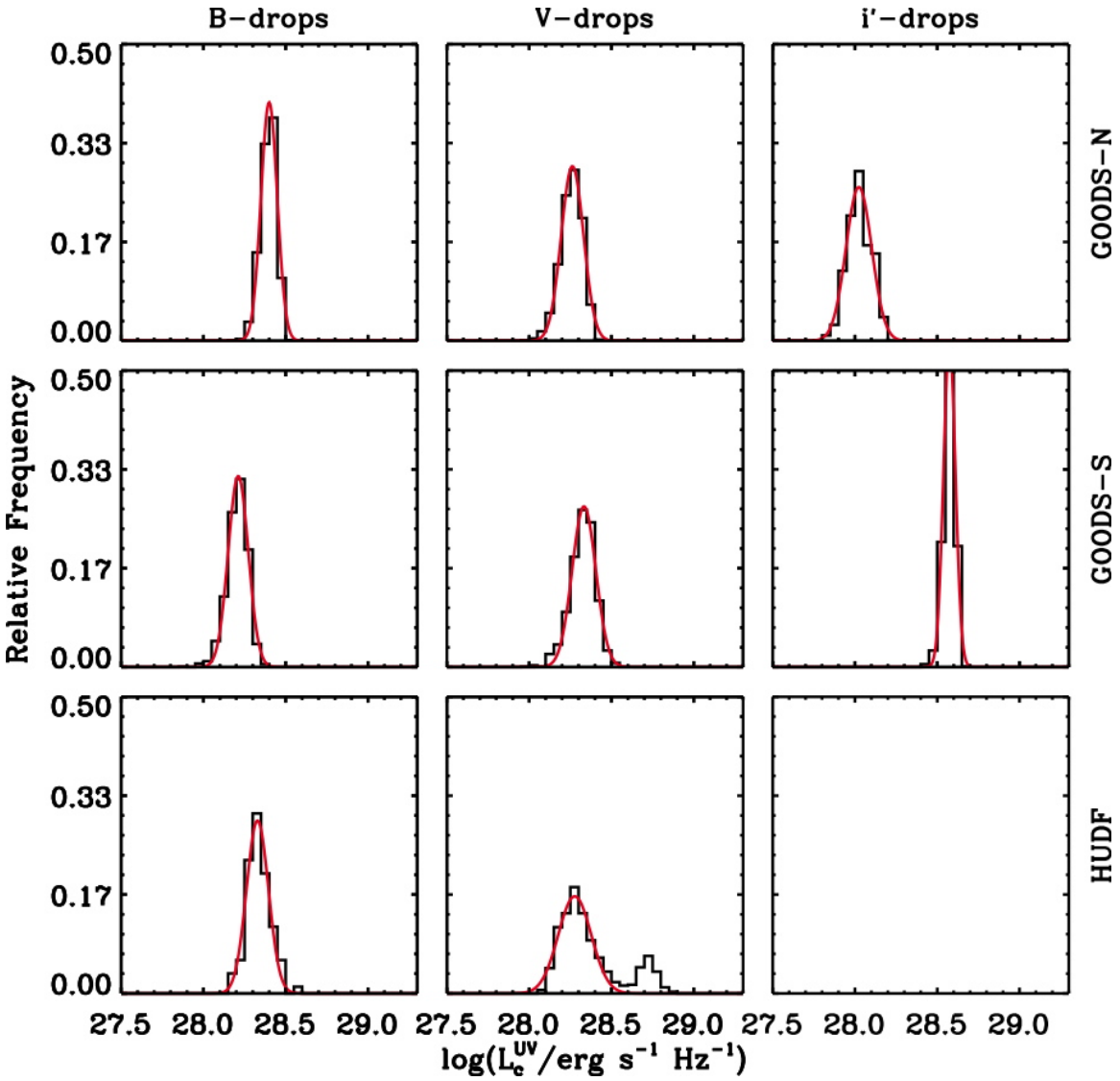

FIG. 20. Like the pair fraction, the luminosity of close companions must be computed with a similar Monte Carlo analysis. As in Figure 19, we show the Monte Carlo results as a black histogram and the Gaussian fit as a red line. These luminosities are derived from the restframe far-ultraviolet ($\lambda_{\rm rest} \simeq 1500$ Å), and are used to compute the comoving luminosity (see equation 5.15) and star formation rate densities (see Table 7). This figure is reproduced from Ryan et al. (2008b).

the 1σ minimum and maximum deviations as the lower and upper uncertainties, respectively. From Table 7, we find that the wider and shallower GOODS fields generally provide stronger constraints on the merger statistics, since we select super-L^* galaxies ($M_B \leq -20.5$ mag). However, the HUDF should be superior to the GOODS fields for determining the merger rate of less luminous or lower mass systems (sub-L^* galaxies), which can dominate the total merger rate (Patton & Atfield 2008).

TABLE 7
Dropout Merger Results

Dropout	N_c	n (10^{-4} Mpc^{-3})	$\log L_c^{\rm UV}$ (erg s^{-1} Hz^{-1})	$\log \rho$ ($M_\odot$ yr^{-1} Mpc^{-3})
B	0.0099 ± 0.0011	0.387 ± 0.046	28.40 ± 0.05	-1.911 ± 0.05
V	0.0047 ± 0.0007	0.128 ± 0.021	28.26 ± 0.07	-2.199 ± 0.07
i'	0.0016 ± 0.0002	0.041 ± 0.007	28.02 ± 0.08	-2.478 ± 0.08
		GOODS-S		
B	0.0072 ± 0.0012	0.238 ± 0.041	28.21 ± 0.06	-2.174 ± 0.07
V	0.0042 ± 0.0006	0.101 ± 0.016	28.33 ± 0.07	-2.192 ± 0.08
i'	0.0038 ± 0.0003	0.094 ± 0.009	28.57 ± 0.04	-1.937 ± 0.05
		HUDF		
B	0.0131 ± 0.0017	0.198 ± 0.067	28.31 ± 0.07	-2.418 ± 0.15
V	0.0057 ± 0.0006	0.133 ± 0.034	28.28 ± 0.10	-2.258 ± 0.14
i'	...	...	...	...
		Average†		
B	$0.0101^{+0.0047}_{-0.0040}$	$0.274^{+0.159}_{-0.144}$	$28.31^{+0.14}_{-0.16}$	$-2.168^{+0.40}_{-0.40}$
V	$0.0049^{+0.0014}_{-0.0012}$	$0.121^{+0.046}_{-0.035}$	$28.29^{+0.11}_{-0.12}$	$-2.216^{+0.19}_{-0.19}$
i'	$0.0027^{+0.0014}_{-0.0014}$	$0.068^{+0.036}_{-0.034}$	$28.30^{+0.31}_{-0.35}$	$-2.208^{+0.35}_{-0.35}$

†These values are computed as averages and min/max ranges from above three fields (see Figure 19 and Figure 20).

5.4. Evolution of the Galaxy Merger Rate

5.4.1. *The Galaxy Merger Fraction*

The galaxy merger rate is proportional to the ratio of the merger fraction and assumed merger timescale (eg. Patton et al. 2000). In general, the merger timescale is assumed to be constant with redshift at $\tau_{\rm mg} \sim 1$ Gyr, although it may slightly depend on the adopted mass or luminosity limits (Kitzbichler & White 2008). In order to compare to a series of observations at lower redshifts ($z \lesssim 3$), we will only discuss the merger fraction. For our intermediate redshift merger study ($0.5 \leq z \leq 2.5$; Ryan et al. 2008a), we selected pairs based on their stellar mass of $M_* \geq 10^{10}$ M$_\odot$ as derived from stellar population fits to the HUDF grism observations (Pirzkal et al. 2004; Ryan et al. 2007). The median stellar mass-to-light ratio for these galaxies was $\Upsilon_{*,B} \simeq 0.5$ M$_\odot$ L$_\odot^{-1}$ (see § 4.4), which implies an absolute magnitude selection of $M_B \leq -20.5$ mag (for $M_{B,\odot} = +5.2$ mag). Therefore, our merger pairs identified in this work are directly comparable to a number of lower redshift studies, which were selected based on their B-band luminosities. In Figure 21, we show the merger fractions from Patton et al. (1997) (*open triangles*), Le Fèvre et al. (2000) (*open diamonds*), Ryan et al. (2008a) (*filled circles*) and this work (*open squares*). As we noted in Ryan et al. (2008a), the merger fraction can only be well-represented by a power-law in $(1 + z)$ for redshifts $z \lesssim 1$, and likely peaks at some redshift ($z_{\rm max}^{\rm frac}$). Therefore, we fit the observed merger fraction with the empirical model of Conselice (2006):

$$f(z) = a(1 + z)^b e^{-c(1+z)}. \tag{5.11}$$

In Figure 21, we show the best-fit model with $a = 0.21 \pm 0.02$, $b = 5.54 \pm 0.26$, and $c = 2.34 \pm 0.10$ with $\min(\chi^2)/\text{d.o.f.} = 7.7/7$ as a solid line, and show the confidence intervals in the $(b - c)$ plane as an inset. When accounting for the correlated uncertainties on b and c, we find that this peak redshift can be reasonably well constrained: $z_{\rm max}^{\rm frac} = (b/c) - 1 = 1.37 \pm 0.10$.

To investigate the cumulative effect of major merging on galaxy populations, we compute the major merger remnant fraction, which is defined as the fraction of galaxies that have experienced a major merger between today and a given redshift. Following Patton et al. (2002, their equation (18)), the merger remnant fraction critically depends on the merger timescale and the functional form of the pair fraction. Therefore, in Figure 22 we show the remnant fraction for various merger timescales ranging from $\tau_{\rm mg} = 0.25 - 1.5$ Gyr, as indicated in the lower-right. In addition, we plot the remnant fraction for the traditional power-law form of the pair fraction, $f(z) = 0.02 \times (1 + z)^3$ as blue lines, and our results from Equation (5.11) as red lines. Since our derived pair fractions exponentially decline for $z \gtrsim 1$, the merger remnant fraction tends to approach a limiting value of $f_{\rm rem}^{\rm lim} \simeq 53\%$ and 78% for $\tau_{\rm mg} = 0.5$ Gyr and 0.25 Gyr, respectively.

5.4.2. *The Galaxy Merger Number Density*

In the hierarchical formation paradigm, galaxy merging plays a lead role in galaxy assembly. Therefore, the number density of galaxy mergers will be a key quantity in setting the rate or the magnitude of a variety of effects which are triggered by merging. We convert our merger fraction estimates (N_c) into the number density

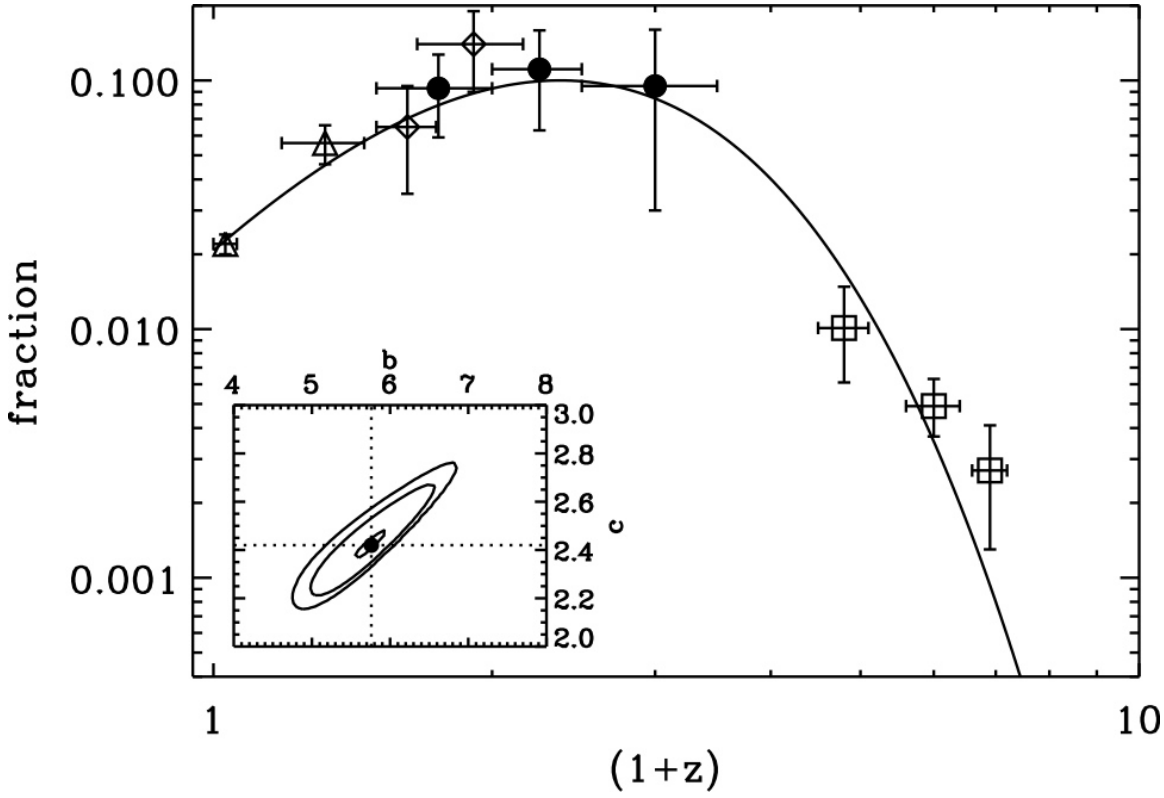

FIG. 21. We show the fraction of major mergers from Patton et al. (1997) (*open triangles*), Le Fèvre et al. (2000) (*open diamonds*), Ryan et al. (2008a) (*filled circles*), and this work (*open squares*). While the merger fraction shows the usual power-law increase for $z \lesssim 1$, there is clear peak at $z_{\rm max}^{\rm frac} = 1.37 \pm 0.10$. Therefore, we fit these observations with the empirical model given as Equation (5.11). We find the best-fit model has $a = 0.21 \pm 0.02$, $b = 5.54 \pm 0.26$, and $c = 2.34 \pm 0.10$ with $\min(\chi^2)/{\rm d.o.f.} = 7.7/7$. In the inset, we show the 68.3%, 95%, and 99% confidence intervals in the $(b-c)$ plane, which serves to highlight the correlation between b and c. While this fit is similar to those found by Ryan et al. (2008a) and Conselice, Rajgor, & Myers (2008), our new $z \gtrsim 3$ data points markedly decrease the uncertainty on the peak redshift. This figure is reproduced from Ryan et al. (2008b).

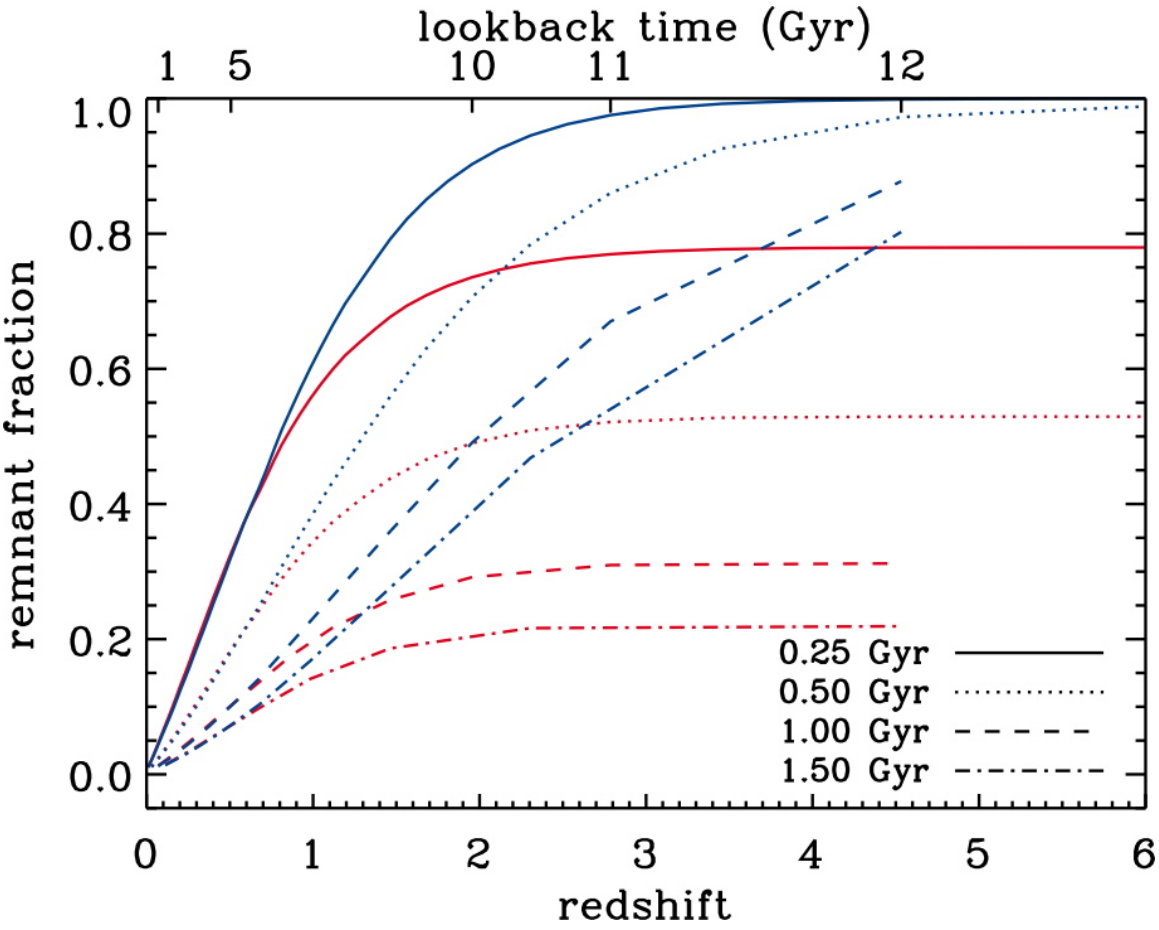

FIG. 22. The remnant fraction represents the fraction of galaxies which have experienced a major merger between a given redshift and today. They are computed from equation (18) of Patton et al. (2002) for the merger timescales ($\tau_{\rm mg}$) in the lower-right, the power-law pair fraction of $f(z) = 0.02 \times (1+z)^3$ (blue lines) and our derived pair fraction Equation (5.11) (red lines). Since the power-law pair fraction increases *ad infinitum* with redshift, every galaxy will eventually experience a major merger. However, our derived pair fraction exponentially declines for $z \gtrsim 1$, which implies that some fraction of galaxies, $(1 - f_{\rm rem}^{\rm lim})$ have never undergone a major merger in the Hubble time. This figure is reproduced from Ryan et al. (2008b).

of merging systems by:

$$n_{mg} = N_c \frac{N_{\rm LBGs}(M < M_{\rm lim})}{\int dV(z)}, \tag{5.12}$$

where $N_{\rm LBGs}(M < M_{\rm lim})$ is the number of LBGs that meet our absolute magnitude criterion and $dV(z)$ is the cosmological volume element. Since this criterion will only select galaxies brighter than our flux limit transformed into an absolute magnitude limit (see Equation 5.1), the incompleteness at the faint-end can be minimized. In Figure 23, we show the number density of mergers for the same four surveys as in Figure 21. We propose a new empirical fitting function for the number density, which is similar to the luminosity-dependent density evolutionary model (LDDE) for X-ray selected AGN (eg. Ueda et al. 2003; Hasinger, Miyaji, & Schmidt 2005):

$$n(z) = n_0 \frac{(1+\epsilon)(1+z)^{\alpha}}{1+\epsilon(1+z)^{\beta}}. \tag{5.13}$$

We show the best-fit model as a dashed line with $n_0 = (7.88 \pm 3.21) \times 10^{-6}$ Mpc^{-3}, $\epsilon = (1.17 \pm 1.11) \times 10^{-3}$, $\alpha = 6.83 \pm 1.41$, and $\beta = 10.4 \pm 1.1$ with $\min(\chi^2)/{\rm d.o.f.} = 11.5/6$. We must stress, this functional form is *purely* empirical, and is only motivated by the observed power-law forms at $z \lesssim 0.5$ and $z \gtrsim 2$. Like the Conselice (2006) model for the merger fraction, our form for the number density has peak at a redshift, which is given by

$$z_{\rm max}^{\rm dens} = \left[\frac{\alpha}{\epsilon(\beta - \alpha)}\right]^{1/\beta} - 1. \tag{5.14}$$

For our observations in Figure 23, we find $z_{\rm max}^{\rm dens} = 1.04 \pm 0.10$. Our proposed functional form has the attractive property that for $\epsilon \to 0$ we recover a pure power-law increase with slope α, while for $\epsilon \to \infty$ there is a sharp power-law decrease with slope $(\alpha - \beta)$. Since α and β are essentially determined by the observed slopes, ϵ is a measure of

the degree to which the data require the two-component power-law. We note that for fixed power-law slopes, the peak redshift is entirely set by ϵ.

The Patton et al. (2000) method optimally weights primary and companion galaxies as a function of their brightnesses to correct the merger counts for flux incompleteness. Therefore, we do not expect to significantly underestimate our merger fractions or densities at $z \gtrsim 3$. However, there are two additional points worth mentioning: (1) If the galaxy merger triggers a substantial starburst, then we may expect that the galaxy pairs to have higher surface brightnesses than field galaxies at the same redshift. Therefore, such galaxy pairs will be proportionally easier to detect and may be less affected by flux incompleteness; (2) Since the merger fraction is essentially the ratio of two quantities, any multiplicative completeness correction which affects the merging and non-merging galaxies equally, will not have any effect on our results.

5.4.3. *Star Formation Rate Densities*

The greatest strength of the Patton et al. (2000) selection algorithm is the ability to correct the flux-limited merger counts. In addition to the merger counts, this method also determines the mean luminosity in close-companions. By computing this luminosity at $\lambda_{\rm rest} \simeq 1500$ Å (which we denote as $L_c^{\rm UV}$), we are able to determine the contribution of major mergers to the cosmic star formation rate density at $z \gtrsim 3$. The luminosity density is

$$\mathcal{L}(z) = L_c^{\rm UV} \frac{N_{\rm LBGs}(M < M_{\rm lim})}{\int dV(z)}, \tag{5.15}$$

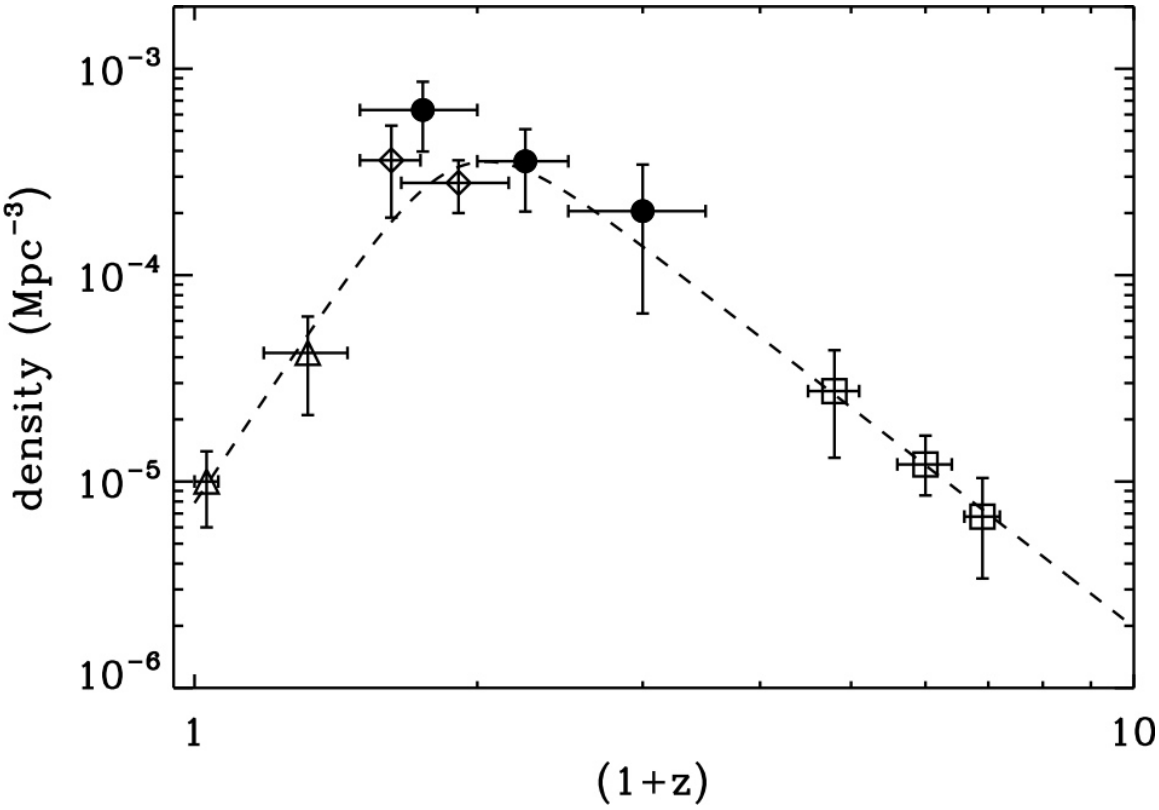

FIG. 23. The data points represent the same surveys shown Figure 21. While the exponentially-decaying power-law was an appropriate fit for the merger fraction, it requires a model of the evolution of the galaxy number density. To avoid this assumption, we propose a different empirically motivated fitting-function of a two-component power-law in $(1+z)$, see Equation (5.13). While this function was inspired by the LDDE model for X-ray selected AGN (Ueda et al. 2003), it is only motivated by the deep observations, not necessarily by any physical insight. The best-fit to these data points gives $\min(\chi^2)/\text{d.o.f.} = 11.5/6$ for $n_0 = (7.88 \pm 3.21) \times 10^{-6}$ Mpc^{-3}, $\alpha = 6.83 \pm 1.41$, $\epsilon = (1.17 \pm 1.11) \times 10^{-3}$, and $\beta = 10.4 \pm 1.1$, which gives a peak redshift of $z_{\rm max}^{\rm dens} = 1.04 \pm 0.10$. This figure is reproduced from Ryan et al. (2008b).

where $L_c^{\rm UV}$ is the mean UV luminosity of the close companions in the units of erg s^{-1} Hz^{-1}. Finally, the *dust-uncorrected* star formation rate density, $\rho(z)$, in the units of M$_\odot$ yr^{-1} Mpc^{-3} is $\rho(z) = 1.25 \times 10^{-28} \mathcal{L}(z)$ (Bouwens et al. 2007), which we give in Table 7. Since determining the extinction for a given galaxy requires many multiwavelength observations (eg. Meurer et al. 1997), we can only apply crude extinction corrections to the star formation rates. Following Bouwens et al. (2007), the dust-corrected star formation rates for the BVi'-band dropouts are generally a factor of 2.7, 2.0, and 1.5 times higher than the uncorrected rates, respectively. However, high resolution observations at longer wavelengths can confirm these corrections, which will be a major focus for the James Webb Space Telescope (JWST).

5.5. Discussion

Since its inception, the dropout technique has been employed by a number of authors to select and study high redshift galaxies in detail. Yan & Windhorst (2004b) identified 108 i'-band dropouts in the HUDF, and they noted that only nine of these sources appear to be in multiple systems separated by $\Delta r \lesssim 8$ kpc. Since the multiple components in a given system have roughly comparable brightnesses, they are likely major mergers. However these particular systems were not identified in this work, since they are individually fainter than our absolute magnitude limits. Similarly, Rhoads et al. (2005) suggest that the linear morphology of the object, UDF 5225, at $z \approx 5.4$ may be caused by a recent galaxy merger. While the image asymmetry corroborates this argument, the ambiguity in selecting the centroid for the asymmetry algorithm leaves some room for debate. While these case-studies suggest a relatively

high merger fraction at $z \simeq 6$, roughly 50% of the BVi'-band dropouts in the HUDF are isolated and compact sources (Hathi et al. 2008a; Hathi, Malhotra, & Rhoads 2008b), indeed implying a relatively low merger fraction for luminous LBGs.

As discussed in § 5.1, the duty cycle of merging followed by starburst followed by AGN provides a formation paradigm for most massive galaxies (Hopkins et al. 2006). Its most attractive feature is that it provides a triggering mechanism for the AGN, whose feedback is essential in terminating the merger-driven starburst, and may ultimately cause the galaxy downsizing. Whether this negative feedback comes in the form of energetic outflows (Scannapieco, Silk, & Bouwens 2005) or the energy deposition of hard X-rays (Daddi et al. 2007), it seems essential in the formation of massive galaxies. Therefore, we expect to observe an increased star-formation rate for close pair galaxies when compared to field galaxies. Based on their restframe UV luminosities, we find that the star-formation rate density of close pairs at $z = 3.8 \pm 0.3$, 5.0 ± 0.4, and 5.9 ± 0.3 is 34%, 67%, and 97% of the totals found by Bouwens et al. (2007) for our absolute magnitude limits, respectively. These relatively high fractions suggest that the star formation rate is significantly enhanced for close pairs, as may be expected for a merger-driven starburst and is qualitatively consistent with observations at $z \sim 0$ (eg. Ellison et al. 2008).

This merger-induced AGN model is complicated by somewhat conflicting observations. Some quasar (QSO) host galaxies have unmistakable merger features (Bahcall et al. 1997), disturbed morphologies (Urrutia, Lacy, & Becker 2008), or shell structures (Canalizo et al. 2007). Conversely, AGN with modest X-ray lumi-

nosities at $z \lesssim 1.3$ generally do not show enhanced image asymmetries or increased close-pair counts, but rather have generally high central concentrations (Grogin et al. 2005). Furthermore, Silverman et al. (2008) find highest fraction of luminous galaxies ($M_V < -20.7$ mag) which harbor AGN are blue ($(U-V) < 0.7$ mag), bulge-dominated (Sérsic index of $n > 2.5$) systems at $0.4 \leq z \leq 1.1$. This argues for AGN that are significantly bulge-dominated and without a merger origin. No matter what the connection between galaxy mergers and AGN may be, our merger number density can offer some independent, but still circumstantial evidence. If a major merger of two massive galaxies is the dominant mechanism to trigger a QSO or luminous AGN, then these two populations should have similar densities with redshift. Indeed their functional forms are similar, however the galaxy mergers peak at a somewhat higher redshift. The redshift offset of $\Delta z \sim 0.3$ between the major merger and AGN space densities corresponds to a cosmic time difference of $\Delta t \sim 2$ Gyr, which suggests that luminous AGN activity is maximized ~ 2 Gyr *after* a major merger (eg. Ryan et al. 2008a). This time delay is consistent with the hydrodynamical and semi-analytic models of Springel, Di Matteo, & Hernquist (2005a), where $\sim 1-2$ Gyr is required to expel the circumnuclear dust and observe the merger remnant as a QSO or AGN. Moreover, this delay is seen in the stellar population ages of many classical QSOs, which often show traces of major star formation episodes $\sim 1-2$ Gyr in their past (Canalizo et al. 2006).

Since our derived merger fraction clearly peaks at $f(z_{\rm max}^{frac}) \simeq 10\%$, the fraction of galaxies which have experienced a major merger within the Hubble time (the

remnant fraction) is roughly $f_{\rm rem}^{\rm lim} \sim 53\%$ (for a merger timescale of $\tau_{\rm mg} = 0.5$ Gyr). Therefore, a non-negligible fraction of local galaxies, $(1 - f_{\rm rem}^{\rm lim}) \sim 47\%$, may not have undergone a major merger, however this does not exclude the possibility of a series of minor mergers. These galaxies would most likely have formed in a "monolithic" collapse (Eggen, Lynden-Bell, & Sandage 1962) followed by secular evolution with possible minor infall, where the majority of their mass must have been assembled at early epochs. We speculate that such systems may be progenitors of some local elliptical galaxies, which often exhibit properties pointing to a monolithic formation, such as their short star formation timescales (eg. Papovich et al. 2006), the small scatter in color-magnitude diagrams (eg. Bower, Lucey, & Ellis 1992), or structural properties of the fundamental plane (eg. Bender, Burstein, & Faber 1992). This conjecture may be supported by the existence of massive and evolved galaxies at very high redshifts (eg. Eyles et al. 2005; Mobasher et al. 2005; Wiklind et al. 2008).

CHAPTER 6

The Distribution of L- & T-Dwarfs in the Galaxy

6.1. Introduction

The method of counting stars to infer the shape and size of the Galaxy is as old as astronomy itself. Earliest efforts using this technique were flawed as they often relied on insufficient data, or incorrect assumptions (eg. Herschel 1785; Kapteyn 1922). Aided by advanced technology, Bahcall & Soneira (B&S; 1980, 1981) demonstrated that the true power of star counts is realized when they are compared to simulations of the fundamental equation of stellar statistics (von Seeliger 1898). The B&S method relies heavily on the assumed stellar luminosity functions and density distributions, and has been a standard method for many subsequent studies.

The Galaxy is traditionally characterized by having a Population I disk and a Population II spheroid. In a series of studies of the Galactic exponential disk, Gilmore & Reid (1983) and Gilmore (1984) established the need for a thick and thin disk, whose scale heights are inversely proportional to the masses of the studied stars (see Table 1 in Siegel et al. 2002). The standard description of the Galactic halo is a de Vaucouleurs or power-law profile, while a Besançon flattened spheroid with $c/a \approx 0.5 - 0.8$ (Bahcall & Soneira 1984; Robin, Reylé, & Crézé 2000; Larsen & Humphreys 2003; Robin et al. 2003) represents the currently favored shape. Thorough discussions of star counts and their relevance to Galactic structure are given in the Annual Reviews by Bahcall (1986), Gilmore, Wyse, & Kuijken (1989), and Majewski (1993).

Many of the Galactic models and the majority of the literature examine only relatively luminous dwarf and/or giant stars, and rarely address sub-stellar objects.

The discovery of the first extra-solar, sub-stellar object, Gliese 229B (Nakajima et al. 1995; Oppenheimer et al. 1995) motivated the creation of the L and T spectral classes. With surface temperatures ranging from 750–2200 K (Burgasser 1999), the L- & T-dwarfs can contaminate searches for i'-band dropout objects at $z \simeq 6$ by mimicking the extremely red broadband colors (Yan & Windhorst 2004b; Caballero, Burgasser, & Klement 2008). This effect has remained largely unquantified due to insufficient knowledge of the L- & T-dwarf IMF, Galactic distribution, and their local number density. Previous work on their IMF and local number density (Reid et al. 1999; Chabrier 2001, 2002; Liu et al. 2002) has suffered from limited statistics. With the deep imaging of 15 Hubble Space Telescope (HST) Advanced Camera for Surveys (ACS) parallel fields, the current study increases the number of *faint* dwarfs by adding 28 new such candidates to the growing list. Little work has been done on the vertical scale height of L- & T-dwarfs — Liu et al. (2002) and Pirzkal et al. (2005) estimated 100–400 pc as based on a single object or a 3–4 objects in a single field. Therefore, the primary goal of this Chapter is to more accurately estimate the scale height of the L- & T-dwarf population by comparing the surface densities from the ACS parallel fields to the Galactic structure models.

This Chapter is organized as follows: in § 6.2 we describe the HST/ACS parallel observations, in § 6.3 we construct our Monte Carlo model of the Milky Way, in § 6.4 we analyze our models, in § 6.5 we outline several sources of contamination to our L- & T-dwarf counts, and § 6.6 we discuss our results in the context of photometric

surveys for high redshift ($z \simeq 6$) galaxies. We adopt the AB magnitude system throughout (Oke & Gunn 1983).

6.2. Observations

The L- & T-dwarf candidates were selected from 15 HST/ACS parallel fields, covering a broad range in Galactic latitudes and longitudes (see Table 8). All ACS fields have at least three independent exposures in F775W (SDSS-i') and F850LP (SDSS-z') with a total exposure time of 2–10 ks per bandpass. All fields are $\gtrsim$90% complete at $z' \simeq 26.0$ mag (Yan & Windhorst 2004a).

After combining the individual ACS frames into final stacks using the PyRAF-based script `multidrizzle` (Koekemoer et al. 2002), the SExtractor package (Bertin & Arnouts 1996) was used in double-input mode to perform the matched-aperture photometry. The F850LP stack was used to define the optimal apertures for the flux measurements in both stacks. For source detection, we used a 5×5 Gaussian smoothing kernel with a FWHM of 2.0 pixels, which has approximately the same width as the FWHM of the ACS point-spread function (PSF) on both image stacks. We used total magnitudes (corresponding to the `MAG_AUTO` option in SExtractor) for the photometry, and adopted the zero points published in HST ACS Instrument Science Report (De Marchi et al. 2004).

As a cursory selection of the L- & T-dwarfs, all objects with $(i' - z') > 1.3$ mag and $z' < 26.0$ mag were considered. Figure 24 is the color-magnitude diagram for all point sources detected in all 15 fields. Dashed lines indicate the imposed color-magnitude limits, and the large filled stars represent the candidate L- & T-dwarfs.

For the five fields for which the F475W (SDSS-g') band was available, we required candidates to also have $(g' - i') > 0$ mag. Objects near the detector edges were not considered, yielding an effective area of ~ 9 arcmin^2 per ACS field. Extended objects were eliminated from the analysis by using the FWHM parameter of SExtractor. In Figure 25, we plot the FWHM as a function of apparent magnitude for each object in Field 1 as small dots. The locus of points at FWHM $\sim 0\farcs13$ and $z' < 26$ mag (hereafter the "stellar locus") are the unresolved objects with the minimum possible FWHM and are represented as asterisks in Figure 25. In addition to the above color-magnitude criterion, we required all L- & T-dwarf candidates to lie within this locus. Sources of contamination to these criteria are discussed in § 6.5.

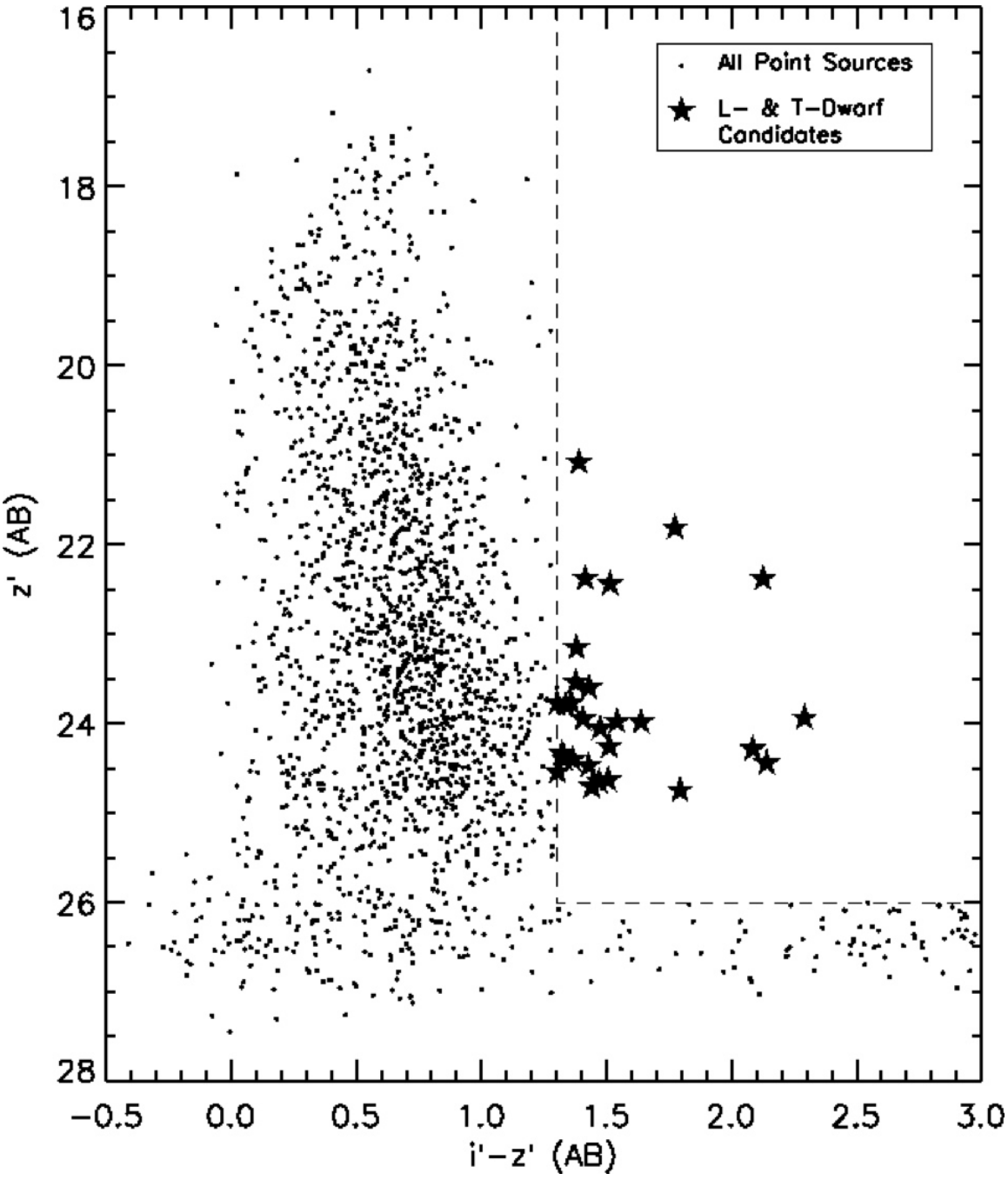

FIG. 24. The small dots represent all objects that met the stellar morphology classification. The solid stars mark the 28 L- & T-dwarf candidates, and the dashed lines represent the imposed color-magnitude limits. Many point sources associated with diffraction spikes, field edges, and spurious detections — ie., objects smaller than the PSF, likely residual cosmic rays — brighter than $z' = 26$ mag were manually removed. The similar points fainter than $z' = 26$ mag were not removed from this figure, since the entire sample is incomplete for $z' \gtrsim 26$ mag. The sample of stellar candidates, becomes incomplete for $z' \geq 25$ mag. This figure is reproduced from Ryan et al. (2005).

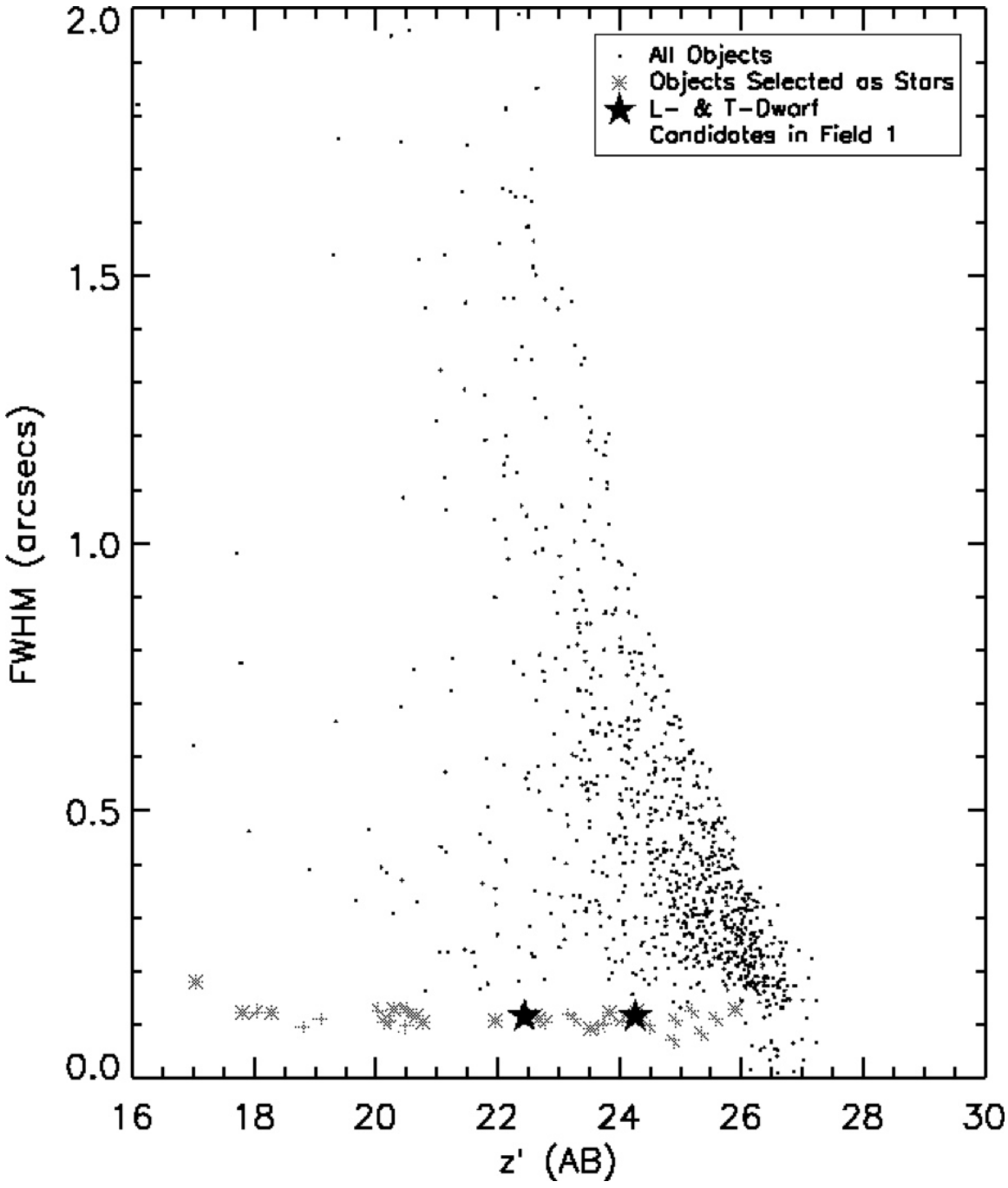

FIG. 25. The small dots represent all sources in field 1, while the asterisks mark objects which are point sources in the HST/ACS imaging, which define the "stellar locus." The large filled stars represent those point sources that meet the color criterion of $(i' - z') > 1.3$ mag and are taken to be L- & T-dwarfs. This figure is reproduced from Ryan et al. (2005).

TABLE 8
L- & T-Dwarf Number Counts

Field No.	l^{II} (deg)	b^{II} (deg)	Number (per 9 arcmin^2)
1	115.018	+46.681	2
2	164.056	−75.750	1
3	169.188	−59.664	0
4	279.934	−19.990	3
5	165.876	+36.396	0
6	280.782	+68.293	0
7	113.107	+28.548	2
8	293.996	−41.466	0
9	316.829	−40.490	1
10	105.103	+7.075	11
11	298.138	−13.885	6
12	92.666	+46.378	1
13	70.106	+62.876	0
14	251.327	−41.444	0
15	216.142	+54.561	1

Typically Galactic structure studies examine the star counts from one or many shallow fields with large surveyed areas (eg. Siegel et al. 2002; Larsen & Humphreys 2003). Thus the data of the 2MASS (Burgasser 1999; Kirkpatrick et al. 1999), DENIS (Delfosse 1999), and/or SDSS (Strauss et al. 1999; Tsvetanov et al. 2000; Hawley et al. 2002) are natural choices to study the Galactic distribution of the L- & T-dwarfs. These surveys have significantly more detection area than our HST dataset, and their L- & T-dwarfs are typically closer to the Sun than $\sim$300 pc or $\sim$1 disk scale height. Therefore, to avoid *extrapolating* the vertical scale height beyond this distance, we chiefly analyzed the HST dataset, where all sample stars are likely more distant than about one e-folding length.

6.3. The Simple Galactic Model

The Galactic structure models were made by distributing 10^{10} points according to an exponential disk that was motivated by the light profiles of edge-on galaxies (de Grijs, Peletier, & van der Kruit 1997):

$$n(r,\theta,z) = n_0 \exp\left(\frac{R_0 - r}{r_l}\right) \exp\left(\frac{Z_0 - z}{z_h}\right), \tag{6.1}$$

where $r_l = 2100$ pc is the radial scale length found by Porcel et al (1998), $n_0 = 0.12$ pc^{-3} is the local space density L- & T-dwarfs taken from Chabrier (2002), and $R_0 = 8$ kpc and $Z_0 = 15$ pc (Yamagata & Yoshii 1992) are the solar orbital radius and height above the disk, respectively. The vertical scale height (z_h) is the free parameter and was found by minimizing the squared difference between the number counts from the model and the HST data. Altering the assumed coordinates of the Sun, and the radial scale length have little effect on the vertical scale height estimate. To generate

absolute magnitudes, we adopted the J-band luminosity function of Cruz et al. (2003) and the $(z' - J)$ colors of Hawley et al. (2002) over the appropriate range of spectral type.

The effects of interstellar extinction were included into the model using the COBE dust maps of Schlegel et al. (1998) in two ways. First, we assumed that each point was located beyond the dust, establishing a lower bound on the model counts. Alternatively, an upper bound is reached by assuming that the Galaxy has *no* dust whatsoever. Since an overwhelming majority of the dust is localized to $|b^{\rm II}| \lesssim 15^\circ$ (see Figure 26) and only two of our observed ACS fields are in this range, either approach yielded the same result within the uncertainties. Therefore we adopted the third method for simplicity. Figure 26 is a representative realization the model with a scale height of 350 pc, where the locations of the 15 observed ACS fields are indicated with plus signs.

The canonical disk/spheroid Galaxy likely has additional components (Bahcall 1986). However, the models used here did not contain any contribution from the Galactic bulge or a two-component disk (Gilmore & Reid 1983; Gilmore 1984) for the following reasons. First, a bulge distribution was not modeled since its radius is $\sim 1 - 2$ kpc or $\sim 7^\circ - 14^\circ$ as observed from Earth, and every field is more distant than 14° of the Galactic center. Hence, we do not require a bulge component in the model. Second, this sample contains only 28 L- & T-dwarfs, which are likely only ~ 1 kpc from the Sun, given their observed brightnesses and typical luminosities. Since the thick disk has a scale height of $\gtrsim 1$ kpc, we expect the star counts to be dominated

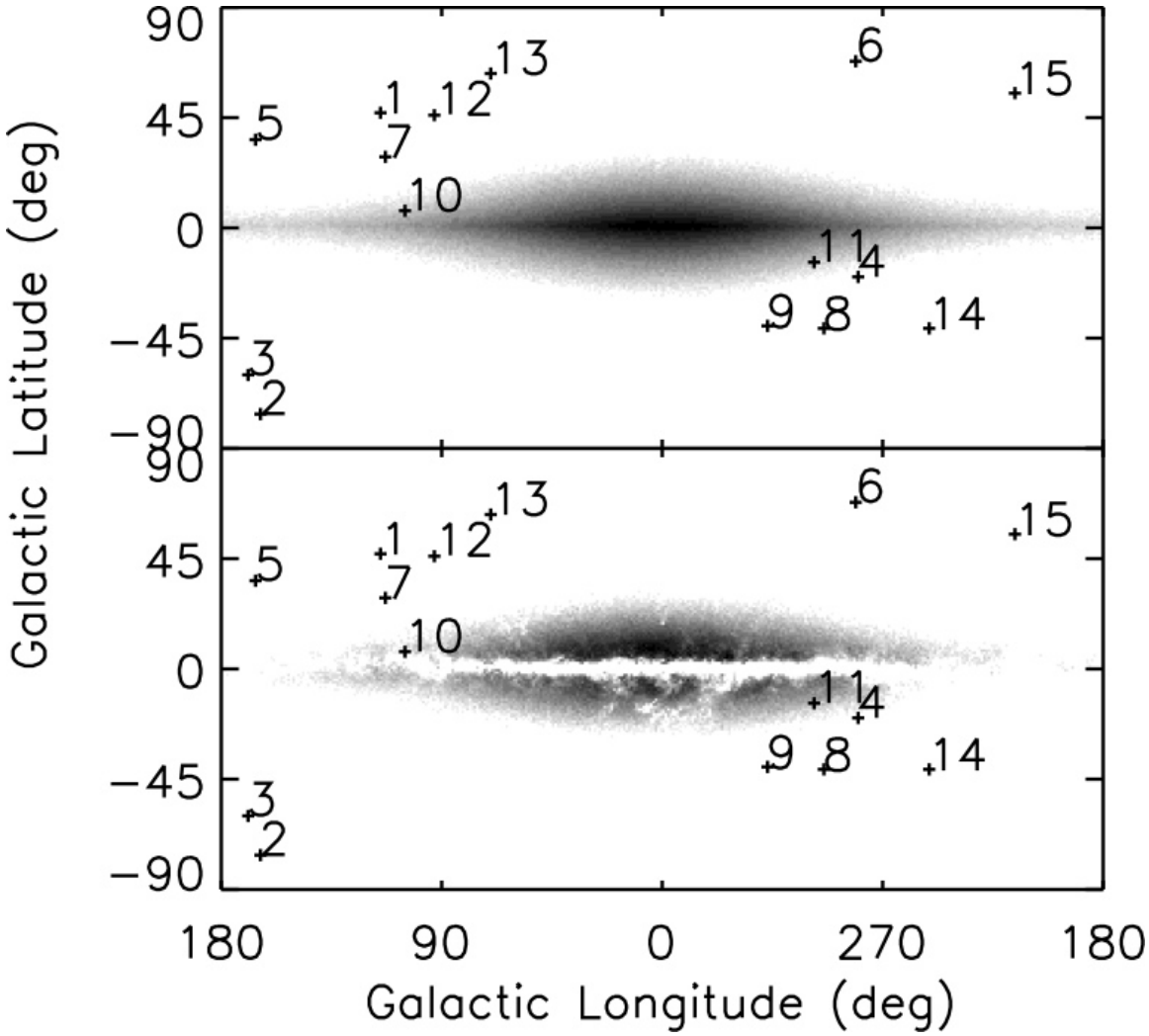

FIG. 26. The over-plotted plusses with numbers represent the observed HST/ACS fields in Table 8. The effects of the Schlegel et al. (1998) dust maps are readily apparent, when comparing the upper (no extinction) and lower (extinction) panels. This realization has a vertical scale height of $z_h = 350$ pc. This figure is reproduced from Ryan et al. (2005).

by a *single* disk population. Moreover, with only 28 L- & T-dwarf candidates, the models and analyses must remain simple and straightforward.

6.4. Analysis

Despite this work utilizing the largest dataset of L- & T-dwarfs compiled from HST observations, the resulting star counts remain low and require a simple analysis scheme. Using the grid of Monte Carlo models described in § 6.3, we found the scale height value that minimizes the squared difference between the integrated star counts of the model and those from the HST/ACS dataset. For the fields where no L- & T-dwarf candidates were found, we assumed that an upper limit of one object (per field) could have been detected. We perform this minimization technique simultaneously on all 15 fields. This procedure yielded a vertical scale height of 350 ± 50 pc. In the upper panel of Figure 27, we plot the modeled surface density averaged over Galactic longitude as a function of Galactic latitude for a scale height of 350 pc. The HST star counts from Table 8 are indicated for direct comparison. The residuals in the lower panel clearly demonstrate that the model with a scale height of 350 pc reproduces the HST star counts for $\left|b^{\rm II}\right| \geq 15°$, where dust extinction is minimal.

6.5. Sources of Contamination

While all L- & T-dwarf candidates were systematically found by color and FWHM criteria, each was visually confirmed as a point source. However, the color-magnitude rules outlined in § 6.2 potentially find three classes of contaminates:

(1) The primary motivation of this study is to reliably correct the i'-band dropout galaxy surveys for interloping L- & T-dwarfs (Yan et al. 2002; Yan, Wind-

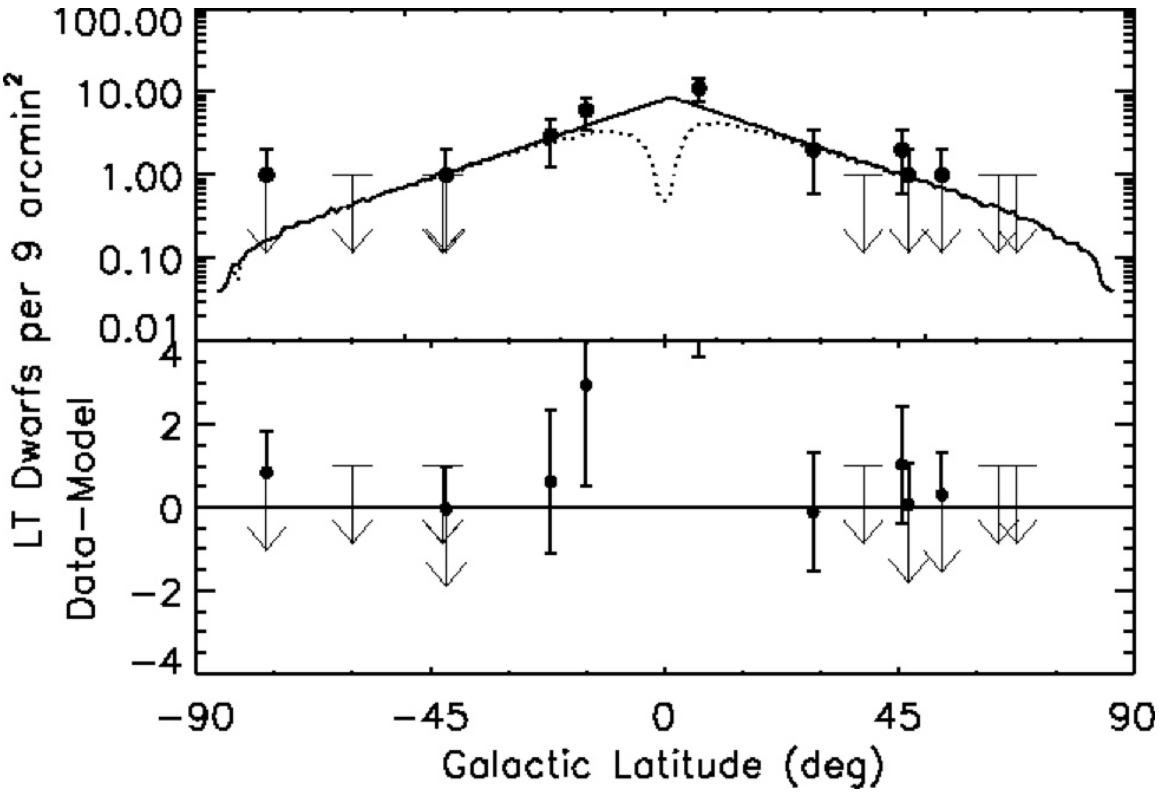

FIG. 27. **Top panel:** model surface density as a function of Galactic latitude. Here we have averaged over all longitudes with a 2.5σ-clipping to better handle the sparse statistics at high latitudes. The dotted and full drawn lines indicate models with and without extinction corrections, respectively. The data from the 15 ACS parallel fields are plotted for comparison as filled circles, and as downward arrows an upper limit when either zero or one object was detected. **Bottom panel:** the residuals from the upper panel as a function of Galactic latitude. Clearly the data where the dust corrections are large (ie. $|b^{\rm II}| \lesssim 15^\circ$) are the most deviant. The model used in both panels has a vertical scale height of 350 pc. The two fields outlying fields at $|b^{\rm II}| \lesssim 15^\circ$ are discussed in § 6.5. This figure is reproduced from Ryan et al. (2005).

horst, & Cohen 2003; Yan & Windhorst 2004a,b). Since our method is similar to the i'-band dropout technique, we expect possible contamination to the L- & T-dwarf star counts from the $z \simeq 6$ galaxies. In a recent study of the Hubble Ultra-Deep Field (HUDF), Yan & Windhorst (2004b) find 108 i'-band dropouts to $i' \sim 29$ mag using the $(i' - z') > 1.3$ mag color selection. Their sample has a median z'-band magnitude of 28.5 mag, and contains only three objects brighter than our limit of $z' = 26.0$ mag. Each of these three objects is considerably extended and could not be mistaken for a point-source. Since the majority of unresolved $z \simeq 6$ galaxies will be ~ 2.5 mag fainter, we conclude their contamination to our L- & T-dwarf sample must be negligible.

(2) Another known source of possible contaminates comes from dusty, elliptical galaxies with redshifts $1.0 \leq z \leq 1.5$, whose 4000 Å break occurs between the i' and z' bands (Yan, Windhorst, & Cohen 2003). With a typical color of $(i' - z') \sim 1.0$ mag, many of these objects would appear too blue in the absence of extreme internal reddening. Moreover the visual identification confirms that only point-like objects populate the "stellar locus" in the lower left of Figure 25. Hence, extended elliptical galaxies at $z \simeq 1$ could not grossly corrupt our sample.

(3) In addition to the above extragalactic sources, we anticipated contamination from galactic M-dwarfs for two different reasons. First, the color criterion of $(i' - z') > 1.3$ mag was primarily motivated by the $z \simeq 6$ galaxy surveys, and is ~ 0.5 mag too blue (Hawley et al. 2002) to have included only L- & T-dwarfs. When we repeated the above analysis for $(i' - z') \geq 1.8$ mag (Hawley et al. 2002) the star counts were reduced by $\sim 50\%$, and the inferred vertical scale height was 300 ± 100 pc.

While there is a significant contribution from late M-dwarfs, the vertical scale height was unaffected by the 0.5 mag difference in the color selection. Second, an appreciably reddened M-dwarf could have an $(i' - z')$ color of an unreddened L- or T-dwarf. This scenario requires considerable reddening, but only the two fields with $|b^{II}| \lesssim 15^{\circ}$ have $E(i' - z') \gtrsim 0.1$ mag. This effect could explain why these fields lie more than 1σ above the best-fit line in Figure 27, although we cannot be certain without more broadband filters and/or spectroscopy. We investigated the contribution from this effect by removing the two low-latitude fields and repeated the analysis. While this procedure reduced the observed star counts by $\sim 50\%$, it resulted in a vertical scale height of 360 ± 180 pc. Without further observations, it is difficult to definitively remove highly reddened M-dwarfs. However their contribution should not grossly affect our main goal.

6.6. Discussion

Using a suite of Monte Carlo simulations and 15 HST/ACS parallel fields, we find a vertical scale height of 350±50 pc for the L- & T-dwarf population based on 28 faint candidates. This estimated scale height is consistent with the known trend of increasing scale height with decreasing stellar mass, independent of reddening, color selections, and other Galactic parameters. Futhermore, our scale height measurement is consistent with the published results of Liu et al. (2002); Pirzkal et al. (2005). Using our value of the scale height, and the parameters and model discussed in § 6.3, we predict a total of $\sim 10^{11}$ L- & T-dwarfs and a total L- & T-dwarf mass of $\lesssim 10^{9}$ $M_{\odot}$ in the Milky Way.

This improved understanding of the L- & T-dwarf Galactic distribution will aide high-redshift surveys in better estimating the contamination of L- & T-dwarfs in such samples. In the recent HUDF pointed at $(\alpha, \delta) = (3^{\rm h}32^{\rm m}39\overset{\rm s}{.}0, -27^\circ47'29\overset{''}{.}1)$ with a depth of $z' \sim 29.5$ mag, we predict $\gtrsim 2$ L- & T-dwarfs in its ~ 11 arcmin^2 field of view, which has been confirmed by Pirzkal et al. (2005), who have spectroscopically identified three L- & T-dwarfs. We confirm that Galactic L- & T-dwarfs cannot significantly corrupt the $z \simeq 6$ surveys in high-latitude fields (the HUDF for example). However low-latitude fields will find a modest number of interloping L- & T-dwarfs. With only 28 candidates from 15 fields, our statistics remain sparse, and ideally require further observations.

CHAPTER 7

Conclusions

7.1. Summary

Using the deep, multiwavelength imaging and spectroscopic data in the HUDF and two GOODS fields, I have investigated primarily two topics in galaxy evolution:

(1) I derive a catalog of spectro-photometric redshifts from the combination of grism spectra with broadband imaging (Chapter 2). From this catalog, I construct the B-band galaxy luminosity function and probe nearly ~ 2 mag deeper than previous studies at the same redshift (Chapter 3). Therefore, I am able *measure* the faint-end slope in a redshift range, where it is customary to *assume* a faint-end slope of $\alpha \approx -1.3$ (eg. Willmer et al. 2006). By comparing to a suite of comparable measurements for $z \lesssim 6$, I find evidence that the faint-end slope steepens with redshift according to $\alpha(z) \simeq -1.12 - 0.12z$, which suggests that there are proportionally more dwarf galaxies in the faint-end of the LF at high redshift.

(2) I compute the fraction and number density for massive paired galaxies (Chapter 4) and luminous galaxies (Chapter 5) at $z \lesssim 6$, which is a generally accepted proxy for major mergers. The number density of major merger can be suitably fit by an empirically derived function which is similar in form to the LDDE model for X-ray selected QSOs (eg. Ueda et al. 2003). While the redshift evolution of major mergers and QSOs is qualitatively similar, the density of major mergers peaks at $z_{\rm max}^{\rm dens} = 1.04 \pm 0.10$, which is ~ 2 Gyr earlier in cosmic than the QSOs. This would suggest that if a major merger can trigger the feeding of a SMBH and a visible QSO, then it may take up to ~ 2 Gyr to efficiently fuel the SMBH so that it is observable in the X-rays. Furthermore, since the fraction of major mergers peaks at some redshift

($z_{\rm max}^{\rm frac} = 1.37 \pm 0.10$), only $f_{\rm rem}^{\rm lim} \sim 53\%$ of massive galaxies will have undergone a merger in the history of the Universe. This suggests that $(1 - f_{\rm rem}^{\rm lim}) \sim 47\%$ of galaxies form *monolithically* or without major mergers, although this does not exclude a series of minor mergers and/or steady gas infall.

7.2. Current Work

In the galaxy formation duty cycle, two or more galaxies merge and trigger a starburst in the remaining system(s). This star-formation continues for $\sim 1 - 2$ Gyr until the negative feedback from an actively accreting supermassive blackhole terminates the current star-formation. Therefore, we may expect the host galaxies of AGN to systematically contain a stellar population of $\sim 1 - 2$ Gyr in age. To investigate this possibility, I am in the process of a stellar population study of $\gtrsim 60$ bright, well-resolved galaxies in the HUDF. In particular, I will be fitting the broadband photometry in the $BVi'z'JH$-bands on a pixel-to-pixel basis in each galaxy.

In Figure 28, I show the stellar populations for an elliptical galaxy at $z = 0.62$ which is a known X-ray source (Rosati et al. 2002) as a preliminary result. The extremely large reduced χ^2 values in the nucleus of the galaxy (upper-right panel of Figure 28) suggests that the *simple* stellar populations are a poor model of the optical and near-infrared fluxes. Since this galaxy is a bright X-ray source, I assert that these χ^2 values are indicative of an active galactic nucleus. Furthermore, the distribution of ages is strongly bimodal (note: the ages of $\lesssim 10^7$ Gyr are associated with the neighboring galaxy to the East). The pixels best-modeled with an age of 10^{10} Gyr are predominately located in the nucleus of the galaxy, which for the reasons described

above are likely unreliable. Therefore, the majority of the pixels in this galaxy are $\sim 10^9$ Gyr old, which is consistent with the ages of many classical QSO hosts (eg. Canalizo et al. 2006) and the merger-driven, AGN-fueling model (eg. Springel, Di Matteo, & Hernquist 2005a,b; Hopkins et al. 2006). In a coming work, I will extend this analysis to many other galaxies in the HUDF to investigate a number of similar issues.

7.3. Future Work

The Early Release Science (ERS) survey with the Wide Field Camera 3 will add three ultraviolet (F225W, F275W, F336W) and three infrared (F098M, F125W, F160W) bandpasses with significantly higher sensitivities over a 5×10 arcmin^2 strip of GOODS-South (see Figure 1 for rough layout). These additional wavelengths will greatly improve the wavelength range of an already rich dataset.

While U-band observations were possible with the Wide Field Planetary Camera 2 (WFPC2), its field-of-view and sensitivity made deep observations very costly. With a nearly 30-fold increase in discovery efficiency, the ultraviolet observations for the ERS with WFC3 will be essentially a new probe of faint galaxies. The three planned ultraviolet filters will provide a means of identifying LBGs at $z \sim 1.7$, 2.3, and 2.8 from F225W, F275W, and F336W-dropouts, respectively. These LBGs will populate part of the *redshift desert*, a redshift range where no familiar spectral features can be observed by ground-based facilities. In addition to improving the photometric redshift catalogs, these LBGs can be used to further many of the topics studied in this dissertation.

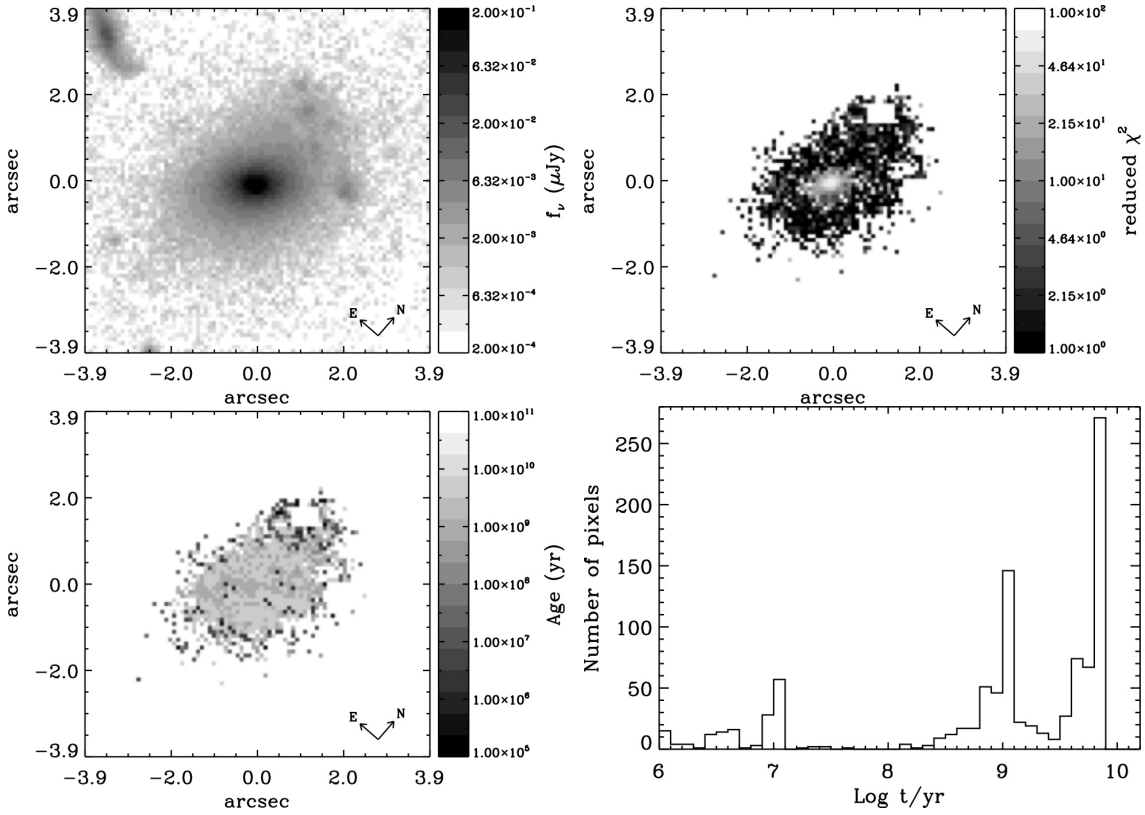

FIG. 28. A representative example of the pixel-to-pixel stellar population modeling, shown as a preliminary result. This elliptical galaxy at $z = 0.62$ was identified as an X-ray source in the 1 Ms Chandra observation (Rosati et al. 2002). The stellar populations are determined by a least-squares fit between the Bruzual & Charlot (2003) models and the $BVi'z'JH$-band photometry from ACS and NICMOS. In a clockwise fashion starting in the upper left, I show the HUDF i'-band image, the reduced χ^2, the distribution of population ages, and the spatial distribution of ages. Each pixel in these images subtends $\sim$600 pc in the restframe of this galaxy. Since the stellar population models do not account for flux from the active nucleus, the χ^2 is anomalously high in the central regions. While there is clearly a broad range of possible ages, the majority of the pixels are fit by ages of either $\sim 10^9$ Gyr or $\sim 10^{10}$ Gyr (NOTE: most of the pixels with ages $\lesssim 10^7$ Gyr are associated with the neighboring galaxy to the East). From the lower-left panel, the stellar populations in the nucleus are generally older than those toward the edge of the galaxy. This is qualitatively consistent with the size-luminosity evolution model (Roche et al. 1998), in which star-formation progresses outward from the nucleus. This figure is reproduced from Ryan et al. (2009).

(1) In Figure 7, I show the redshift evolution of the faint-end slope of the galaxy luminosity function. The apparent steepening of the faint-end slope is strongest for the luminosity functions measured in the restframe ultraviolet (blue points). Since the data at $z \gtrsim 3$ were all obtained from the study of LBGs, it would be ideal to collect a similar sample at $1.5 \lesssim z \lesssim 3$;

(2) In Chapter 5, I derive the galaxy pair fraction from LBGs selected as BVi'-band dropouts in the HUDF and GOODS fields. While these measurements are consistent with the results of Chapter 4, there is a void of observations at $2.5 \lesssim z \lesssim 3.5$. Therefore, the U-band dropouts will ideally complement my existing work at modest redshift at $0.5 \leq z \leq 2.5$ (Chapter 4) and $3.8 \lesssim z \lesssim 6$ (Chapter 5). On a related note, three independent teams (G. Illingworth PID: 11563, M. Trenti PID: 11700, and H. Yan PID: 11702) have recently been awarded (HST Cycle 17) infrared observations to discover z'- or Y-band dropouts (the choice of the Y-band slightly differs between the teams: Illingworth et al. will observe in F105W while Trenti et al. and Yan et al. will use F098M). Since these data will be immediately available, they can be used to push the major merger studies for $z \lesssim 9$.

The use of stellar population synthesis models (eg. Bruzual & Charlot 2003) has become a standard approach to estimate stellar masses, population age, and star-formation rates (eg. Papovich, Dickinson, & Ferguson 2001). While this approach is somewhat dependent on the suite of models, it is a fairly robust method of determining the physical properties of distant ($z \gtrsim 0.5$), faint galaxies (AB $\gtrsim 27$ mag). However, when using this technique, a critical assumption must typically be made: the observed

stellar population has a single, well-defined age with an easily parameterizable star formation history. While this scenario may be true for some massive ellipticals (Eggen, Lynden-Bell, & Sandage 1962; Larson & Tinsley 1978), the majority of galaxies are expected to have a spectrum of ages and a significantly more complex star formation history (eg. Cid Fernandes et al. 2005). This complication is most pronounced in merging systems, where two separate galaxies, each with its own stellar systems, combine and possibly trigger a starburst of a substantially younger age. Therefore, we may expect at least two distinct stellar populations in the resulting galaxy, and hence additional care must be taken when modeling such systems (Canalizo et al. 2007).

In addition to the six broadband filters in the ultraviolet and infrared, the ERS program will observe two pointings with the infrared grisms (G102L and G141L) over the PEARS (PID: 10530; PI: S. Malhotra) footprint. When combined with the three ultraviolet filters, B-band, and the existing optical grism spectra, the final spectra will cover 2200 Å $\lesssim \lambda_{\rm obs} \lesssim$ 1.7 μm, albeit with a variety of spectral resolutions. These data can be used to decompose the spectrum of a galaxy into its constituent stellar populations of varying ages, extinctions, and star-formation rates (Cid Fernandes et al. 2005; Papovich et al. 2006; Brammer, van Dokkum, & Coppi 2008). By applying this method to a sample of merging galaxies, I can separate the young population (which was presumably triggered by the merging) from the underlying old population (which must have been present prior to the merging). It will then be possible to study the merger-driven starburst activity.

REFERENCES

Abraham, R. G., Tanvir, N. R., Santiago, B. X., Ellis, R. G., Glazebrook, K., & van den Bergh, S. 1996, MNRAS, 279, L47

Abraham, R. G. 1999, IAUS, 186, 11

Abraham, R. G., et al. 2004, AJ, 127, 2455

Afonso, J., Mobasher, B., Koekemoer, A., Norris, R. P., & Cram L. 2006, AJ, 131, 1216

Arnouts, S., et al. 2005, ApJ, 619, L43

Bahcall, J. N. 1986, ARA&A, 24, 577

Bahcall, J. N. & Soneira, R. M. 1980, ApJS, 44, 73

Bahcall, J. N. & Soneira, R. M. 1981, ApJ, 246, 122

Bahcall, J. N. & Soneira, R. M. 1984, ApJS, 55, 67

Bahcall, J. N., Guhathakurta, P., & Schneider, D. P. 1990, *Science*, 248, 178

Bahcall, J. N., Kirhakos, S., Saxe, D. H., & Schneider, D. P. 1997, ApJ, 479, 642

Barger, A. J. & Cowie, L. L. 2005, ApJ, 635, 115

Barger, A. J., Cowie, L. L., Mushotzky, R. F., Yang, Y., Wang, W.-H., Steffen, A. T., & Capak, P. 2005, AJ, 129, 578

Barnes, J. E. 1992, ApJ, 393, 484

Baum, W. A. 1962, in IAU Conf. Symp. 15, Problems of Extragalactic Research, ed. G. C. McVittie (New York, NY: MacMillan Press), 390

Beckwith, S. V. W., et al. 2006, AJ, 132, 1729

Bell, E. F., et al. 2005, ApJ, 625, 23

Bell, E. F., Phleps, S., Somerville, R. S., Wolf, C., Borch, A., & Meisenheimer, K. 2006, ApJ, 652, 270

Bender, R., Burstein, D., & Faber, S. M. 1992, ApJ, 399, 462

Benítez, N. 2000, ApJ, 536, 571

Berrier, J. C., Bullock, J. S., Barton, E. J., Guenther, H. D., Zentner, A. R., & Wechsler, R. H. 2006, ApJ, 652, 56

Bershady, M. A., Jangren, A., & Conselice, C. J. 2000, AJ, 119, 2645

Bertin, E. & Arnouts, S. 1996, A&AS, 117, 393

Blanton, M. R., et al. 2003, ApJ, 592, 819

Bolzonella, M., Miralles, J.-M., & Pelló, R. 2000, A&A 363, 476

Bouwens, R. J., et al. 2004a, ApJ, 606, L25

Bouwens, R. J., et al. 2004b, ApJ, 616, L79

Bouwens, R. J., Illingworth, G. D., Thompson, R. I., & Franx, M. 2005, ApJ, 624, L5

Bouwens, R. J., Illingworth, G. D., Blakeslee, J. P., & Franx, M. 2006, ApJ, 653, 53

Bouwens, R. J. & Illingworth, G. D. 2006, *Nature*, 443, 189

Bouwens, R. J., Illingworth, G. D., Franx, M., & Ford, H. 2007, ApJ, 670, 928

Bower, R. G., Lucey, & Ellis, R. S. 1992, MNRAS, 254, 601

Bower, R. G., Benson, A. J., McMahon, R., Helly, J. G., Frenk, C. S., Baugh, C. M., Cole, S., & Lacey, C. G. 2006, MNRAS, 370, 645

Brammer, G. B., van Dokkum, P. G., & Coppi, P. 2008, ApJ, accepted, arXiv: 0807.1533

Brinchmann, J. & Ellis, R. S. 2000, ApJ, 536, L77

Brinchmann, J., Charlot, S., White, S. D. M., Tremonti, C., Kauffmann, G., Heckman, T., & Brinkmann, J. 2004, MNRAS, 351, 1151

Bruzual, G. & Charlot, S. 1993, ApJ, 405, 538

Bruzual, G. & Charlot, S. 2003, MNRAS, 344, 1000

Budavári, T., et al. 2005, ApJ, 619, L31

Bundy, K., Ellis, R. S., & Conselice, C. J. 2005, ApJ, 625, 621

Bunker, A. J., Stanway, E. R., Ellis, R. S., & McMahon, R. G. 2004, MNRAS, 355, 374

Burgasser, A. J., et al. 1999, ApJ, 522, L65

Burgasser, A., Kirkpatrick, D., Burrows, A., Liebert, J., Reid. N., Gizis, J., McGovern, M., & Prato, L. 2003, ApJ, 592, 1186

Burkey, J. M., Keel, W. C., Windhorst, R. A., & Franklin, B. E. 1994, ApJ, 429, 13

Caballero, J. A., Burgasser, A. J., & Klement, R. 2008, A&A, accepted, astro-ph/0805.4480

Canalizo, G., Stockton, A., Brotherton, M. S., & Lacy, M. 2006, NewAR, 50, 650

Canalizo, G., Bennert, N., Jungwiert, B., Stockton, A., Schweizer, F., Lacy, M., & Peng, C. 2007, ApJ, 669, 801

Caputi, K. I., Dunlop, J. S., McLure, R. J., & Roche, N. D. 2004, MNRAS, 353, 30

Carlberg, R. G. 1990a, ApJ, 350, 505

Carlberg, R. G. 1990b, ApJ, 359, L1

Carlberg, R. G. 1991, ApJ, 375, 429

Carlberg, R. G., Pritchet, C. J., & Infante, L. 1994, ApJ, 435, 540

Cassata, P., et al. 2005, MNRAS, 357, 903

Chabrier, G. 2001, ApJ, 554, 1274

Chabrier, G. 2002, ApJ, 567, 304

Chen, H.-W., et al. 2003, ApJ, 586, 745

Cid Fernandes, R., Mateus, A., Sodré, L., Stasińska, G., & Gomes, J. M. 2005, MNRAS, 358, 363

Cimatti, A., et al. 2004, *Nature*, 430, 184

Coe, D., Benítez, N., Sánchez, S., Jee, M., Bouwens, R., & Ford, H. 2006, AJ, 132, 926

Cohen, J. G., Hogg, D. W., Blandford, R., Cowie, L. L., Hu, E., Songaila, A., Shopbell, P., & Richberg, K. 2000, ApJ, 538, 29

Cohen, S. H., Windhorst, R. A., Odewahn, S. C., Chiarenza, C. A., & Driver, S. P. 2003, AJ, 125, 1762

Cohen, S. H., et al. 2006, ApJ, 639, 731

Cole, S., et al. 2001, MNRAS, 326, 255

Coleman, G. D., Wu, C.-C., & Weedman, D. W. 1980, ApJS, 43, 393

Connolly, A. J., Szalay, A. S., Dickinson, M., SubbaRao, M. U., & Brunner, R. J. 1997, ApJ, 486, L11

Conselice, C. J. 2003, ApJS, 147, 1

Conselice, C. J., Bershady, M. A., Dickinson, M., & Papovich C. 2003, ApJ, 126, 1183

Conselice, C. J. 2006, ApJ, 638, 686

Conselice, C. J., Rajgor, S., & Myers, R. 2008, MNRAS, 386, 909

Cowie, L. L., Songalia, A., Hu, E. M., & Cohen, J. G. 1996, AJ, 112, 839

Cristiani, S., et al. 2004, ApJ, 600, L119

Cross, N. J. G., et al. 2004, AJ, 128, 1990

Croton, D. J., et al. 2005, MNRAS, 356, 1155

Croton, D. J., et al. 2006, MNRAS, 356, 1155

Cruz, K. C., Reid, I. N., Liebert, J., Kirkpatrik, J. D., Lowrance, P. J. 2003, AJ, 126, 2421

Daddi, E., et al. 2004, ApJ, 617, 746

Daddi, E., et al. 2005, ApJ, 626, 680

Daddi, E., et al. 2007, ApJ, 670, 173

Dahlen, T., Mobasher, B., Dickinson, M., Ferguson, H. C., Giavalisco, M., Kretchmer, C., & Ravindranath, S. 2007, ApJ, 654, 172

Davis, M., et al. 2007, ApJ, 660, L1

de Grijs, R., Peletier, R., & van der Kruit, P. 1997, A&A, 327, 966

De Lucia, G., Springel, V., White, S. D. M., Croton, D., & Kauffmann, G. 2006, MNRAS, 366, 499

De Marchi, G. et al. 2004, Detector Quantum Efficiency and Photometric Zero Points of the ACS, Instrument Science Report, (STScI, Baltimore)

de Mello, D. F., Dahlen, T., Gardner, J. P., & Grogin, N. A. 2006, AJ, 132, 2014

de Propris, R., Liske, J., Driver, S. P., Allen, P. D., & Cross, N. J. G. 2005, AJ, 130, 1516

de Propris, R., Conselice, C. J., Driver, S. P., Liske, J., Patton, D., Graham, A., & Allen, P. 2007, 666, 212

Dekel, A. & Silk, J. 1986, ApJ, 303, 39

Delfosse, X., Tinney, C. G., Forveille, T., Epchtein, N., Borsenberger, J., Fouqué, P., Kimeswenger, S., & Tipène, D. 1999, A&AS, 135, 41

Dickinson, M., Papovich, C., Ferguson, H. C., & Budavári, T. 2003, ApJ, 587,25

Dow-Hygelund, C. C., et al. 2007, ApJ, 660, 47

Driver, S. P., Windhorst, R. A., & Griffiths, R. E. 1995, ApJ, 453, 48

Driver, S. P., Windhorst, R. A., Ostrander, E. J., Keel, W. C., Griffiths, R., E., Ratnatunga, K. U. 1995, ApJ, 449, L23

Driver, S. P. 1999, ApJ, 526, L69

Driver, S. & de Propris, R. 2003, Ap&SS, 2003, 285, 175

Eggen, O. J., Lynden-Bell, D., & Sandage, A. R. 1962, ApJ, 136, 748

Ellison, S. L., Patton, D. R., Simard, L., & McConnachie, A. W. 2008, ApJ, 135, 1877

Elmegreen, D. M. & Elmegreen, B. G. 2006, ApJ, 651, 676

Elmegreen, D. M., Elmegreen, B. G., Ferguson, T., & Mullan, B. 2007, ApJ, 663, 734

Elsner, F., Feulner, G., & Hopp, U. 2008, A&A, 477, 503

Eyles, L. P., Bunker, A. J., Stanway, E. R., Lacy, M., Ellis, R. S., & Doherty, M. 2005, MNRAS, 364, 443

Fakhouri, O. & Ma, C.-P. 2008, MNRAS, 386, 577

Fall, S. M. & Efstathiou, G. 1980, MNRAS, 193, 189

Ferguson, H. C. & Babul, A. 1998, MNRAS, 296, 585

Ferguson, H. C. 1999, ASPC, 191, 51

Ferguson, H. C., Dickinson, M., & Williams, R. 2000, ARA&A, 38, 667

Ferguson, H. C., et al. 2004, ApJ, 600, L107

Fernández-Soto, A., Lanzetta, K. M., & Yahil, A. 1999, ApJ, 513, 34

Fontana, A., et al. 1999, A&A, 343, L19

Förster Schreiber, N. M., et al. 2004, ApJ, 616, 40

Frei, Z., Guhathakurta, P., Gunn, J. E., & Tyson, J. A. 1996, AJ, 111, 174

Fried, J. W., et al. 2001, A&A, 367, 788

Giavalisco, M., et al. 2004a, ApJ, 600, L93

Giavalisco, M., et al. 2004b, ApJ, 600, L103

Gilli, R., et al. 2007, A&A, 475, 83

Gilmore, G & Reid, N. 1983, MNRAS, 202, 1025

Gilmore, G. 1984, MNRAS, 207, 223

Gilmore, G., Wyse, R., & Kuijken, K. 1989, ARA&A, 27, 555

Glazebrook, K., Ellis, R., Santiago, B., & Griffiths, R. 1995, MNRAS, 275, L19

Governato, F., Gardner, J. P., Stadel, J. Quinn, T., & Lake, G. 1999, AJ, 117, 1651

Grazian, A., et al. 2006, A&A, 449, 951

Grogin, N. A., et al. 2003, ApJ, 595, 685

Grogin, N. A., et al. 2005, ApJ, 627, L97

Guyon, O., Sanders, D. B., & Stockton, A. 2006, ApJS, 166, 89

Gwyn, S. D. J. & Hartwick, F. D. A. 1996, ApJ, 468, L77

Haarsma, D. B., Partridge, R. B., Windhorst, R. A., & Richards, E. A. 2000, ApJ, 544, 641

Hasinger, G., Miyaji, G., & Schmidt, M. 2005, A&A, 441, 417

Hathi, N. P., Jansen, R. A., Windhorst, R. A., Cohen, S. H., Keel, W. C., Corbin, M. R., & Ryan, R. E., Jr. 2008a, AJ, 135, 156

Hathi, N. P., Malhotra, S., & Rhoads, J. E. 2008b, ApJ, 673, 686

Hawley, S. et al. 2002, ApJ, 123, 3409

Heckman, T. M., et al. 2005, ApJ, 619, L35

Herschel W. 1785, RSPT, 75, 213

Hopkins, A. M. & Beacom, J. F. 2006, ApJ, 651, 142

Hopkins, P. F., Hernquist, L., Cox, T. J., Di Matteo, T., Robertson, B., & Springel, V. 2006, ApJS, 163, 1

Hsieh, B. C., Yee, H. K. C., Lin, H., Gladders, M. D., & Gilbank, D. G. 2008, ApJ, in press

Hubble, E. P. 1936, Realm of the Nebulae, New Haven, CT: Yale University Press

Ilbert, O., et al. 2004, MNRAS, 351, 541

Iwata, I., et al. 2003, PASJ, 55, 415

Kapteyn, J. C. 1922, ApJ, 55, 302

Kartaltepe, J. S., et al. 2007, ApJS, 172, 320

Kauffmann, G. & Haehnelt, M. 2000, MNRAS, 311, 576

Kauffmann, G., White, S. D. M., & Guiderdoni, B. 1993, MNRAS, 264, 201

Kennicutt, R. C., Jr. 1998, ApJ, 498, 541

Khochfar, S. & Burkert, A. 2001, ApJ, 561, 517

Khochfar, S., Silk, J., Windhorst, R. A., & Ryan, R. E., Jr. 2007, ApJ, 668, 115

Khochfar, S. & Ostriker, J. P. 2008, ApJ, 680, 54

Kirkpatrick, J. D., et al. 1999, ApJ, 519, 802

Kistler, M. D., Yüksel, H., Beacom, J. F., & Stanek, K. Z. 2008, ApJ, 673, L119

Kitzbichler, M. G. & White, S. D. M. 2008, MNRAS, submitted, astro-ph/0804.1965

Klesman, A. & Sarajedini, V. 2007, ApJ, 665, 225

Koekemoer, A. M., Fruchter, A. S., Hook, R., & Hack, W. 2002 "*The 2002 HST Calibration Workshop*" Space Telescope Science Institute, 2002

Koekemoer, A. M., et al. 2004, ApJ, 600, L123

Koo, D. C. 1985, AJ, 90, 418

Lai, K., Huang, J.-S., Fazio, G., Cowie, L. L., Hu, E. M., & Kakuzo, Y. 2007, ApJ, 655, 704

Lanzetta, K. M., Yahil, A., & Fernández-Soto, A. 1996, Nature, 381, 759

Larsen, J. A. & Humphreys, R. M. 2003, AJ, 125,1958

Larson, R. B. & Tinsley, B. M. 1974, ApJ, 192, 293

Larson, R. B. & Tinsley, B. M. 1978, ApJ, 219, 46

Lee, K.-S., Giavalisco, M., Gnedin, O. Y., Somerville, R. S., Ferguson, H. C., Dickinson, M., & Ouchi, M. 2006, ApJ, 642, 63

Le Fèvre, O., et al. 2000, MNRAS, 311, 565

Le Fèvre, O., et al. 2005, A&A, 439, 845

Lilly, S. J., Le Fèvre, O., Hammer, F., & Crampton, D. 1996, ApJ, 406, L1

Lin, H., Yee, H. K. C., Carlberg, R. G., & Ellingson, E. 1997, ApJ, 475, 494

Lin, H., et al. 1999, ApJ, 518, 533

Lin, L., et al. 2004, ApJ, 617, L9

Liu, M., Wainscoat, R., Martín, E. L., Barris, B., & Tonry, J. 2002, ApJ, 568, L107

Liu, C., T., Capak, P., Mobasher, B., Paglione, T. A. D., Rich, M. R., Scoville, N. Z., Tribiano, S. M., & Tyson, N. D. 2008, ApJ, 672, 198

Lotz, J. M., Madau, P., Giavalisco, M., Primack, J., & Ferguson, H. C. 2006, ApJ, 636, 592

Lotz, J. M., et al. 2008, ApJ, 672, 177

Madau, P., Ferguson, H. C., Dickinson, M. E., Giavalisco, M., Steidel, C. C., & Fruchter, A. 1996, MNRAS, 283, 1388

Madau, P., Pozzetti, L., & Dickinson, M. 1998, ApJ, 498, 106

Madau, P., Haard, F., & Rees, M. J. 1999, ApJ, 514, 648

Mainieri, V., et al. 2005, A&A, 437, 805

Majewski, S. R. 1993, ARA&A, 31, 575

Malhotra, S., et al. 2005, AJ, 626, 666

Marchesini, D., et al. 2007, ApJ, 656, 42

Marconi, A., Risaliti, G., Gilli, R., Hunt, L. K., Maiolino, R., & Salvati, M. 2004, MNRAS, 351, 169

Marleau, F. R. & Simard, L. 1998, ApJ, 507, 585

Marzke, R. O., da Costa, L. N., Pellegrini, P. S., Willmer, C. N. A., & Geller, M. J. 1998, ApJ, 503, 617

Mazzali, P. A., et al. 2006, *Nature*, 442, 1018

Meurer, G. R., Heckman, T. M., Lehnert, M. D., Leitherer, C., & Lowenthal, J. 1997, AJ, 114, 54

Meurer, G. R., Heckman, T. M., & Calzetti, D. 1999, ApJ, 521, 64

Mo, H. J., Mao, S., & White, S. D. M. 1999, MNRAS, 304, 175

Mobasher, B., Rowan-Robinson, M., Georgakakis, A., & Eaton, N. 1996, MNRAS, 282, L7

Mobasher, B., et al. 2004, ApJ, 600, L167

Mobasher, B., et al. 2005, ApJ, 635, 832

Mobasher, B., et al. 2007, ApJS, 172, 117

Nakajima, T., Oppenheimer, B. R., Kulkarni, S. R., Golimowski, D. A., Matthews, K., & Durrance, S

Neuschaefer, L. W., Im, W., Ratnatunga, K. U., Griffiths, R. E., & Casertano, S. 1997, ApJ, 480, 59

Norberg, P., et al. 2002, MNRAS, 336, 907

Odewahn, S. C., Windhorst, R. A., Driver, S. P., & Keel, W. C. 1996, ApJ, 472, L13

Oesch, P. A., et al. 2007, ApJ, 671, 1212

Oke, J. B. & Gunn, J. E. 1983, ApJ, 266, 713

Oppenheimer, B. R., Kulkarni, S. R., Matthews, K., & Nakajima, T. 1995, Science, 270, 1478

Overzier, R. A., Bouwens, R. J., Illingworth, G. D., & Franx, M. 2006, ApJ, 648, L5

Overzier, R. A., et al. 2008, ApJ, 677, 37

Papovich, C., Dickinson, M., & Ferguson, H. C. 2001, ApJ, 559, 620

Papovich, C., Giavalisco, M., Dickinson, M., Conselice, C. J., & Ferguson, H. C. 2003, ApJ, 598, 827

Papovich, C., et al. 2006, ApJ, 640, 92

Patton, D. R., Pritchet, C. J., Yee, H. K. C., Ellingson, E., & Carlberg, R. G. 1997, ApJ, 475, 29

Patton, D. R., Carlberg, R. G., Marzke, R. O., Pritchet, C. J., da Costa, L. N., & Pellegrini, P. S., 2000, ApJ, 536, 153

Patton, D. R., et al. 2002, AJ, 565, 208

Patton, D. R. & Atfield, J. E. 2008, ApJ, accepted, astro-ph/0806.0018

Peebles, P. J. E. 1980, The Large-Scale Structure of the Universe, (Princeton, NJ: Princeton University Press)

Pirzkal, N., et al. 2004, ApJS, 154, 501

Pirzkal N., et al. 2005, ApJ, 622, 319

Pirzkal, N., Malhotra, S., Rhoads, J. E., & Xu, C. 2007, ApJ, 667, 49

Porcel, C., Garzón, F., Jimenénez-Vicente, J., & Battaner, E. 1998, A&A, 330, 136

Ravikumar, C. D., et al. 2006, A&A, 465, 1099

Ravindranath, S., et al. 2006, ApJ, 652, 963

Reid, I. N., et al. 1999, ApJ, 521, 613

Rhoads, J. E., et al. 2005, ApJ, 621, 582

Riess, A. G., et al. 2004, ApJ, 600, L163

Rix, H.-W., et al. 2004, ApJS, 152, 163

Robin, A., Reylé, C., & Crézé M. 2000, A&A 359, 103

Robin, A., Reylé, C., Derrière, S., & Picaud, S. 2003, A&A, 409, 523

Roche, N., Ratnatunga, K., Griffiths, R. E., Im, M., & Naim, A. 1998, 293, 157

Rosati, P., et al. 2002, ApJ, 566, 667

Ryan, R. E., Jr., Hathi, N. P., Cohen, S. H., & Windhorst, R. A. 2005, 631, L159

Ryan, R. E., Jr., et al. 2007, ApJ, 668, 839

Ryan, R. E., Jr., Cohen, S. H., Windhorst, R. A., & Silk, J. 2008a, ApJ, 678, 751

Ryan, R. E., Jr., Cohen, S. H., Windhorst, R. A., Khochfar, S., & Silk, J. 2008b, ApJ, in preparation

Ryan, R. E., Jr., Jansen, R. A., Cohen, S. H., & Windhorst, R. A. 2009, ApJ, in preparation

Salpeter, E. E. 1955, ApJ, 121, 161

Sanders, D. B. & Mirabel, I. F. 1996, ARA&A, 34, 749

Sawicki, M. J., Lin, H., & Yee, H. K. C. 1997, AJ, 113, 1

Sawicki, M. J. & Yee, H. K. C. 1998, AJ, 115, 1329

Sawicki, M. & Thompson, D. 2006, ApJ, 642, 653

Scannapieco, E. & Oh, S. P. 2004, ApJ, 608, 62

Scannapieco, E., Silk, J., & Bouwens, R. 2005, ApJ, 635, L13

Schmidt, M. 1968, ApJ, 151, 393

Schechter, P. 1976, ApJ, 203, 297

Schlegel, D. J., Finkbeiner, D. P., & Davis, M. 1998, AJ, 500, 525

Schneider, D. N., et al. 2005, AJ, 130, 367

Scoville, N., et al. 2007, ApJS, 172, 1

Sérsic, J. L. 1968, Atlas de Galaxias Australes (Córdoba: Obs. Astron., Univ. Nac. Córdoba)

Siegel, M. H., Majewski, S. R., Reid, I. N., & Thompson, I. B. 2002, ApJ, 578, 151

Silk, J. & Rees, M. J. 1998, A&A, 331, L1

Silverman, J. D., et al. 2008, ApJ, 675, 1025

Spergel, D. N., et al. 2007, ApJS, 170, 377

Springel, V., Di Matteo, T., & Hernquist, L. 2005a, MNRAS, 361, 776

Springel, V., Di Matteo, V., & Hernquist, L. 2005b, ApJ, 620, L79

Stanek, K. Z., et al. 2003, ApJ, 591, L17

Stark, D. P., Bunker, A. J., Ellis, R. S., Eyles, L. P., & Lacy, M. 2007, ApJ, 659, 84

Stiavelli, M., Fall, S. M., & Panagia, N. 2004, ApJ, 610, L1

Straughn, A. N., Cohen, S. H., Ryan, R. E., Jr., Hathi, N. P., Windhorst, R. A., & Jansen, R. A. 2006, ApJ, 639, 724

Strauss, M. A., et al. 1999, ApJ, 522, L61

Somerville, R. S. & Kolatt, T. S. 1999, MNRAS, 305, 1

Somerville, R., S., Lee, K., Ferguson, H. C., Gardner, J. P., Moustakas, L., A., & Giavalisco, M. 2004, 600, L171

Stanway, E. R., Bunker, A., & McMahon, R. G. 2003, Ap&SS, 284, 381

Stanway, E. R., Bunker, A. J., McMahon, R. G., Ellis, R. S., Treu, T., & McCarthy, P. J. 2004a, ApJ, 607, 704

Stanway, E. R., et al. 2004b, ApJ, 604, L13

Stanway, E. R., McMahon, R. G., & Bunker, A. J. 2005, MNRAS, 359, 1184

Stanway, E. R., et al. 2007, MNRAS, 376, 727

Steidel, C. C., Giavalisco, M., Pettini, M., Dickinson, M., & Adelberger, K. L. 1996, ApJ, 462, L17

Steidel, C. C., Adelberger, K. L., Giavalisco, M., Dickinson, M., & Pettini, M. 1999, ApJ, 519, 1

Taylor-Mager, V. A., Conselice, C. J., Windhorst, R. A., & Jansen, R. A. 2007, ApJ, 659, 162

Teplitz, H., I., Gardner, J. P., Malumuth, E. M., & Heap, S. R. 1998, ApJ, 506, L17

Thompson, R. I., et al. 2005, AJ, 130, 1

Thompson, R. I., Eisenstein, D., Fan, X., Dickinson, M., Illingworth, G., & Kennicutt, R. C., Jr. 2006, ApJ, 647, 787

Toomre, A. & Toomre, J. 1972, ApJ, 178, 623

Toomre, A. 1977, in "Evolution of Galaxies and Stellar Populations," ed. B. M. Tinsley & R. B. Larson (New Haven: Yale Univ. Press), 401

Treu, T., Ellis, R. S., Liao, T. X., & van Dokkum, P. G. 2005, ApJ, 622, L5

Treister, E., et al. 2004, ApJ, 616, 123

Trentham, N. 1998, MNRAS, 294, 193

Trujillo, I., et al. 2006, ApJ, 650, 18

Tsvetanov, Z. I., et al. 2000, ApJ, 531, L61

Ueda, Y., Akiyama, M., Ohta, K., & Miyaji, T. 2003, ApJ, 598, 886

Urrutia, T., Lacy, M., & Becker, R. H. 2008, ApJ, 674, 80

van den Bergh, S., Abraham, R. G., Ellis, R. S., Tanvir, N. R., Santiago, B. X., & Glazebrook, K. G. 1996, AJ, 112, 359

Vanzella, E., et al. 2006, A&A, 454, 423

von Seeliger, H. 1898, Abh. Bayerische Akad. Wiss., Math.-Phys. KI, 19, 564

Waddington, I., Dunlop, J. S., Peacock, J. A., & Windhorst, R. A. 2001, MNRAS, 328, 882

Wang, J. X., Malhotra, S., & Rhoads, J. E. 2005, ApJ, 622, L77

White, S. D. M. & Frenk, C. S. 1991, ApJ, 379, 52

Wiklind, T., Dickinson, M., Ferguson, H. C., Giavalisco, M., Mobasher, B., Grogin, N. A., & Panagia, N. 2008, ApJ, 2008, 676, 781

Williams, R. E., et al. 1996, AJ, 112, 1335

Willmer, C. N. A. 1997, AJ, 114, 898

Willmer, C. N. A., et al. 2006, ApJ, 647, 853

Windhorst, R. A., et al. 2002, ApJS, 143, 113

Windhorst, R. A., Hathi, N. P., Cohen, S. H., Jansen, R. A., Kawata, D., Driver, S. P., & Gibson, B. 2008, AdSpR, 41, 1965

Wolf, C., Meisenheimer, K., Rix, H.-W., Borch, A., Dye, S., and Kleinheinrich, M. 2003, A&A, 401, 73

Wyder, T. K., et al. 2005, ApJ, 619, L15

Xu, C. K., Sun, Y. C., & He, X. T. 2004, ApJ, 603, L73

Xu, C., et al. 2007, AJ, 134, 169

Yahata, N. 2000, ApJ, 538, 493

Yamagata, T., & Yoshii, Y. 1992, AJ, 103, 117

Yan, H. et al. 2002, ApJ, 580, 725

Yan, H., Windhorst, R. A., & Cohen S. H. 2003, ApJ, 585, L93

Yan, H. & Windhorst, R. A. 2004a, ApJ, 600, L1

Yan, H. & Windhorst, R. A. 2004b, ApJ, 612, L93

Yan, H., Dickinson, M., Giavalisco, M., Stern, D., Eisenhardt, P. R. M., & Ferguson, H. C. 2006, ApJ, 651, 24

Yee, H. K. C. & Ellingson, E. 1995, ApJ, 445, 37

Young, P. A. & Fryer, C. L. 2007, ApJ, 670, 584

Zepf, S. E. & Koo, D. C. 1989, ApJ, 337, 34

Zucca, E., et al. 2006, A&A, 455, 879